

Università degli Studi di Napoli Federico II

Dottorato di Ricerca in
Ingegneria Strutturale, Geotecnica e Rischio Sismico

THESIS FOR THE DEGREE OF DOCTOR OF PHILOSOPHY

Constructional design of echinoid test: Mechanical behavior and potential for biomimetic applications

by

PASQUALE CESARANO

Advisor: Prof. Francesco Marmo
Co-Advisor: Prof. Luciano Rosati

SCUOLA POLITECNICA E DELLE SCIENZE DI BASE
DIPARTIMENTO DI STRUTTURE PER L'INGEGNERIA E L'ARCHITETTURA

AVGVST FRIDERICVS IMPERATOR ROMANORVM SEMP

“Qualunque cosa dobbiamo affrontare, qualunque siano le nostre lotte interiori, abbiamo sempre una scelta. Sono le nostre scelte che fanno di noi quello che siamo, e abbiamo sempre la possibilità di fare la scelta giusta.”

Peter Parker, Spider-Man.

Constructional design of echinoid test: Mechanical behavior and potential for biomimetic applications

Ph.D. Thesis presented

for the fulfillment of the Degree of Doctor of Philosophy

in Ingegneria Strutturale, Geotecnica e Rischio Sismico

by

PASQUALE CESARANO

October 2024

Approved as to style and content by

_____

Prof. Francesco Marmo, Advisor

_____

Prof. Luciano Rosati, Co-advisor

Università degli Studi di Napoli Federico II

Ph.D. Program in Ingegneria Strutturale, Geotecnica e Rischio Sismico

XXXVI cycle - Chairman: Prof. Iunio Iervolino

www.dist.unina.it/dottorati-di-ricerca/dottorati

Candidate's declaration

I hereby declare that this thesis submitted to obtain the academic degree of Philosophiæ Doctor (Ph.D.) in Ingegneria Strutturale, Geotecnica e Rischio Sismico is my own unaided work, that have not used other than the sources indicated, and that all direct and indirect sources are acknowledged as references.

Parts of this dissertation have been published in international journals and/or conference proceedings.

Napoli, October 07, 2024

Pasquale Cesarano

Abstract

Structural variability of biominerals has been demonstrated to result in unusual advantageous mechanical properties in many organismal structures, including vertebrate bones, mollusk shells and sea urchin teeth and spines. These observations inspired numerous researches on biological materials selected over millions of years of evolution to discover their hidden structural secrets and recreate them into new technical applications. Interesting structural strategies are arising from studying the echinoid skeleton that can inspire the engineering world of building constructions at different dimensional scales. Echinoids, commonly known as sea urchins, are characterized by an ultralight-weight and resistant skeleton consisting of a porous 3D lattice-like meshwork, known as stereom. The stereom displays unique structural, compositional and crystallographic heterogeneities able to meet several mechanical needs according to a direct and clear structure–function relationship adapted to withstand biotic and abiotic stresses.

The main goal of this doctoral research was to gain new insights about the microarchitectural variability analyzing the interambulacral plate of the sea urchin *Paracentrotus Lividus*. Accordingly, micro-CT scans, image analysis, 3D modelling, and linear elastic FE-Analysis were conducted to provide new insights about the topological and geometrical variability of the different stereom types, and their region-specific mechanical behavior calculated for tensile and shear loadings. The results achieved were of value to improve the understanding of the mechanical function of the stereom variability, as well as to identify adaptive strategies to develop new lightweight, high-performance impact-resistant and energy-absorbent bioinspired materials. These bioinspired structural materials can be effectively employed in building construction as well as in many other fields of our society, reducing energy and resources and thus providing environmental and economic advantages.

Keywords: biomimetic, structural materials, echinoids, *Paracentrotus lividus*, stereom.

Sintesi in lingua italiana

Il lavoro di ricerca è finalizzato allo studio del comportamento meccanico del guscio degli echinoidi, comunemente conosciuti come ricci di mare. Questa struttura naturale è stata studiata sia dal punto di vista macroscopico che dal punto di vista microscopico al fine di determinare il modo in cui la microstruttura porosa che costituisce la teca degli echinoidi è organizzata spazialmente e come questa organizzazione influisce sulle proprietà meccaniche emergenti alla scala macroscopica.

Gli echinoidi, comunemente conosciuti come ricci di mare, sono una classe di invertebrati dall'estremo successo evolutivo che popolano i mari da più di 450 milioni di anni. Durante la loro evoluzione, hanno sviluppato una struttura scheletrica calcitica capace di adattarsi efficacemente a resistere ai vari stress biotici e abiotici ambientali. Ciò è dovuto al design ultraleggero ottimizzato per incrementare la resistenza strutturale. Lo scheletro è costituito da una rete porosa tridimensionale, nota come stereoma, che presenta eterogeneità uniche strutturali, composizionali e cristallografiche in grado di soddisfare le esigenze meccaniche locali. Gradienti strutturali di varie geometrie trabecolari, topologie, orientamenti e composizioni possono essere rilevati a diverse scale, portando a pattern specie-specifici che risultano in proprietà meccaniche emergenti.

Il concetto costruttivo e i principi di funzionamento correlati allo scheletro degli echinoidi offrono preziose intuizioni per migliorare il comportamento meccanico nella scienza delle costruzioni e dei materiali industriali.

In tale contesto, secondo un approccio definito biomimetico, la ricerca svolta ha previsto un'analisi approfondita della variabilità scheletrica degli echinoidi con l'obiettivo di acquisire nuove intuizioni riguardo la loro configurazione ultrastrutturale e al suo significato funzionale meccanico per future applicazioni ingegneristiche strutturali. Di conseguenza, sono state effettuate scansioni micro-CT, analisi di immagine, modellazione 3D e analisi agli elementi finiti in regime elastico lineare fornendo nuovi dati sulla variabilità topologica

e geometrica dei diversi tipi di stereomi e andandone a definire il loro comportamento meccanico specifico per regione calcolato per carichi di trazione e di taglio.

Parole chiave: echinoidi, biomimetica, materiali biologici, comportamento meccanico.

Contents

Acknowledgements

The completion of this PhD thesis marks the end of a journey that I could never have undertaken without the support of many people, to whom I would like to express my deep gratitude.

Embarking on a new path is never easy, but when passion is involved, choosing that path always feels like the right thing to do. It all began on a cold winter evening in 2020, in Casoria. I was with my dear friend Giovanni Forte, sitting at a pizzeria table, waiting to enter the cinema to watch Star Wars: The Rise of Skywalker. In a moment of openness, I told him about one of my greatest regrets: not pursuing a PhD after my degree. His response struck me deeply and ignited a spark within me for the future: "What's stopping you from applying to the next competition and chasing the path you want so much?"

In the following months, that spark turned into a true desire to engage in academic research. The aspiration to contribute to the scientific community grew stronger, and what had initially been just a dream became a concrete reality. I then decided to participate in the competition for the PhD program in Structural Engineering, Geotechnics, and Seismic Risk (Cycle XXXVI). Despite coming from a background in Mechanical Engineering, the decision to apply felt natural.

The opportunity to work with Professors Francesco Marmo and Luciano Rosati was a dream come true for me. Collaborating with minds of such caliber was not only an honor but also a great source of pride.

First and foremost, I wish to express my most sincere gratitude to my advisor, Professor Francesco Marmo. Since my university days, I have had the deepest respect for him, not only for his technical knowledge but also for his human qualities. I would like to thank him for his constant guidance, patience, and encouragement throughout this thesis journey. His expertise, dedication, and passion for research have been a source of inspiration and have allowed me to grow, both professionally and personally. The road was not easy, and I faced many ups and downs from various aspects of life, even beyond the academic field. That is why I am particularly grateful for his support during every moment, always making me feel capable of facing any challenge.

A special thanks also goes to my co-advisor, Professor Luciano Rosati, for his constant support and invaluable advice during the crucial moments of my research. His patience and availability, which have always distinguished him, have been priceless. More than just a professor, Professor Rosati has always

been a paternal figure to his students, and this quality will remain indelible in our memories. I cannot help but say, simply, thank you.

I would like to express my deep gratitude to Professor Elio Sacco for his invaluable support. His expertise, passion, and creativity played a pivotal role in strengthening my curiosity toward engineering.

A special thanks also goes to Professor Salvatore Sessa: your energetic passion for work has been an incredible source of inspiration. Your generosity in sharing your experience, combined with your professionalism and kindness, was fundamental, especially during our conversations about my thesis topic.

Finally, I would like to thank Professor Massimiliano Fraldi for his constant support, stimulating discussions, and valuable advice.

My heartfelt thanks go to my dear friend Giovanni Forte: this journey would not have been the same without being able to share its challenges with a friend like him. Thank you for being not only a source of inspiration but also for your constant presence, even when I burdened you with my work-related and personal difficulties. You have been a precious companion in this adventure, giving me the courage and energy needed during the toughest moments.

A special thank you goes to Alessandra Rosati. We met by chance during the first year of the PhD, but it feels like we've known each other forever. I want to thank you for your support, your constructive criticism, and the kindness with which you listened to me, both regarding academic and personal matters.

I would like to extend a sincere thank you to the company I work for, CAE Technologies. Special thanks to the CEO, Alberto Naviglio, for the invaluable support that made this research possible. Thank you for your trust and for believing in the value of this research, which I hope will also benefit our organization.

A special thanks goes to my colleague and friend, Giovanni D'Aniello, with whom I have shared not only hours of work and research but also moments of personal growth and reflection. Your constant presence, support, and ability to always offer a clear and stimulating perspective were fundamental during this journey.

My greatest acknowledgment goes to my greatest wealth, my parents. I cannot forget to thank my family, who have always been by my side, even in the most difficult times. To my parents, Domenico and Antonella, I extend my deepest

gratitude for their unconditional love, support, and patience. Without them, this achievement would not have been possible.

A special thank you goes to my sister, Emilia. Thank you for always being by my side, for your unwavering support, and for encouraging me in moments when I needed it the most.

A special thought goes to my beloved nieces, Myriam, Manuela, and Marta, whose sweetness and smiles brought joy and lightness even during the most challenging moments of this journey. Your energy and affection gave me unexpected strength and reminded me of the importance of finding time to laugh and enjoy the little things, even during the most demanding challenges. This achievement is also for you, with the hope that you always believe in your dreams and find the strength to achieve them.

Last but not least, my biggest thank you goes to Valentina Perricone. In life, you meet many people: some pass by, while others leave an indelible mark, becoming beautiful memories along our path. Valentina is undoubtedly one of those. Without her support, I would not be writing these acknowledgments today. If I managed to complete this journey, I simply owe it to her.

Valentina has always been by my side, at any time and any hour, helping me not only with revising papers and the thesis but also with her infinite availability and patience. Life is often compared to a train journey, and I am glad that you were part of mine.

I hope that our journey together continues, and that we can contribute even more to this research side by side.

Lastly, I wish to dedicate a special thank you to my son, Domenico. The year 2023, specifically September 7th, was when you came into my life. Thank you for giving profound meaning to this journey with your presence. Thank you for filling my days with joy, energy, and unconditional love. Even during the most demanding moments, your smile and curiosity about life reminded me of what truly matters and gave me the strength to keep going. You don't know how grateful I am for the endless love you give me each day. I love you.

To you, who are my greatest inspiration and deepest motivation, I dedicate this achievement.

Per aspera

Ad astra.

List of Acronyms

The following acronyms are used throughout the thesis.

CPS4R	Continuum Four-node plane stress element, reduced integration
FEA	Finite Element Analysis
FEM	Finite Element Method
gs	galleried stereom located at suture
gt	galleried stereom located at tubercle boss
imp	imperforate stereom
INGV	National Institute of Geophysics and Volcanology
l	labyrinthic stereom
NMDS	Non-Metric multidimensional scaling
opl	open labyrinthic stereom
p	perforate stereom
RVE	Representative volume elements
SEM	Scanning Electron Microscopy
X-ray	X-radiation
µCT	Micro-computed tomography

AVGVSTVS FRIDERICVS ROMANORVM IMPERATOR SEMPER

List of Figures

AVGVSTVS FRIDERICVS ROMANORVM IMPERATOR SEMPER

List of Tables

AVGVSTVS FRIDERICVS ROMANORVM IMPERATOR SEMPER

List of Symbols

The following symbols are used within the thesis

component

A_o	Total Area
C	Connectivity
C’	Stiffness tensor expressed in rotated reference
Ca	Calcium
Circ	Circularity
$\bar{C}_{11}^{p}$	Average value of principal longitudinal stiffness
C_{ij}^{p}	Components of C in the principal material reference frame
C_{ji}	Components of the homogenised stiffness tensor
C_r	Rotated stiffness tensor
E	Young’s Modulus
ε_i	Strain components
ϵ	Strain tensor
l_c	Chord length
l_t	Curved length
M	Rotation matrix for a stiffness tensor C’
Mg	Magnesium
n	Nodes
N	Number of Pores

n_1	Direction of maximum longitudinal stiffness
n_2	Direction of intermediate longitudinal stiffness
n_3	Direction of minimum longitudinal stiffness
n_i	Base unit vector of the Stiffness principal reference
p	Points
P	Porosity
p	Wilcoxon Mann-Whitney test results probability of the “z score
Perim	Perimeter
r	Radius
R	Rotation matrix for a stiffness tensor C_r
s	Segments
S	Area of the stereom RVE
S11	Normal stress along the horizontal direction
S12	Shear stress
S22	Normal stress along the vertical direction
T	Local thickness
T	Stress tensor
th	Thickness
tr	Tortuosity
$\bar{\sigma}_j$	Average value of the stress component σ_j
$\theta_{\max}$	Rotation Angle identify the direction of higher stiffness
σ_j	Stress components
v	Poisson’s Ration
V	Volume of the stereom RVE
z	Wilcoxon Mann-Whitney test results “z score”

AVGVSTVS FRIDERICVS ROMANORVM IMPERATOR SEMPER

Chapter 1

Introduction

Echinoids, known as sea urchins, are a highly successful class of invertebrates that have populated the sea for more than 450 million years. Throughout their evolution, they have developed a calcitic skeletal structure that effectively adapts to withstand various environmental challenges. This is achieved by combining an ultra-lightweight design with improved strength and impact resistance. The skeleton consists of a porous 3D lattice-like meshwork, known as the stereom, which displays unique structural, compositional, and crystallographic heterogeneities capable of meeting local mechanical needs. Structural gradients of various trabecular geometry, topology, orientation, and composition can be detected at different scales, leading to species-specific patterns with emerging mechanical properties.

The constructional concept and related working principles of the echinoid skeleton offer valuable insights for improving the mechanical behavior of building constructions and materials. By understanding and emulating the echinoid's skeletal design, it is possible to develop building materials that are both lightweight and robust, with enhanced impact resistance and structural integrity (Perricone et al., 2020).

This approach that combines the understanding of natural structures, systems, and processes with their abstraction and translation into technological applications is known as “Biomimetics” or “Biomimicry”. Nature has long been a source of inspiration for human innovation and important figures in the world of architecture and engineering consciously choose to use this approach leading to original creations and technologies, such as such as Leonardo Da Vinci, Antonio Gaudi, Frei Otto, Pierluigi Nervi, Joseph Paxton, Santiago Calatrava, Renzo Piano and Peter Pearce (Bhushan, 2009;

Gebeshuber and Drack, 2008; Gebeshuber, Gruber and Drack, 2009; Knippers and Speck, 2012; Speck et al. 2017). Indeed, natural organisms have evolved structural solutions over millions of years to solve complex problems related to strength, flexibility, and resilience, often under extreme environmental conditions leading to groundbreaking technical innovations in building constructions

This transfer of biological solutions is facilitated by numerous analogies between organisms and building constructions, encompassing their components, behaviors, and functions. For example, an infinite variety of optimized shell structures can be found in nature, each designed to effectively bear a wide range of loading conditions (e.g. Marmo et al. 2022). Notably, some, such as Acanthocardia, Pecten, or Tridacna seashells (Fig. 1.1A), utilize corrugation to enhance the structural performance of their shells. This strategy of shell corrugation has been effectively adopted in structural engineering (Fig. 1.1B) to increase shell stiffness and strength under varying loading conditions, with only a minimal increase in structural thickness and weight (Michels et al., 2019; Marmo et al., 2019).

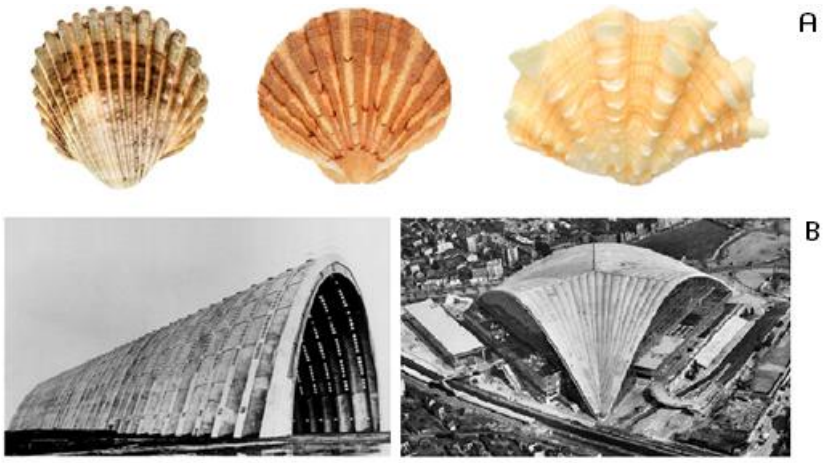

Figure 1.1. Corrugation in seashells (Acanthocardia, Pecten, and Tridacna) and in architecture (Hangar in Orly, CNIT in Paris).

In this context, the present doctoral dissertation entails an in-depth analysis of the echinoid skeletal variability with the aim of acquiring

new insights into the ultra-structure configuration and its mechanical functional meaning. This research focuses on the application of biomimetic principles derived from echinoid skeletons to building engineering, with the goal of improving construction materials and structural designs.

Accordingly, the thesis is organized as follows:

I. **Introduction**: Chapter 1 contains the introduction to the thesis through a general overview.

II. **The Echinoid Skeleton and Biomimetic potentialities**: Chapter 2 provides an overview of the constructional morphology and biomechanics of the echinoid skeleton, along with insights into bioinspired design principles.

III. **The 2D Analysis of the Echinoid Microarchitecture**: Chapter 3 focuses on the geometrical variability and mechanical responses of the microarchitecture present in the *Paracentrotus Lividus* interambulacral plates.

IV. **The 3D Analysis of the Echinoid Microarchitecture**: Chapter 4 includes a comprehensive structural characterization and mechanical evaluation using a combination of micro-CT analysis, image analysis, and finite element analyses (FEA).

V. **The echinoid plate: microstructural variation in relation to the main sustained mechanical stresses**: Chapter 5 evaluates the microstructural variation in relation to the main sustained mechanical stresses, providing insights into the design principles that can be applied to building materials.

VI. **Conclusion and Further Perspectives**: Chapter 6 summarizes the findings and discusses potential future research directions and applications in building engineering.

Through this comprehensive analysis, the dissertation aims to bridge the gap between biological inspiration and engineering application, contributing to the development of innovative building materials and structures inspired by the remarkable design of echinoid skeletons.

Chapter 2

The echinoid skeleton and biomimetic potentialities

In the course of time, the unique constructional design of the echinoid endoskeleton has attracted the attention of researchers from different scientific fields due to its unique morphology, structure, and material properties. Echinoids are highly adapted to different marine environments: the extant groups of regular and irregular sea urchins are widely distributed from the equator to the poles, from the bright shallow waters to the dark and cold deep sea. The evolutionary success of echinoids is certainly due to the massive strategic employment of their endoskeleton displaying numerous functional details.

The endoskeleton consists of three main structural components: skeletal structures known as tests, dental apparatus, and accessory appendages. All parts of the echinoid skeleton consist of the same basic high-magnesium calcite material; however, their microstructure displays great potential in meeting several mechanical needs according to a direct and clear structure-function relationship. This versatility has allowed the echinoid skeleton to adapt to different activities such as structural support, defense, feeding, burrowing, and cleaning. Although constrained by energy and available resources, many of the structures found in the echinoid skeleton are optimized in terms of functional performances and, consequently, can be used as role models for bio-inspired solutions in various industrial sectors. The geometry of the test, including its interlocking plate structure and porous yet robust framework, offers valuable insights into the development of synthetic materials that mimic these natural advantages. Additionally, the regenerative capabilities and self-

sharpening spines of some echinoid species present further opportunities for innovation in material science.

The present chapter provides an overview on echinoid skeletal structures, focusing attention on the main morphological features and mechanical aspects of the test and stereo.

2.1 Echinoids as a source of bioinspiration

Echinoids, commonly known as *sea urchins*, are a class of marine invertebrates belonging to the phylum Echinodermata and the class Echinoidea. Characterized by their spiny exoskeletons, echinoids are a diverse and ecologically significant group found in oceans worldwide, from shallow coastal waters to the deep sea. Their distinctive morphology, complex behaviour, and varied ecological roles make them an important subject of study in marine biology and ecology. Echinoid skeletal components are structurally and functionally organized regarding, among others, lightness, stability, strength, flexibility, and stress resistance. Presently, due to the availability of novel analytical methods, the underlying principles can be better understood and transferred into building constructions and industrial products (Speck et al., 2017).

The evolutionary success of echinoids is undoubtedly due to the strategic employment of their endoskeleton, macroscopically consisting of three main functional components: *test, dental apparatus (Aristotle's lantern), and accessory appendages (such as spines and pedicellariae)* (Allasinaz, 1995; Nebelsick et al., 2015).

During evolution, the echinoid skeletal parts underwent morphological and physiological modifications adapted to novel functions (Seilacher and Gishlick, 2014). In the meantime, progressive modifications led to increased specialization and adaptation of these skeletal parts in efficiently perform specific mechanical roles. In particular, spines and test protect the animal by withstanding *biotic* (e.g. predatory attacks) and *abiotic* (e.g., strong wave motion or substrate impact during burrowing or locomotion) mechanical stresses (Cavey and Märkel 1994; Guidetti and Mori, 2005; Lawrence, 2001; Nichols, 1967; Strathmann, 1981; Telford and Harold, 1982;

Wainwright et al., 1976; Grun and Nebelsick 2018a); pedicellariae, provide further defence and are used for cleaning the echinoid's epidermis (Coppard et al., 2012; Von Uexkull, 1899). Aristotle's lantern plays a direct role in multiple activities such as gripping, scraping, digging, and even locomotion (Jensen, 1984).

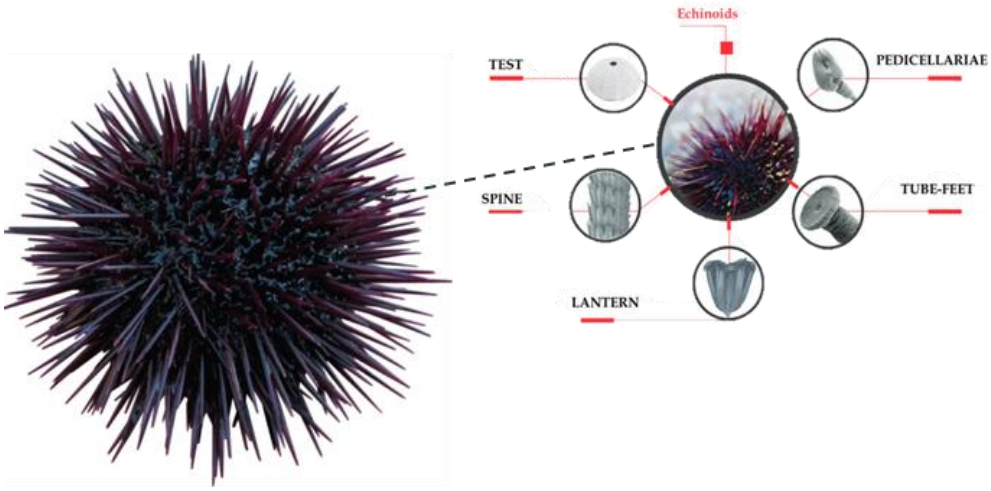

Figure 2.1 Constructional design of echinoid endoskeleton: main structural components and their potential for biomimetic applications.

Due to its unique features, it is not surprising that the constructional design of the echinoid skeleton has attracted the interest of both biologists and engineers. Accordingly, mechanical engineering and material science principles, methods and tools have been applied in exploring the mechanical performances of sea urchins as an integrated system or single component urchins (e.g., Grossmann and Nebelsick, 2013; Grun et al., 2018a,b; Grun, and Nebelsick, 2018a,b,c; Lauer et al., 2018; Philippi, and Nachtigall, 1996; Presser et al., 2009; Seilacher, 1979; Telford, 1981; 1985; Wainwright et al., 1976). This biomechanical approach provided important biological insights on form-function skeletal features, taxa comparisons, ecological and evolutionary trends and adaptive role, as well as new functional principles used to design innovative bioinspired technical solutions (Grun et al., 2016; Grun et al., 2018b; Grun, and Nebelsick, 2018a; Nebelsick, 2015; Klang et al., 2016; Knippers et al., 2016; Presser et al., 2011; Wester, 1984). The study of bioinspired materials based on echinoids represents a dynamic and promising

field of research. By harnessing the unique structural and mechanical properties of these marine organisms, scientists and engineers can develop innovative materials that meet human needs while aligning with principles of sustainability and efficiency.

Echinoids have a long history as inspiring models for engineering structures. This interest has recently increased, regarding rotationally symmetrical constructions, defined as echinodomes (e.g., Ibidapo-Obe, Royles and Sofoluwe, 1981; Bramski, 1981). Detailed analyses of these structures including their mechanical advantages and limits have been technically described and generally well understood. Different load conditions, such as self-weight, snow loads, wind and hydrostatic loads, which can generate over- or under-pressure, can be calculated adapting constructions to specific mechanical needs and functions (Bramski 1981). Echinodomes have been applied to several constructions including long-term storage containers for gas and liquid fuels such as automobile and aircraft gasoline, mineral oil, and other volatile substances (Bramski, 1981). The advantages of echinodomes are specifically due to their thin-shelled and double-curved architecture that results in mechanical behaviour predominantly following the membrane theory, i.e., in-plane membrane stress, reduced bending stress (e.g., Bramski, 1981; Bletzinger and Maute 1995, Tamboli et al., 2000; Schodeck and Bechthold, 2015).

Additional studies have not only focused on the overall shape of an echinoid test, but also on specific working principles that have recently been implemented in civil engineering. Grun et al. (2016, 2017, 2019) provided an overview on echinoid skeletal strategies in building constructions, by identifying in the skeleton various structural working principles on different hierarchical levels and their transfer into demonstrators. These are architectural constructions providing a proof-of-concept of specific functional aspects. Transferred structural principles based on echinoid skeleton include: 1) mosaic-arranged plates, where three plates meet at one point to avoid straight edges, which may cause kinking; 2) clerestories-type plates, interconnected by skeletal protrusions leading to secure plate interlocking; 3) fiber-connected plates; 4) light-weight constructions; 5) double-wall constructions as found in Clypeaster rosaceous. Both structural elements and processes leading to specific echinoid morphologies have been investigated (CIT).

Plate distribution has been optimized using the echinoid skeleton as a role model (Grun et al., 2016, Schwinn et al., 2019), and high-performance structures, identified and analyzed, have been abstracted and transferred in various ways into demonstrators. For example, the ICD/ITKE Research Pavilion 2011 (Fig 2.2A) (e.g., Knippers et al., 2013; Grun et al., 2016, Schwinn et al., 2019) has well demonstrated the application of three structural principles among those cited above: 1) mosaic-arranged modules, where three modules meet in one point; 2) single hollow modules, made from multi-elements reflecting a lightweight construction; 3) modules interconnected by comb-joints. Similarly, building construction in the form of the Landesgartenschau Exhibition Hall 2014 was realized (Fig 2.2B) (Schwinn et al., 2014; Krieg et al., 2015; Li and Knippers, 2015; Schmitt and Schwieger 2015; Grun et al. 2016; Schwinn et al., 2019). A second ICD/ITKE Research Pavilion developed in 2015 (Fig 2.2C) focused on 1) module arrangement; 2) comb-joint refinement; 3) material differentiation using textile connections; 4) light-weight construction; 5) a double-shelled structure; 6) an evolutionarily optimized growth construction algorithm (e.g., Grun et al., 2016; Schwinn et al., 2019). In 2018, the Rosenstein Timber Pavilion was exhibited demonstrating further developed, high-performance characteristics based on echinoid skeleton, focusing on improved plate connections and optimized plate distribution (Schwinn et al., 2019). Furthermore, these characteristics have also inspired the BUGA wooden pavilion (2019, ICD/ITKE University of Stuttgart) (Fig 2.2D), which was realized combining a new digital design approach for shape-funding structures with an automated robotic manufacturing using wood, thus receiving the German Design Award 2020 in the "Excellent Architecture" category (Schwinn et al., 2019).

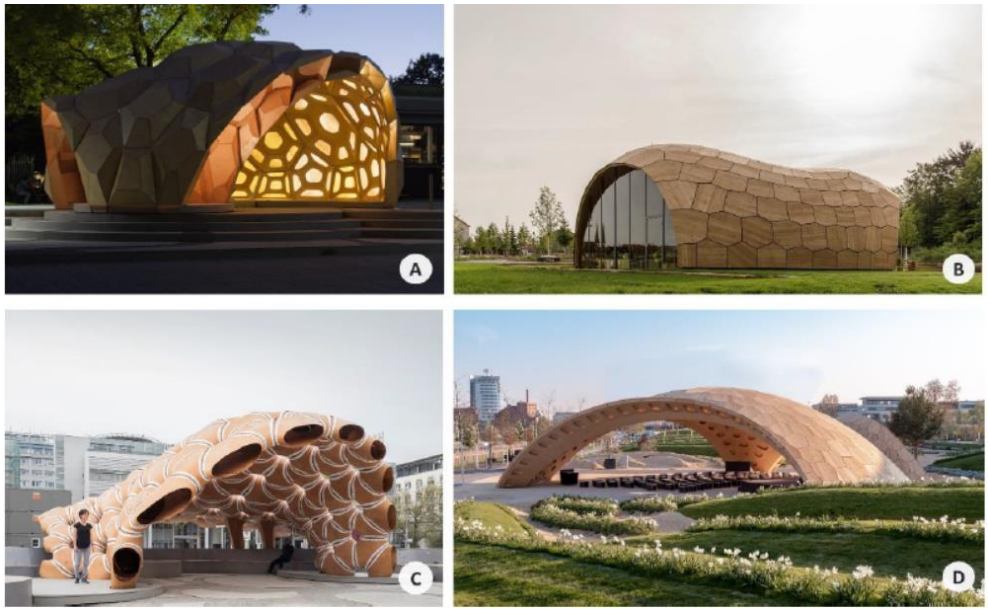

Figure 2.2. Echinoids in Architecture. Research pavilions and building constructions inspired by both morphological and mechanical principles of the genera *Clypeaster and Phyllacantus*. A) ICD/ITKE Research Pavilion 2011. B) Landesgartenschau Exhibition Hall 2014. C) ICD/ITKE Research Pavilion 2015-16. D) BUGA Wood Pavilion 2019 (© Photo A-D of Prof. Jan Knipper, obtained from the Institute of Building Structures and Structural Design website, University of Stuttgart).

2.2 Model Description of *Paracentrotus Lividus*

The regular echinoid *Paracentrotus Lividus* has been chosen as a biological model. *Paracentrotus Lividus* is a regular echinoid belonging to the *Parechinidae* family. It is characterized by a circular-flattened test with a diameter of no more than 6-7,5 (Bonnet, 1925; Boudouresque et al., 1989; Lozano et al., 1995). Although the popular name is ‘purple sea urchin’, its color is variable: black-purple, purple, red-brown, dark brown, yellow-brown, light brown, or olive green.

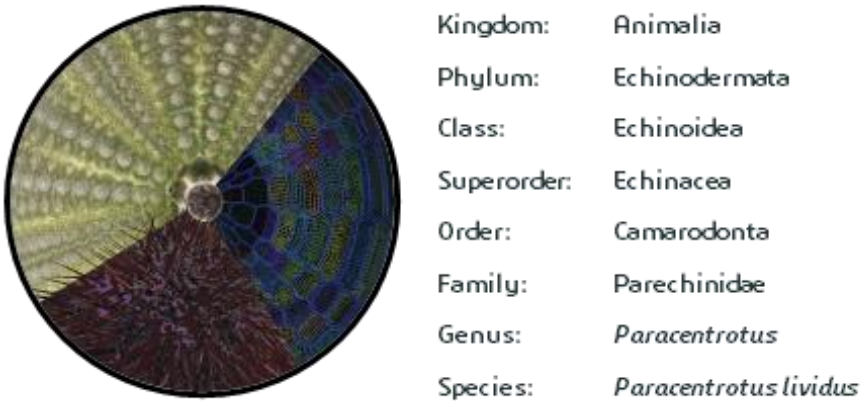

Figure 2.3. *Paracentrotus Lividus*

Paracentrotus Lividus is omnivorous, feeding on vegetal and animal materials and an opportunistic generalist: moving from a rare, preferred resource to an abundant but less preferred one. In shallow water environments, *Paracentrotus Lividus* can drastically affect the abundance and distribution of photosynthetic organisms (including seagrasses) playing a key role in the ecosystem functioning (see reviews by Lawrence, 1987; 2001).

The test *Paracentrotus Lividus* was chosen among the skeletal components for an in-depth study to acquire new biological knowledge regarding its mechanical design and adaptive strategies. The test surface is composed by long and sharply pointed articulated spines. The role of the echinoid test is to support and protect visceral organs; it must be robust enough to withstand external forces and moments, but also flexible enough to allow growth and movement. Consequently, this skeletal system can be investigated as an engineering structure on which it is possible to apply mechanical notions The echinoid skeleton (test), in fact, presents interesting functional features on their macro and microarchitectures, mechanical performances, and material properties. This hierarchical design fulfils several functional principles acting as a lightweight and load-bearing system adapted to withstand biotic and abiotic stresses. Due to its functional strategies, the echinoid test has a long history as an inspiring model for engineering structures and materials.

2.3 The echinoid test of *Paracentrotus Lividus*: the system of plates and sutures

In structural engineering, the use of efficient structural systems provides the double advantage of reducing the impact of the construction processes on the environment and obtaining structures that resist extreme loadings (e.g. earthquakes, volcanic eruptions, and floods). Owing to their geometric stiffness and reduced mass, shell structures represent one of the most efficient structural systems to resist actions that generally affect constructions. The efficiency of shell structures is mainly owing to their geometry since this is characterized by a thick curved surface having two large dimensions (mid-surface) and a smaller one (thickness). However, similarly to several structural systems, their efficiency is also related to the distribution of internal forces, namely membrane forces, bending moments, and out-of-plane shears (F. Marmo et al., 2022).

In this respect, structural optimization techniques, widely employed to design shell structures and referred to as form-finding methods, aim at defining the geometry of the shell mid-surface so that applied loads can be equilibrated mainly by membrane forces (S. Adriaenssens et al., 2014). In fact, structural solutions that minimize bending moments in favor of membrane forces are desirable when optimization of material exploitation is a primary goal. However, the optimal configuration of structures is strongly related to every specific load case and is unlikely adaptable to all load conditions that a real structure is expected to resist (F. Marmo et al., 2022).

On the other hand, a large amount of optimized shell structures, designed to effectively sustain a variety of loading conditions, can be found in nature. Numerous living organisms employ protective shells against predators or external abiotic loadings. Some of them, such as *Acanthocardia*, Pecten, and Tridacna shells, use corrugation as a strategy to optimize structural performance (Wainwright SA et al., 1976). Actually, the efficiency of shell corrugation has been successfully employed in the construction industry to increase shell geometric stiffness and strength against loading variability with a limited increase of structural thickness and weight (T. Michiels et al., 2019).

A completely different solution is *shell tessellation* which amounts to partitioning the shell mid-surface into a series of patches united by compliant joints. Shell tessellation does exist in numerous organisms and provides a range of interesting mechanical properties at different scales (from molecular to macroscopic arrangements), such as crack propagation prevention, flexibility, and protection for biological shells and armors (P. Fratzl et al., 2016). An outstanding example of a tessellated shell is observed in echinoids, known as sea urchins.

Echinoids are particularly noteworthy for their intricate and robust exoskeletons, defined as test (*hard shell*) or echinodome [DM. Raup, 1966; JN. Weber, 1969; O. Ibidapo, 1981; M. Telford, 1985], that consists of a coherent and resistant dome-shaped and tessellated shell structure (figure 2.4), composed of a series of polygonal skeletal plates (hundreds of calcite plates) joined by flexible sutures that are skeletal protrusions and collagenous fibres (ligaments). (M. Telford, 1985; ML. Moss, 1967; O. Ellers et al., 1998; A. Seilacher, AD. Gishlick, 2014; JH. Nebelsick et al., 2015; V. Perricone et al., 2020). These sutures can be characterized by the presence of interdigitating articular surfaces (finger-joints) often bound together by short collagenous ligaments (Duncan, 1882; Ellers et al. 1998; Grun and Nebelsick, 2018a, b; Lawrence, 1987; Nebelsick et al., 2015; Pearse and Pearse, 1975; Seilacher, 1976; Telford, 1985 a, b). This design fulfills several mechanical and biological functional principles acting as a resistant, lightweight, and load-bearing system adapted to withstand biotic (e.g. predatory attacks) and abiotic (e.g. environmental forces such as fluid flow and pressure) mechanical stresses [SA. Wainwright et al., 2019; U. Philippi, W. Nachtigal., 1995; O. Ellers, M. Telford, 1992; A. Seilacher, 1979; TB. Grun, JH. Nebelsick, 2018; S. Vogel, 2013)]. The most important function of the test was to support and protect the soft body inside. Additionally, the tessellated configuration is functional for the echinoid test growth since sutures guarantee a space between plate margins (plate gapping) so that each plate can continuously expand while interacting with the adjacent ones (M. Abou Chakra, JR. Stone, 2011).

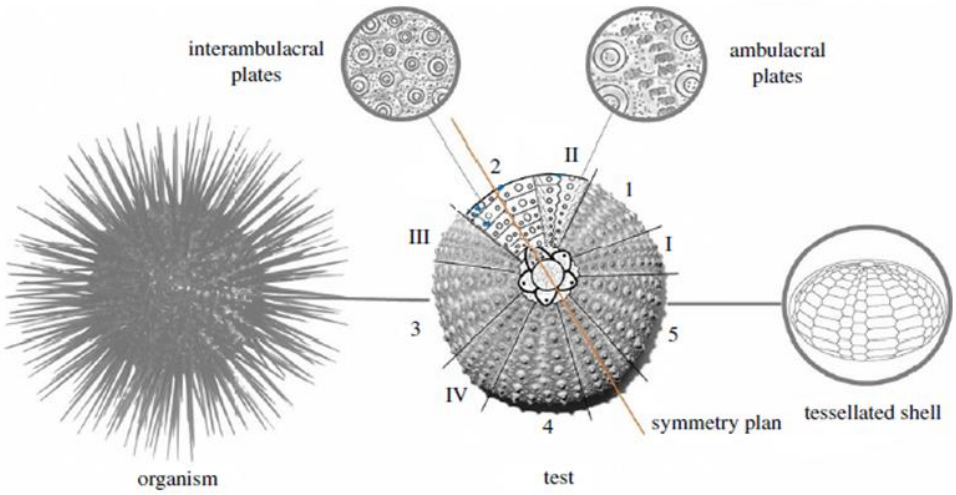

Figure 2.4. Regular echinoid. Schematic reconstruction of a regular echinoid, its skeletal test in aboral view, and functional characteristic of a tessellated shell structure. The aboral view shows the subdivision in ambulacral (I–V) and interambulacral (1–5) zones along with respective plates and the symmetry plan (F. Marmo et al., 2022).

Echinoid test have a variety of shapes; they can be globular or flattened, rounded or heart-shaped.

At the macroscale level the test of echinoid (sea urchin), which is its external skeleton, is a rigid, globular structure made up of fused calcareous plates, and covered with small knobs (tubercles) to which spines are attached in living echinoids. The test and spines are the parts normally found as fossils. The spines like as echinoid's test are composed of calcium carbonate in the form of calcite.

The individual plates of the echinoid test are highly variable in morphology and their form is closely related to specific functional aspects (A. B. Smith, 1980). These skeletal plates consist of integrated inorganic and organic components. The inorganic component, composed of magnesium-rich calcite (C. E. Killian et al., 2008), is a lightweight structure characterized by a porous arrangement (stereom) and is extremely variable in its density and microarchitecture. The organic component (stroma), which fills and permeates the inorganic stereom, is a true connective tissue consisting of cells, extracellular matrix (ECM), and collagen fibril bundles (A. B. Smith, 1980), (P. Gorzelak, 2021). The stroma significantly contributes to the integrity of

the skeletal structure by providing mechanical robustness and flexibility (A. Smith, et al, 1990).

Based on their skeletal morphology and lifestyle, echinoids are divided into two groups:

a) *regular*, which is characterized by a radial symmetry, herbivorous/carnivorous, and epifaunal (i.e., living on the ocean bottom surface) lifestyle;
b) *irregular*, having a bilateral symmetry and tending to be deposit feeder and infaunal (i.e., living buried in the ocean bottom) (R. C. Brusca, 2021).

In regular echinoids, the overall test forms an evident pentaradial symmetrical structure, where pseudo-hexagonal plates are systematically arranged in four pentameric systems:

1) coronal system, composed of 10 meridian areas divided into
   - five *interambulacral areas*, composed of larger plates (interambulacral plate) that lack tube feet. They mainly provide structural support and protection to the sea urchin. Spines, which are used for defense and mobility, are attached to these plates.
   - *five ambulacral areas*, composed of smaller plates (ambulacral plate) with pores through which tube feet extend. The tube feet, which protrude through these plates, are used for locomotion, feeding, and respiration. They also contain sensory cells that help the sea urchin navigate its environment. The plates of the ambulacral zones are typically pierced by pores (two series) for the tube-feet protrusion, these pore-pairs are located and aligned along the outer (adambulacral) margins of the plates.
2) apical system, consisting of 5 genital plates, alternating with 5 smaller ocular plates and the madreporite.
3) periportal system, is constituted by plates arranged in an irregular circle covering the membrane on which the anus opens.
4) peristomatic system, consisting of numerous plates protecting the membrane between the adoral margin of the coronal system and the mouth (Brusca and Brusca, 2003).

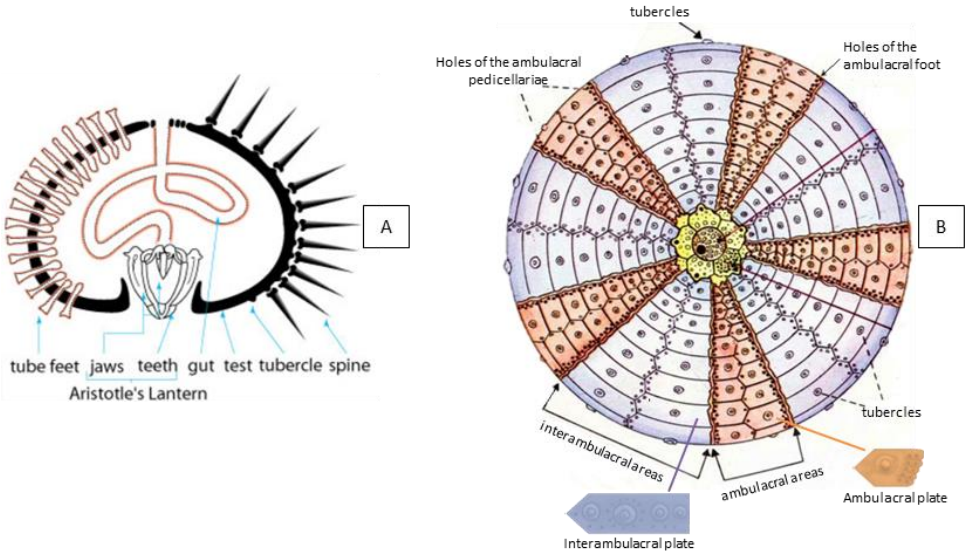

Figure 2.5. Morphology of regular sea urchin. A) Simplified cross-section through a living echinoid. B) Aboral view of regular sea urchins (without spines).

Since all plates bear movable spines, their outer surfaces display rounded tubercles on which the spines are articulated by balland-socket joints. The tubercles are constructed by a ball-like"mamelon" at the center, where the spine is articulated and usually imperforated (A. B. Smith, 1980).

The mamelon is situated at the apex of the "boss", a conical mound representing the attachment site for the connective tissue, generally composed of galleried stereom (A. B. Smith, 1980). The "areole" is the area surrounding the base of the boss and is composed of a fine labyrinthic stereom (A. B. Smith, 1980). The spine attaches to the tubercle by an inner ring of collagenous fibers, called the "catch apparatus", and an outer ring of muscle fibers (generally described as "smooth") (S. Kawaguti et al., 1965), (K. TAKAHASHI, 1967).

Catch apparatus fibers are inserted within the boss and bound around the trabeculae. Muscle fibers are attached to the areole stereom through connective tendons. Finally, a fluid-filled space separates the muscle fibers from the catch apparatus (A. B. Smith, 1980).

This constructional design fulfils several mechanical principles acting as a resistant, lightweight, load bearing and load-transferring system, as well as being an attachment point for appendages. Structural strength is achieved by hierarchical constructional adaptations, such as: overall shape, plate layout and arrangement (trivalent vertex arrangement, in which three plates meet in one point), skeletal interlocking and reinforcements (e.g. internal buttressing), material distribution and stereom diversity (Ellers et al., 1998; Grun et al., 2018 a, b; Grun and Nebelsick, 2018a,b,c; Mihaljević, Jerjen and Smith, 2011; Nebelsick et al., 2015; Smith, 1980; Terlford, 1985a,b; Wester, 2002). These skeletal features have been described as functional strategies which, suitably combined with adaptations of the connective tissue components, allow the echinoid test to withstand compressive, tensile and bending stresses (Ellers et al., 1998; Grun and Nebelsick, 2018a; Grun et al., 2018a; Telford, 1985 a,b; Marmo et al. 2019).

Due to the structural form and architecture of the test, echinoids have been extensively investigated in order to understand their constructional design and mechanical behaviour in detail (Currey, 1999; Seilacher 1979; Telford 1985; Philippi and Nachtigall 1996; Chakra and Stone 2011; Mihaljević et al., 2011; Zachos, 2009, 2015; Grun et al., 2018 a; Grun and Nebelsick, 2018a; Pearse and Pearse, 1975; Wester, 1984; Wainwright et al., 1976).

The geometry of the spines and the arrangement of the plates in the test, often featuring a porous yet highly organized framework, provide insights into creating materials that are both strong and lightweight. Moreover, the regenerative capabilities and self-sharpening spines of some echinoid species offer further avenues for innovation in material design.

Detailed morphospace analyses were carried out to explain and predict extinct and extant echinoid test shapes by considering possible phylogenetic, physical, and mechanical factors (e.g., Dafini, 1986; Ellers, 1993; Mihaljević et al., 2011; Moore and Ellers, 1993; Raup, 1968; Thompson 1917). Thompson (1917) in particular, carried out a pioneer study on test shape using a liquid drop analogy to describe the shape and growth of regular echinoids. Ellers (1993) supported this hypothesis using the thin shell theory to explain test curvature defining the echinoid morphospace in two parameters: 1) the apical

curvature; 2) a proportion of the vertical gradient of pressure to the internal coelomic pressure. Seilacher (1979) proposed that the echinoid test should be analysed as a mineralized pneumatic structure that grows when the internal pressure exceeds the internal one, varying its morphology through plate growth. However, Ellers and Telford (1992) measured the internal coelomic pressure in the regular sea urchin Strongylocentrotus The samples were completely and Lytechinus variegatus. They found that internal pressure fluctuates rhythmically about -8 Pa and was negative for 70% of the time, disempowering the pneumatic hypothesis that requires an internal positive pressure. These rhythmical fluctuations in pressure could be mainly caused by the lantern movements that change the curvature and tension of the peristomial membrane. Telford (1985) analysed the test as a dome structure utilizing both the membrane theory and static analysis to determine its behaviour under different loads; thereby assessing the hypothesis that the test form was constructed to resist external forces. Overall, considering these and other studies, test form and growth were described and explained using different theoretic models, based on a total of nine hypotheses, in addition to different computational models (Baron, 1991; Dafni and Erez, 1982; Raup, 1968; Moss and Meehan, 1968; Zachos, 2009; reviewed in Chakra and Stone, 2011). The echinoid test growth is mainly based on two combined processes, namely: plate addition, i.e., the insertion of new plates in the apical system, and plate growth, based on a peripherally accretion or reabsorption of skeletal material.

Modern methods such as 3D acquisition (e.g., µCT and photogrammetry), digital modelling and simulation, e.g., Finite Element Analysis (FEA) are recently being adopted, providing novel answers to questions about test morphology, functional performance, and mechanical behaviour (Fig. 2.5) (Rayfield, 2007). As pioneers in this field, Philippi and Nachtigall (1996) conducted FEA-analysis describing the behaviour of the regular echinoid test (Echinus esculentus) under diverse loads. Their studies highlighted the structural load-bearing efficiency of the test and interpreted its peculiar spherical shape as the most adapted form to sustain the tensile stresses resulting from the tube feet activity. Recently, Grun and co-workers focused on the clerestoried skeleton using X-ray µCT, SEM observations and physical and virtual tests to analyse the hierarchical structural design of the Echinocyamus poilus test (Grun et al., 2018a;

Grun and Nebelsick, 2018a, b). They displayed in detail the mechanical properties of the test at different hierarchical levels, i.e., from the overall shape - although consisting in a discontinuous structure divided into several polygonal plates, it behaves as a monolithic structure - to the plate micro-architecture, internal supports and stereom variability, all described as specific functional devices for bearing and transferring loads.

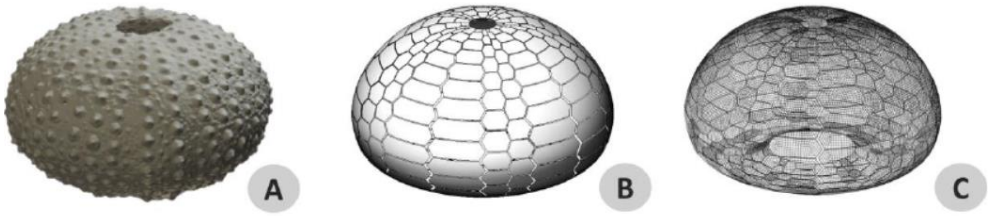

Figure 2.6. Virtual models of *Paracentrotus Lividus's* test. A) 3D model obtained with a photogrammetric reconstruction. B) Parametrized geometry model with visible plates and sutures. C) 3D mesh used for Finite Element Analyses.

2.4 Stereomic microstructure of the echinoid test

Echinoids are particularly noteworthy for their intricate and robust exoskeletons, that consists of a dome-shaped and tessellated shell structure, defined as a "test" (hard shell), composed of a series of skeletal plates joined by flexible sutures that are skeletal protrusions and collagenous fibres (ligaments). Shell structures are geometrically defined as three-dimensional-curved solids in which thickness is much smaller than the other two dimensions.

At the microscale, is possible to observe that each skeletal plates of the echinoids'test, ambulacral and interambulacral, consists of high magnesium calcite material, displays a complex 3D microarchitecture, variable both in porosity and in architectural design (H.-U. Nissen, 1969), (J. N. Weber, 1969), (J. Weber et al., 1969). These ambulacral and interambulacral plates are composed of *stereom* (Bather, 1891); It has a porous, lattice-like structure, resembling a three-dimensional mesh of trabeculae, i.e., struts, of or sponge-like microstructure, made of made of bio calcite (Smith 1980).

In other words, each plate of the echinoids'test consists of high magnesium calcite material arranged in a porous three-dimensional lattice-like meshwork (stereom) (AB. Smith, 1980; TB. Grun, JH. Nebelsick, 2018; D. Müter et al., 2015)

The porosity of the stereom varies; it can range from very fine to quite open, depending on the specific function and location of the plate within the test. The interconnected pores allow for the lightness and strength of the test, optimizing it for the needs of the sea urchin.

The stereom is highly complex and varies widely. It represents a key element responding to the principles of robustness, lightness and stability, due to three primary factors:

1) material composition and related mechanical properties based on material variations through strategic substitution of calcium (Ca) with magnesium (Mg) in the calcite crystal, and alterations of fracture behaviour due to the incorporation of organic components and crystallographic alignment (Donnay and Pawson, 1969; Magdans and Gies, 2004; Killian et al., 2009; 2011; Nichols and Currey, 1968; Raup, 1965; Seto et al., 2012; Wang et al, 1997; Weber, 1969; Weber et al., 1969);
2) high structural porosity of about 50% - 75% (Presser et al., 2010; Lauer et al. 2017; Wainwright et al., 1976);
3) large structural variability (related to e.g., phylogeny, functional adaptations, growth rate and soft tissue types) allowing specific mechanical demands to be met (e.g., Emlet, 1982; Candia et al., 1991; Grossmann and Nebelsick, 2013 a,b; Grun et al., 2018a,b; Grun and Nebelsick 2018a,b; Lauer et al. 2017; Muter et al., 2015; Smith, 1980; 1990).

Consequently, this lightweight structure denotes an important adaptive achievement within the entire phylum Echinodermata contributing to its evolutionary success (Emson, 1985; Nichols, 1967; Paul, 1977).

The complex constructional design of the stereom varies from species to species and within both individuals and skeletal elements. The microstructure is characterized by variable oriented trabeculae of different basic types associated in very different combinations,

creating species-specific 3D structural patterns. Nevertheless, known far away in time (Valentin, 1841), this structural variability was described in detail by Smith (1980) identifying ten different stereom types in the test that exist in different combinations to create the species-specific 3D structural patterns within the plates. Based on Smith's classification (1980), these ten stereom types include the imperforate, microperforated, simple perforate, galleried, rectilinear, retiform, laminar, fascicular, labyrinthic and irregular perforate (Fig. 2.7).

All of these can be employed in several combinations, creating species-specific 3D structural patterns easily recognizable in Scanning Electron Microscope (SEM) images (Smith, 1980).

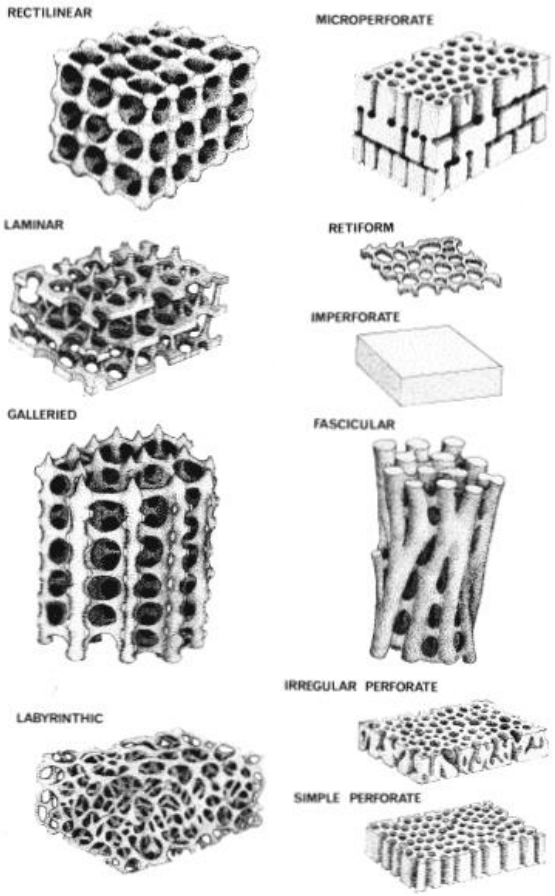

Figure 2.7. Smith's classification of stereom (1980)

In *Paracentrotus Lividus* (Lamarck, 1816), the common regular echinoid of the Mediterranean Sea, four types of stereoms can be detected: imperforate, galleried, labyrinthic and perforate. Although the mechanics of these architectures are well investigated in other skeletal components)

Aristotle's lantern and teeth (M. D. C. Carnevali et al., 1991), (N. Toader et al., 2017), (V. Presser et al., 2009), (J. N. Grossmann et al., 2013), (C. Moureaux et al., 2010), (J. Seto et al., 2012), (R.Wang et al., 1997), (S. R. Stock, 2014), (T. Yang et al., 2020), the evolutionary benefits provided by these stereoms and their combinations in the plates are still not fully understood or analyzed in detail. However, it is highly plausible that the echinoid's structural variability developed as a to species-specific strategy to decrease weight and increase mechanical robustness through density variation and structural specialization similar to design aspects observed in vertebrate bones.

Architectural variability and possible modulations based on specific mechanical needs have been described in several studies regarding:

1) the test and its individual plates (Grun et al., 2018a,b; Grun and Nebelsick, 2018a,b; Muter et al., 2015; Jensen, 1972; Nissen, 1969; Regis, 1977; Raup, 1966; Smith, 1980; Telford, 1985);
2) Aristotle's lantern ossicles (e,g. Carnevali et al.,1991; Stock et al., 2003);
3) more frequently, spines (Grossmann and Nebelsick 2013a,b; Klang et al., 2016; Lauer et al. 2017; Mooi, 1986; Moureaux et al. 2010; Nichols, 1962; Nebelsick et al. 2015; Presser et al. 2009a,b; Regis and Thomassin, 1985; Tsafnat et al. 2012).

As a rule, stereom density tends to increase in regions subjected to high mechanical stresses resulting in imperforate or microperforate types; in particular, this occurs in those areas exposed to high frictional and compressive stresses, such as tubercles (Fig. 2.8 C, E), lantern (Fig. 2.8B), rotulae (Fig. 2.8 C) and spine bases (Nebelsick et al. 2015; Candia Carnevali et al., 1991). Also, the microstructure tends to be specialized in regions subjected to directional tensile stresses, i.e., the sutural areas characterized by galleried stereom, which offers a suitable insertion pattern for the attached ligament bundles (Fig.2.8 C,

D, E; Fig.2.8 D,E) (Carnevali et al.,1991; Grun et al., 2018; Grun and Nebelsick 2018a,b; Nebelsick et al., 2015; Smith, 1980). On the contrary, labyrinthic stereom is found in zones subjected to multi-directional mechanical stresses, such as in the centre of the plates (Fig. 2.8 C,D,E), lantern demi-pyramid (Fig. 2.8 B,C) and in the radiating layer of camarodont spines (Carnevali et al.,1991; Grossmann and Nebelsick 2013b; Smith, 1980): according to Grun and Nebelsick (2018) labyrinthic stereom could equally distribute stresses in multiple directions, thus reducing local stresses.

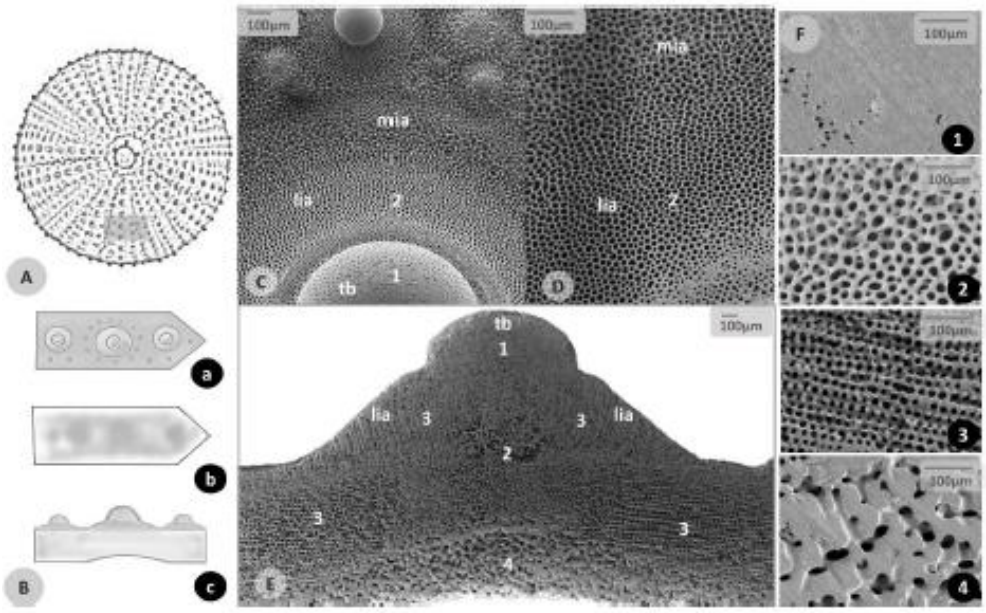

Figure 2.8. SEM micrographs showing microstructure and stereom variability of the test plates. A) Topographic reference of the interambulacral region inspected. B) Schematic reconstruction of an interambulacral plate: (a) top view, (b) internal view, (c) lateral view. C) Top view of *Paracentrotus Lividus* interambulacral plate; D) Enlargement of figure C. Labyrinthic stereom with a variable porous texture is the dominant microstructural pattern. In the wide circular insertion area of the overall catch apparatus, it is possible to distinguish specific stereom patterns related to muscle and ligament insertions, density, and sizes of porosity, closer and more regular in the ligament area. Adjacent to the tubercle where the stereom structure tends to become imperforate, pore size decreases. E) Vertical section of the plate showing a high diversity of the stereom microarchitecture according to zones and related specific mechanical needs. F) Details of stereom types detected: (1) imperforate stereom; (2) labyrinthic stereom; (3) galleried stereom; (4) microperforate stereom. Bar = 100 µm. lia= ligaments insertion area, mia= muscles insertion area, tb= tubercle

The microstructure displays great potential in meeting several mechanical needs according to a direct and clear structure-function

relationship. In the past decades, the mechanical design of the stereom has been extensively studied in a two-dimensional view (Becher, 1914; Becher, 1924; Lawrence, 1987; Jensen, 1972; Regis, 1977; Regis and Thomassin, 1985; Olfield, 1976; Smith, 1980; 1990); however, with the advent of affordable high-resolution computed tomography (CT) scanning, recent studies explored the stereom using 3D modelling reconstruction, 3D topological and structural analysis (e.g., Finite Element Analysis, FEA). These modern methods allow detailed analyses of mechanical properties, lightweight constructions and load-bearing systems (e.g., Grun et al., 2018a, b; Grun and Nebelsick, 2018b; Lauer et al. 2017; Müter et al. 2015; Tsafnat et al. 2012).

2.5 Echinoid test: functional features

The echinoid test, commonly referred to as a sea urchin shell, has several unique and interesting properties that can be transferred or applied to various fields of study and applications. Functional features contribute to the stability of the echinoid structure and influence its mechanical behavior.

To identify the main structural features of the echinoid test and select the ones that significantly contribute to its global structural behaviour, specimens of *P. Lividus* were analyzed in depth both at the macro- and microscale using a stereomicroscope (Leica M205C) and high-resolution scanning electron microscope (JEOL 6700F 250 MK2).

The samples were completely digested via 0.1 N NaOH treatment (for about 1–2 weeks), which completely removed the organic components and provided perfectly clean disassembled plates. Samples were then washed three times in deionized water to remove caustic remains, air-dried, and analysed according to standard scanning electron microscopy (SEM) methods. Different plates were isolated, suitably sectioned, and processed for observation in SEM (at 5 or 10 kV).

Here are reported the functional details and key transferable properties as mechanical support:

1. **Shape**. The test is oblate shaped assuming the form of a flattened sphere and resembling an architectural dome (Telford, 1985). During growth, it acquires this shape presumably resulting in a stable geometry funicular to self-weight and coelomic pressure (Ellers and Telford, 1992). The internal pressure balances the surrounding water pressure and was also found to fluctuate rhythmically at about -8 Pa (Ellers and Telford, 1992) providing the test with compressive compactness. Even though the ideal form of the test should be that of a sphere, downward forces from calcite underwater weight and tube feet pull are most probably the cause of polar flattening (Ellers and Telford, 1992; Philippi and Nachtigall, 1996).

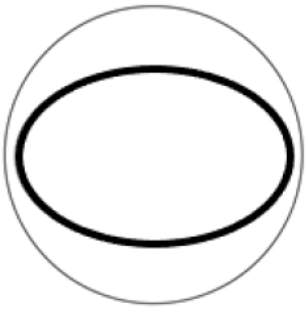

Figure 2.9. Oblate shape of echinoids test

2. **Subdivision into plates**. Macroscopically, the overall echinoid test is a modular tessellated shell structure that forms an evident pentaradial structure, where pseudohexagonal plates are regularly arranged according to 10 double series of plates, respectively, representing alternating five ambulacral and five interambulacral zones (A. Kroh et al. 2020; A. Allasinaz, 1995). The hexagonal modules represent an optimized tessellation of the surface and form a continuous modular grid The ambulacral plates are typically pierced by pores (double series) for tube-feet emergence. These pore-pairs are located and aligned along the outer (adambulacral) margins of the plates. The ambulacral and interambulacral plates have different shapes and functions, providing organisms with great flexibility during growth, greater structural resistance, and damage

limitation (Telford, 1985; Ellers et al, 1998). Piercing loads, such as those caused by predator actions, are transferred through all skeletal plates rather than affecting one. For better comprehension, two types of hollow glass balls can be used as an example: one ball consisting of a single piece and another of many fitted together. Piercing the single-piece ball will result in cracking and in its probable destruction. Conversely, piercing the multiple-pieced ball will cause the cracking of only a single or few pieces, but the overall ball will remain intact. Hence, echinoids prevent test cracking and breaking by distributing impact forces throughout their different test plates (Vogel, 2013).

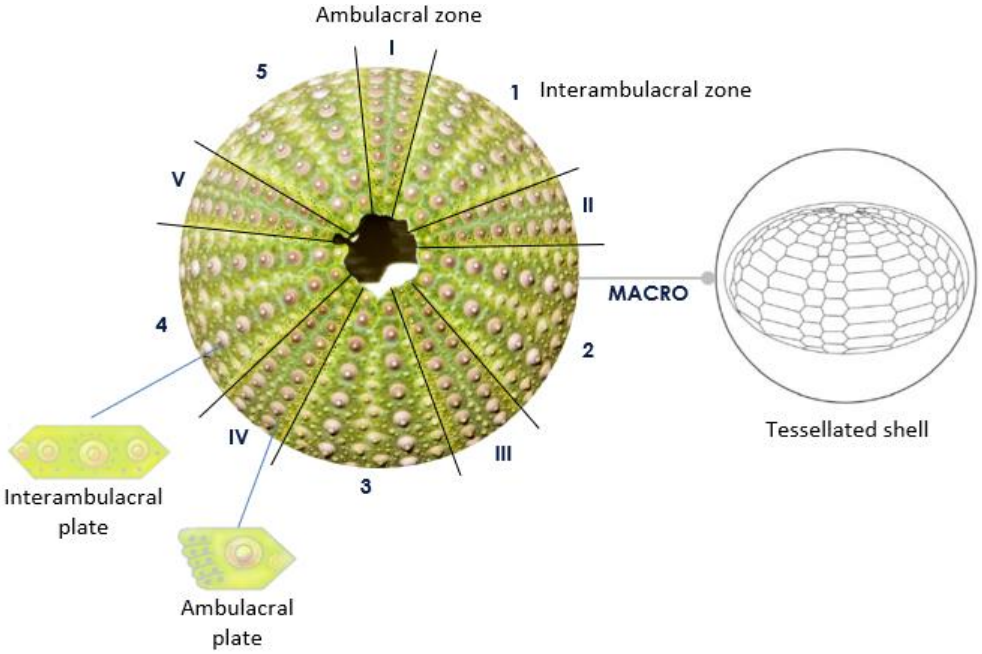

Figure 2.10. *Paracentrotus Lividus's* test: functional details from macroscale. Schematic reconstruction of a regular echinoid, its skeletal test in aboral view, and functional characteristic of a tessellated shell structure. The aboral view shows the subdivision in ambulacral (I–V) and interambulacral (1–5) zones along with respective plates.

3. **Trivalent vertex principle**. In the echinoid test, the plates are arranged following the trivalent vertex principle; in which three plates meet at one point (Wester 1984). This is a stable configuration and a structural pattern characteristic of pure

plate structures, the echinoid test being an outstanding example. As described by Wester (1984) a plate structure consists of plates and lines of support. The forces generated between the plates are only shear forces. Considering a horizontal plate in a three-dimensional space: a plate hinged along one or two lines of support is movable for forces not directed through the intersection points; conversely, a plate hinged along three lines of support is not movable by any direction of forces, resulting in a stabilized plate.

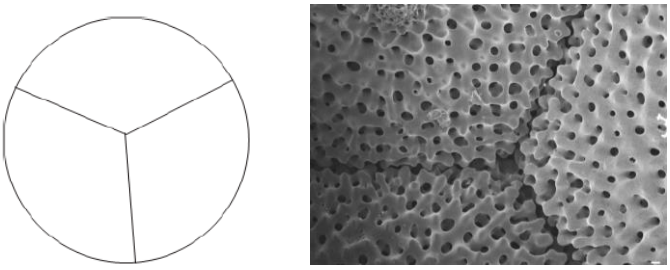

Figure 2.11. Plate arranged as the trivalent vertex principle

4. **Flexible sutures**. Owing to the regular alignment, each ambulacral and interambulacral zone displays longitudinal (radial or meridional) and latitudinal (circumferential) sutures. Radial sutures are:
    i. the perradial suture, between the two series of ambulacral plates;
    ii. (ii) interradial sutures at the midline of each interambulacral zone;
    iii. (iii) the adradial suture, i.e. the longitudinal joints between interambulacral and ambulacral plates.

    Circumferential sutures are adapical, i.e. the upper edge of a plate, and adoral sutures, the lower one (A. Mancosu, JH. Nebelsick , 2020).

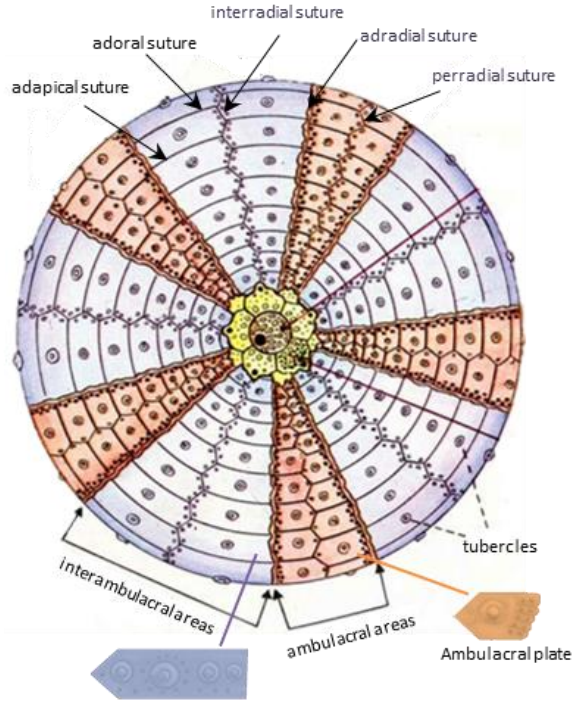

Figure 2.12. Schematic reconstruction of a regular echinoid, its skeletal test in aboral view. The aboral view shows the subdivision in ambulacral (I–V) and interambulacral (1–5) zones along with respective plates joined by flexible sutures.

In detail, the flexible sutures are characterized by the presence of interdigitated articular surfaces (knob-like protrusions) and are bound together by bundles of short collagenous ligaments (M. Telford, 1985; ML. Moss, MM. Meehan 1967).

a) **Finger joints**. *Knob-like spherical protrusions* allowing interlocking between the complementary plates preventing shearing movements (Wester, 2002; Mancosu and Nebelsik, 2020). Under loading, the small plates of the sea urchin test interlock creating a stronger shell structure.

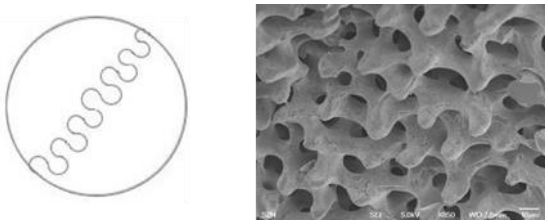

Figure 2.13. *Paracentrotus Lividus's* test: functional details from microscale. Finger joints (knob-like protrusions).

b) **Collagen fibers**. Flexible fibers joining the plates dissipate normal, shear, and flexural forces, increasing the stability of the structure (Ellers et al.1998). The collagen fibers may have an important role in keeping the whole structure assembled by pre-compressing the joints, as well as, in sustaining and transmitting stresses, particularly during the repair period from eventual breakage of one or more plates (Wester, 2002). Additionally, unlike other shells, tests are growing structures composed of articulated hard elements. Thus, collagen-swathed sutures permit growth and local deformation reducing impact loading and therefore offsetting the eventual hazards of a thin shell (Telford 1985).

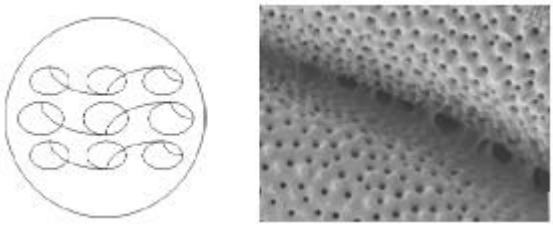

Figure 2.14. *Paracentrotus Lividus's* test: functional details from microscale. Collagen fibers.

5. **Plate curvature**. The plates are visibly curved following the flattened sphere of the test (Telford, 1985). Curved hinges avoid rotation mechanisms even with only one line of support per plate, preventing bending action transfer.

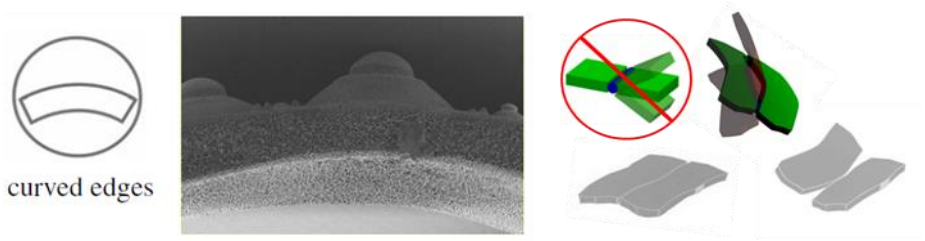

Figure 2.15. *Paracentrotus Lividus's* test: functional details from microscale. Plate with curvature edges.

Owing to their microstructure, knob-like protrusions can prevent shear movements between plates. Collagenous ligaments, on the other hand, avoid plate separation. Hence, the combined effect of knob-like protrusions and collagen fibres makes sutures behave as cylindrical hinges, i.e. they allow relative rotation between plates while preventing sliding. These hinges do not compromise the global stability of the echinoid test since plates are arranged following the trivalent vertex principle, in which three plates meet at one point (T. Wester, 1984; T. Wester, 1990; T. Wester, 2022). As shown by Wester (T. Wester, 1984), the subdivision of a shell structure in different plates and their arrangement in trivalent vertices (Y-shaped) provides stability to the echinoid test as occurs in a panel structure. Interestingly, Wester describes and compares the dualistic nature of the panel structure with pure lattice structures: as the triangular mesh stabilizes lattice structures, three lines of support are necessary for panel structures to avoid the rigid mechanisms of a plate in a three-dimensional space. Although the trivalent vertex pattern is enough to prevent rigid mechanisms in closed plate structures, the echinoid tests are opened at the oral side, with the mouth (peristome), and the aboral side, with the anus (periproct). These two discontinuous areas, in particular the peristome, are remarkably large and not negligible; hence, the trivalent vertex principle is not sufficient to guarantee the stability of the overall shell structure. Different from the structures described by Wester, the joints between plates constituting the echinoid test have a curved geometry. Owing to the curvature of the intersection lines, relative rotation

between two adjacent plates is coupled with relative displacements between adjacent edges (F. Marmo et al., 2022).

In conclusion, the strategical partitioning of the test into plates and partially flexible sutures produce a reduction of bending actions, without compromising global stability. In fact, global mechanisms are avoided by the trivalent vertex arrangement, curved edges, and plate interlocking at the joint level. In contrast, the flexible sutures were identified as a functional biological principle to reduce bending actions. The flexible joints facilitate relative rotations between plates at small values of bending moments; knob-like protrusions can transmit in-plane and out-of-plane shear forces between modules; application of the trivalent vertex principle avoids global mechanisms (T. Wester, 1990); and (vi) curved modules avoid relative rotation between plates.

6. **Material differentiation**. Microscopically, SEM surveys on the *P. lividus* test showed high microstructural variation within the plates. The *stereom microstructure* is highly variable in density and architecture and is filled with cells and organic material (stroma). This architecture is extremely complex, largely varying not only from species to species, but also within the individual echinoid test plates. The microstructure is characterized by variable-oriented trabeculae of different basic types (e.g., imperforate, galleried, labyrinthic, fascicular, laminar) associated in very different combinations, creating species-specific 3D structural patterns (Smith, 1980). The differentiation depends on three main factors: associated soft tissues, mechanical needs, and growth rate (Smith, 1980). It optimizes the use of material, whereas structural specialization increases mechanical resistance, ensuring lightness and a high level of robustness (Grun and Nebelsick, 2018; Nichols and Currey, 1968).

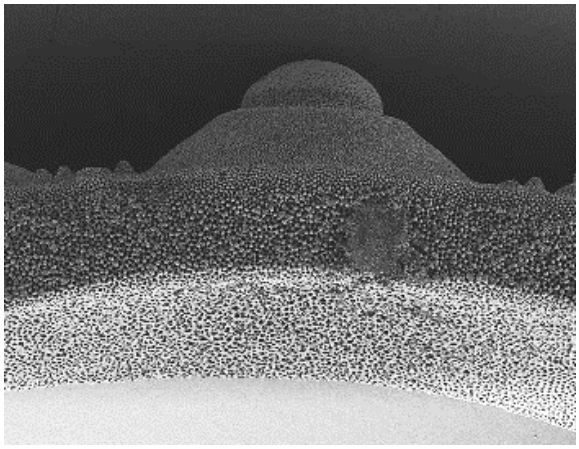

Figure 2.16. *Paracentrotus Lividus's* test: functional details from microscale. Material differentiation

Considering an interambulacral plate (figure 2.17a), the skeletal material tends to increase in density in different regions, such as tubercles and basal zone, and to specialize its microstructure in the zones more subjected to directional forces, i.e. the sutural ones (figure 2.17b). At the sutures, these external bands are characterized by a regular porous arrangement (galleried stereom) (AB. Smith, 1980), which is geometrically ordered and regularly oriented according to the junction direction (figure 2.17b, e). The suture area terminates with knob-like trabecular protrusions that allow interlocking between the adjacent plates (figure 2.17c, d,e). According to the description of Mancosu & Nebelsick (A. Mancosu, JH. Nebelsick, 2020], the sutural micromorphology among the different radial and circumferential regions is slightly variable; however, these differences can be considered negligible at the global scale. Moreover, plates are connected at sutures by short and strong articular ligaments, consisting of parallel bundles of densely packed collagen fibrils. In regular echinoids, these sutures remain 'open', up to the adult stage; thus, it is highly plausible that they actively influence the mechanical behaviour of the echinoid test as proved in the turtle carapace (S. Krauss et al., 2009).

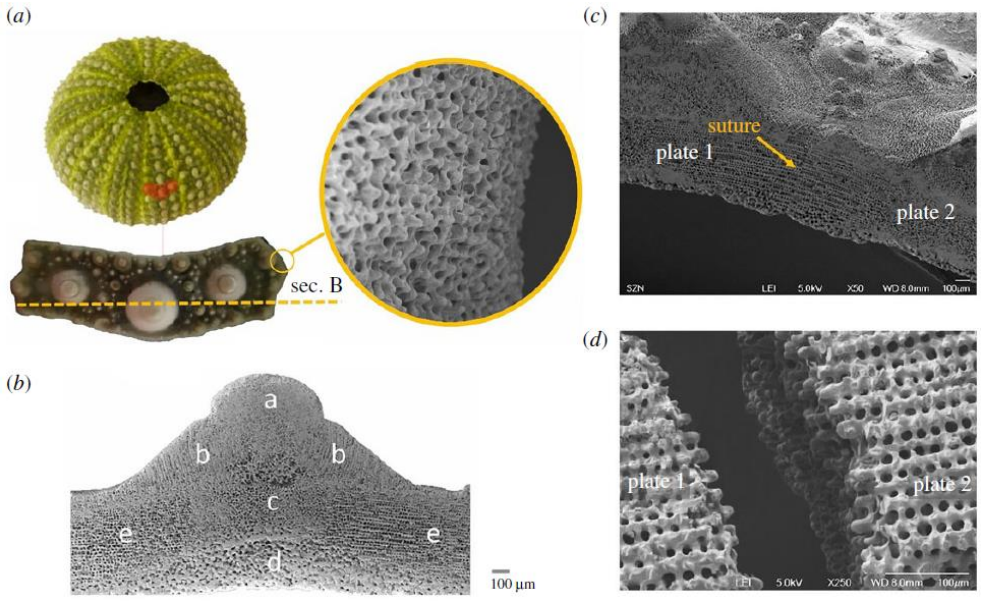

Figure 2.17. Macro and microstructure of an interambulacral plate. (a) Interambulacral plate with detail of knob-like protrusions, extracted from *Paracentrotus Lividus's* test. SEM micrographs showing: (b) plate transversal section with microstructural variability (a, imperforated; b, tubercle galleried; c, labyrinthic; d, perforated; e, suture galleried) identified by a dashed line; suture area of (c) joined and (d) divided plates (F. Marmo et al., 2022).

7. **Functional porosity**. Porosity is highly variable within the skeleton according to local functional needs. From a mechanical perspective, internal porosity ensures lightness and saves material without compromising the overall skeletal resistance (Grun and Nebelsick, 2018; Nichols and Currey, 1968), as well as reduces cracking eventuality (Vogel, 2013). Furthermore, open pores provide an attachment site for muscles and ligaments, as well as permeability and connections to the external environment. Examples of the latter function are the madreporite, a modified highly porous plate used to filter and balance the water vascular system, and gonophores, passageways for eggs and sperm release (Brusca and Brusca, 2003).

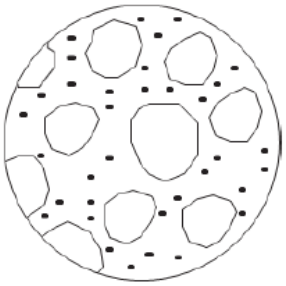

Figure 2.18. Porosity within the skeleton of echinoid test

8. **Ornamentation**. The plates are characterized by a series of species-specific tubercles and fine-relief ornaments. Tubercles serve as multiple articulation surfaces for spines (ball and socket joint) and pedicellariae allowing these appendages to exploit the wide range of movements related to their diverse functional roles (Smith, 1980). The plate surface ornamentation can indicate habitats and growth patterns of extant and fossil echinoids (Oldfield, 1976).

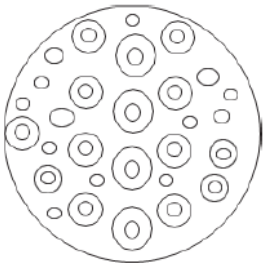

Figure 2.19. Ornaments

2.6 Nature-Inspired innovation from the echinoid test

Since all plates bear movable spines, their outer surfaces display the echinoid test's unique combination of strength, flexibility, efficient design, and adaptability providing numerous transferable properties that can inspire innovations in materials science, engineering,

architecture, robotics, environmental science, and beyond. By studying and applying these properties, we can develop new technologies and materials that are both efficient and sustainable. In industrial design, the functions analogous to those performed by the echinoid test are external protection, containment, and mechanical support.

The shape of the test and its interlocking plates protect the organism in harsh underwater environments. The functional characteristics of the test are particularly useful for the design of stable, resistant, flexible, and adaptable structures to be used in various industrial sectors from architecture to automotive, packaging, and biomedical. The echinoid test can inspire the creation of stronger, lightweight structures and buildings better able to withstand strong forces, like skyscrapers and wind turbines. Modularity has many benefits in the field of design, such as: reduction of production costs (repetitiveness of one or few modules and standardization); flexibility; free increase or reduction in scale (adding or removing modules); and versatility (new solutions for adding different modules). The trivalent vertexes are valid and easily reproducible elements in the designing (especially parametric) of stable and robust structures. Joints, with their shapes and structures, can instead be a source of inspiration for reversible and irreversible joints with a high degree of resistance and flexibility.

- Other bioinspired applications could be identified in:
- Optimized building constructions used as human protective shelters from variable external environmental conditions.
- Lightweight and resistant packaging, wrapping, or bottling of products securing from external damages during transportation and storage.
- Protective cases, such as electronic and digital device cases.
- Impact-resistant and multifunctional vehicle frames to which other components are attached.
- Protective equipment for working environments, sports activities, or motorcycle and bicycle safety, i.e., protecting accessories, e.g., clothing, and helmets.

Orthopedic devices such as back supports and braces: arm, foot, and ankle support, cervical collars, knee and elbow braces.

Chapter 3

The 2D analysis of the echinoid microarchitecture

In this chapter, is an in-depth characterization of the species-specific pattern present in the *Paracentrotus Lividus* interambulacral plates, including the analysis of the main microstructural features concerning their geometrical variability and mechanical responses. Accordingly, the plate stereom was analysed through: (1) skeletal analysis, describing the different stereom types as a network of segments (trabeculae) and nodes (conjunction points); (2) orientation analysis, estimating the local orientation of the trabecular system; (3) pore analysis, delineating the stereom pore space variability; (4) structural investigation using the Finite Element Method (FEM).

3.1 Materials and methods

3.1.1 Material preparation and image acquisition

Samples of *Paracentrotus Lividus* were collected in the Gulf of Naples, Italy. Five tests were selected (n1: diameter (d) 4.8, height (h) 2.5; n2: d 4.7, h 2.3; n3: d 4.5, h 2.5; n4 d 4.5 h 2.2; n.5 d 4.9 h 2.8) and completely digested via 0.1 N NaOH treatment (1 week), which completely removed the organic components and provided clean skeletons without altering their structure. The samples were then washed three times in deionized water to remove caustic remains and air-dried for several days. The interambulacral plates at the ambitus (i.e., the maximum horizontal circumference of the test that contains largest and most mature plates in echinoid ontogeny) were isolated, then longitudinally sectioned (Fig. 3.1). The cutting process was carried out manually, holding the plate to be cut in place, with the help

of tweezers, when necessary, on a Buehler Beta-Grinder-Polisher horizontal lapping machine, with Buehler Carbimet SiC fine-grained grinding discs, beginning with a P600 grain increasing to a P2,500 grain leading to the semi-polishing of the preparations. They were mounted on stubs, sputtered-coated with platinum and recorded using Scanning Electron Microscopy (SEM) (JEOL 6700F 250 MK2, at 5kV) at the Anton Dohrn Zoological Station of Naples, Italy.

3.1.2 Image processing

SEM micrographs (200x200 pixels) of the five longitudinally sectioned plates were analysed to acquire information regarding skeletal structure variability. The galleried stereom located at tubercle boss (gt) and sutures (gs), the labyrinthic stereom at the plate centre (l) and perforate stereom at the basal zone (p) were processed using Avizo software version 2019.1 (Thermo Fisher Scientific, Waltham, MA, USA) (Fig 3.1). The images were binarized using interactive thresholding in order to identify and divide the skeletal region from the background (pore area). The binarized images were used for the skeletal, orientation and pore analysis of the different microstructures (Fig. 3.2).

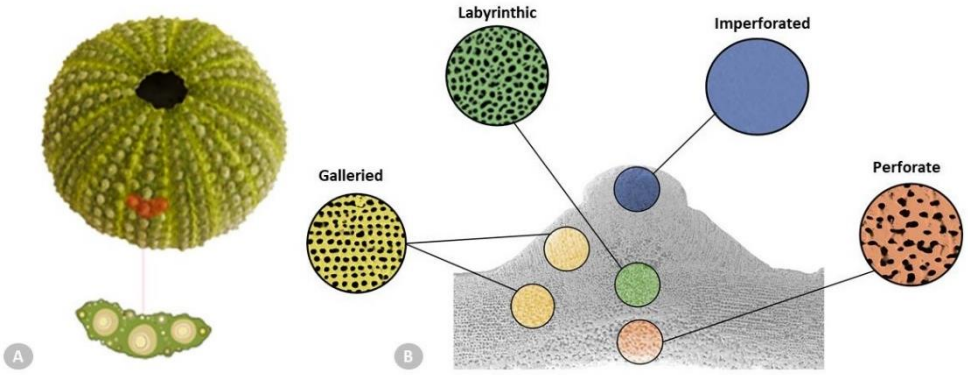

Figure 3.1. A) *Paracentrotus Lividus's* test and interambulacral plate. B) Longitudinal section of the interambulacral plate analysed showing stereom variability and highlighting the galleried stereom located at the tubercle boss and suture area, labyrinthic stereom located at the plate center and perforated stereom at the basal

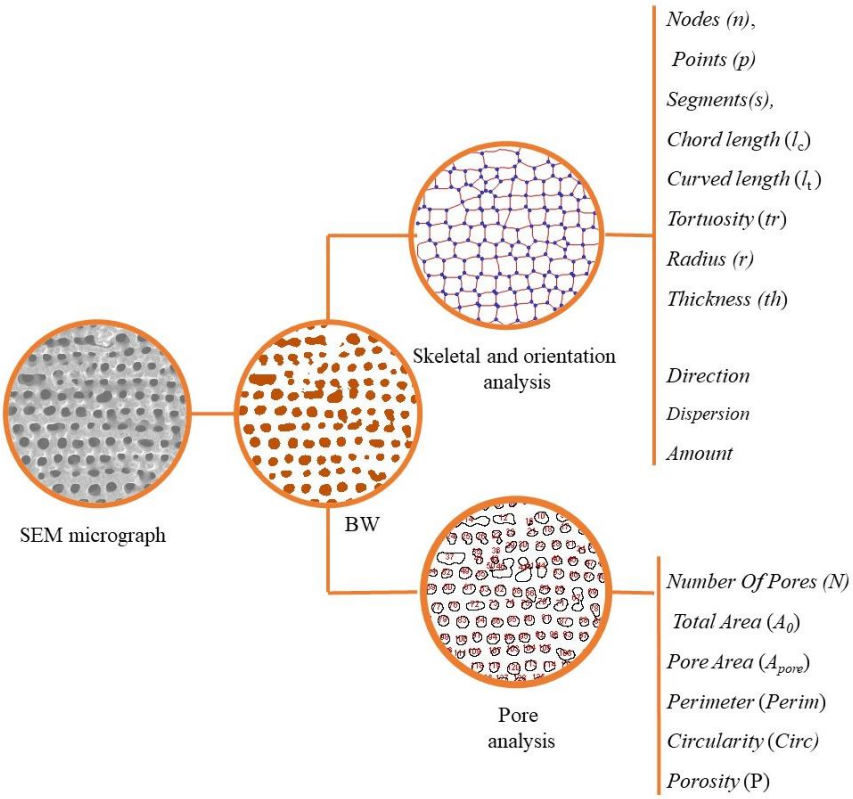

Figure 3.2. *Image processing*. SEM micrographs (200x200 pixels) of the longitudinally sectioned plates were binarized using interactive thresholding in order to identify and divide the skeletal region from pore area. The binarized images were used for the skeleton, orientation and pore analysis of the different microstructure.

3.1.3 Skeletal analysis

The different skeletal regions were analysed using the Avizo "auto-skeleton" command, which transforms the trabecular stereom system into segments, i.e., lines equidistant to the shape boundaries providing region-based shape features of each trabecula, and nodes, representing the junctions of these segments. In addition, several points provide the description of the segment course.

Accordingly, the following information was obtained: (1) *Nodes* (n), number of intersection points; (2) *Points* (p), number of descriptors of the segment course; (3) *Segments*(s), number of identified trabeculae;

(4) *Chord length* (lc) described by a straight line between two nodes; (5) *Curved length* (lt) identified as the approximated curved course of a segment; (6) *Tortuosity* (tr) defined by the ratio between curved length and chord length *t= lt / lc*; (7) *Radius* (r) explained as the mean value of all point radii describing a segment.

In addition, thickness (th) was measured using the BoneJ thickness Fiji/ImageJ plug-in that calculated the thickness value in a specific point as the diameter of the largest sphere fitting within the structure and containing the point. The plugin calculates mean and standard deviation of the trabecular thickness directly from the pixel values of the thickness map

3.1.4 Orientation analysis

To estimate the local orientation of the trabecular system, the Directionality Fiji/ImageJ plug-in was applied on binarized images. This algorithm is based on Fourier spectrum analysis, which splits the image into square pieces and computes their Fourier power spectra, analyzed in polar coordinates, measuring the power for each angle. This method generates normalized histograms revealing the number of trabeculae present between -90°, +90° and uses a correspondent gaussian to compute the directionality parameters. Directional data are therefore reported: Direction (º), the gaussian center; Dispersion (º), the gaussian standard deviation; Amount, the histogram sum from center-std to center+std, divided by the total sum of the histogram; Goodness, indicating good (=1) or bad (=0) fitting.

3.1.5 Pore analysis

The pore spaces were analysed using binarized images of the different skeletal microstructures by means of the “Analyze particles” command in Fiji. This provides information regarding: (1) Number (n) of identified pores; (2) Total Area (A0) of the selection in calibrated square units (µm2); (3) Pore Area (Apore) of the selection in calibrated square units (µm2); (4) Perimeter (Perim), the length of the boundary of the selection calculated by its decomposition into individual

selections; (5) Circularity (Circ), shape descriptor calculated using equation (3.1).

$$Circ = 4\pi \times \left[\frac{A_{pore}}{Perim^{2}}\right] \quad (3.1)$$

for which a value of 1 indicates a perfect circle and values decreasing toward 0 indicate increasingly elongated shapes; (6) Porosity (P), amount of pore area in the skeleton compared to the skeletal area investigated in toto using equation (3.2).

$$P = \left(\frac{A_{pore}}{A_0}\right) * 100\% \quad (3.2)$$

3.1.6 Statistical analysis

Statistical analyses were carried out using PAST software for Windows, version 3.16 (Hammer et al., 2001). In particular, non-parametric univariate analysis Kruskal-Wallis tests were carried out to determine the specific differences between the different stereom structures. Correlation analyses were carried out to measure the linear relationship strength between variables using Pearson's r linear correlation statistics. Two-sample Wilcoxon Mann-Whitney test was carried out to determine statistical differences in the skeletal structure between the galleried stereom at suture and the one located at the tubercle. The differences among the stereom types were visualised using a non-metric multidimensional scaling ordination (nMDS) for both skeletal and pore analysis

3.1.7 Structural investigation

The Finite Element Method (FEM) was used to evaluate the mechanical response of each stereom type and evaluate the corresponding elastic parameters of a homogenised material. To this end, binarized images were used to obtain the geometry of each specimen. Each geometry was vectorized and imported in Abaqus/CAE 2022 and cleaned-up to obtain a connected manifold. Successively, it was discretized into quadrilateral elements with CPS4R formulation, i.e., continuum element in plane stress with 4

nodes and reduced integration. The material constitution associated to such models is linear elastic, with elastic modulus E=73.5 GPa and Poisson ratio v=0.4, corresponding to solid organic calcite (Chen, 2011). An arbitrary thickness of 0.001mm was assigned to such plane models.

Three analyses were conducted on the finite element model of each stereom type by assigning a uniform distribution of one strain component $\varepsilon_i = 0.00211$, i=1,2,3, keeping the others equal to zero. Here the Voight notation is used, hence ε_1 and ε_2 are linear strains, while ε_3 is the shear strain. Corresponding boundary conditions assigned to perform these analyses are shown in Figure 3.3 on the suture galleried stereom model.

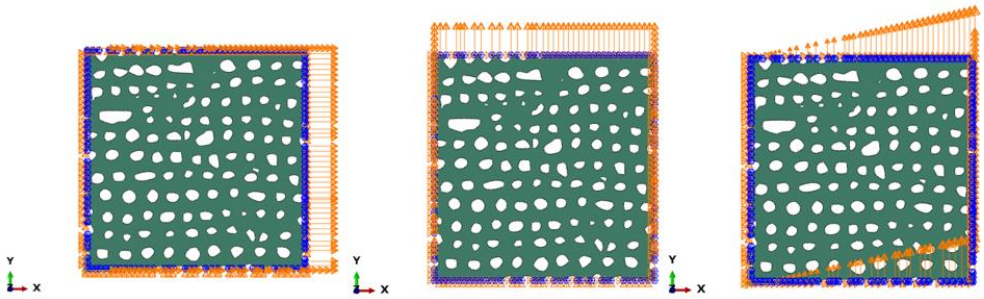

Figure 3.3. Boundary conditions assigned to perform the stress analyses of stereoms: A) uniform normal strain along x, B) uniform normal strain along y, and C) uniform shear strain.

The results of the generic i-th analysis, were used to compute the components of the homogenised stiffness tensor associated to the corresponding stereom as $C_{ji} = \bar{\sigma}_j/\varepsilon_i$ where $j = 1,2,3$ and $\bar{\sigma}_j = \int_S \sigma_j dS / \int_S dS$ is the average value of the stress component σ_j computed on the entire area S of the stereom.

Homogenised stereom types were expected to be anisotropic. Hence, it is possible to identify the direction of higher stiffness, represented by a rotation angle $\theta_{\max}$, along which C_{11} is maximised (notice that C_{22} is maximum along the orthogonal direction $\theta_{max} \pm \pi/2$). Such direction can be computed by maximising the C_{r11} component of the rotated stiffness tensor $\mathbf{C_r} = \mathbf{RCR}^{\mathrm{T}}$, where $\mathbf{R}$ is the rotation matrix (Vannucci, 2018).

$$\mathbf{R} = \begin{bmatrix} cos^2\,\theta & sin^2\,\theta & 2\,sin\,\theta\,cos\,\theta \\ sin^2\,\theta & cos^2\,\theta & -2\,sin\,\theta\,cos\,\theta \\ -\,sin\,\theta\,cos\,\theta & sin\theta\,cos\theta & cos^2\,\theta - sin^2\,\theta \end{bmatrix} \quad (3.3)$$

3.2 Results

3.2.1 Skeletal, orientation and pore analysis

Imperforate stereom

The imperforate stereom (Fig. 3.11$_i$) is a solid calcite layer lacking stroma canals and characterises the mamelon zone.

Sutural galleried stereom

The galleried stereom (Fig. 3. 11$_{gs}$) characterises the most external bands at the suture area. This stereom is uniform in thickness and length, showing little tortuosity (Tab.3.1) (Fig. 3.4). The trabeculae are predominantly oriented at 0.2±3.5° with a small dispersion indicative of a uniform alignment (Tab. 3.2) (Fig. 3.5). The porosity is 21.25±2.01 consisting of parallelly organized pores that are regular in form as shown by the highest level of circularity (Fig. 3.6).

Tubercle galleried stereom

This galleried stereom (Fig. 3. 11$_{gt}$) constitutes the tubercle boss and is characterised by numerous aligned trabeculae uniform in length and showing little tortuosity (Tab. 3.1) (Fig. 3.4). The trabeculae are predominantly oriented at 82.0±3.5° with a uniform alignment (Tab. 3.2) (Fig. 3.5). The porosity is 25.52±4.7 consisting in numerous pores that are parallel and regular in form as shown by the circularity (Fig. 3.6).

Labyrinthic stereom

The labyrinthic stereom (Fig. 3. 11_I) characterises the inner central part of the plate, extending into the boss centre, where it forms a very coarse and open structure (Fig. 3.12_E). The labyrinthic stereom consists of a uniformly short and thick system of trabeculae (Tab. 3.1) (Fig. 3.4). Results confirmed the non-orientation of the trabecular system as indicated by the variability of orientation peaks, the high dispersion from the gaussian and its poor fitting (Tab. 3.2) (Fig. 3.5). The porosity is 25.69±2.7 with regularly shaped pores (Tab. 3.3) (Fig. 3.6).

Perforate stereom

The perforate stereom (Fig. 3.11_p) is a remarkably high-density layer and characterizes the basal plate zone and is also present at the base of the tubercle boss (Fig 3.11). The trabecular system is characterized by few and thick trabeculae (Tab. 3.1) (Fig. 3.4). The variability in the main direction and the high dispersion from the gaussian indicate an unclear dominant direction (Tab. 3.2) (Fig. 3.5). However, a slight horizontal orientation is visible in the SEM micrographs. The porosity is 19.04±6.4 with a small number of regularly shaped pores (Tab. 3.3) (Fig. 3.6).

Stereom comparison

The Kruskal-Wallis tests indicated differences among the investigated stereom types at a significant level of $\alpha = 5\%$. Regarding the skeletal analysis, nodes, points, segments, curved length, chord length, radius, tortuosity and thickness were statistically different among the four stereom types (Tab. 3.1). Regarding the pore analysis, number of pores, pore area, perimeter, and circularity were statistically different among the analysed stereom types; whereas the total area and porosity were not significant (Tab. 3.3).

Correlation analyses revealed a strong linear correlation between nodes and segments (0.999), points and nodes (0.891), points and

segments (0.886), chord length and curved length (0.999), radius and curved length (0.968), radius and chord length (0.967) (Tab. 3.4).

The spatial differences among the stereom types for the skeleton data were also evidenced by the nMDS plot (Fig. 3.7), which showed a clear separation between the four types, while suture galleried partially overlapped with labyrinthic stereom. Whereas the nMDS plot (Fig. 3.8) revealed the spatial differences among the stereom types regarding the pore data, showing a clear separation between the four types and a partial overlap of the labyrinthic stereom with suture and tubercle galleried stereoms.

Two-sample Wilcoxon Mann-Whitney test between the galleried stereom at suture and the galleried located at the tubercle reported that: nodes, segments, curved length, chord length, radius, tortuosity, thickness, number of pores, pore area, and circularity were significant, whereas points, perimeter, total area, and porosity were not significant (Tab. 3.5).

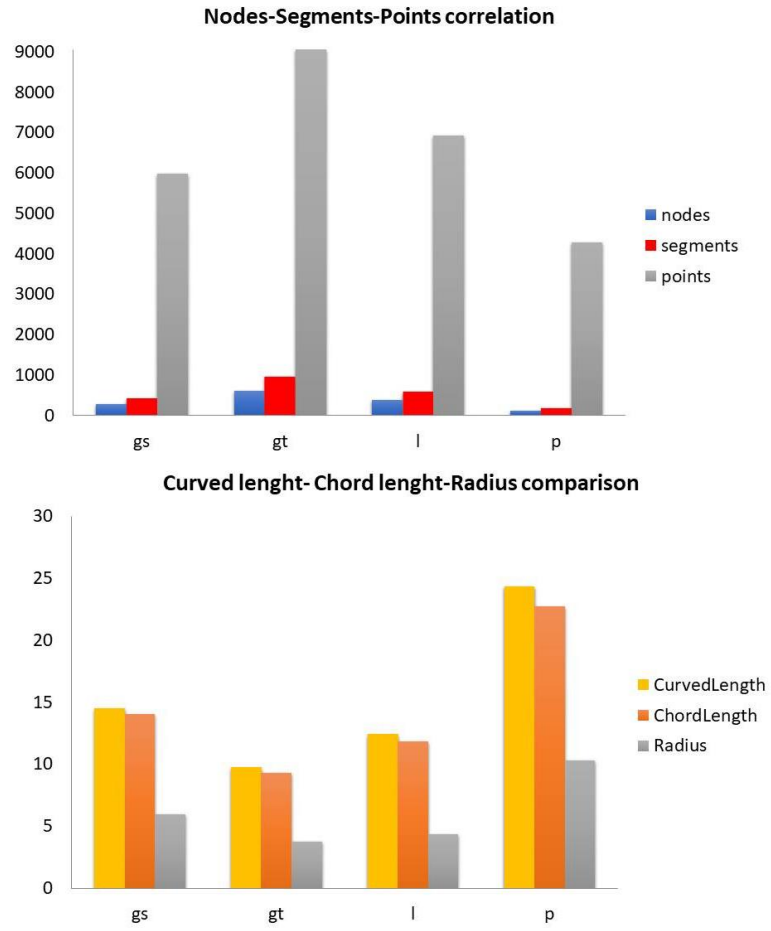

Figure 3.4. Histograms of node-segment-point comparison and curved length-chord length-radius comparison. gs= galleried stereom at suture; gt= galleried stereom at tubercle; l=labyrinthic stereom; p=perforate stereom

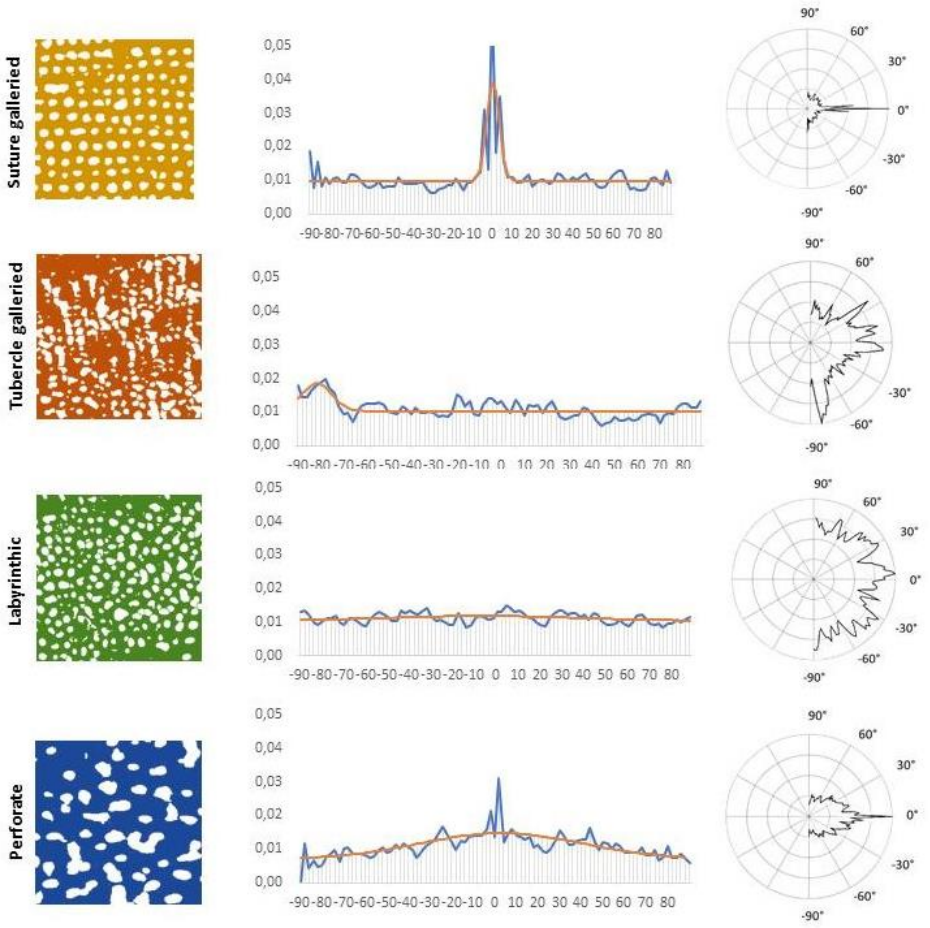

Figure 3.5. Histograms and polar plots of the trabecular orientation results regarding the suture galleried, tubercle galleried, labyrinthic and perforate stereom.

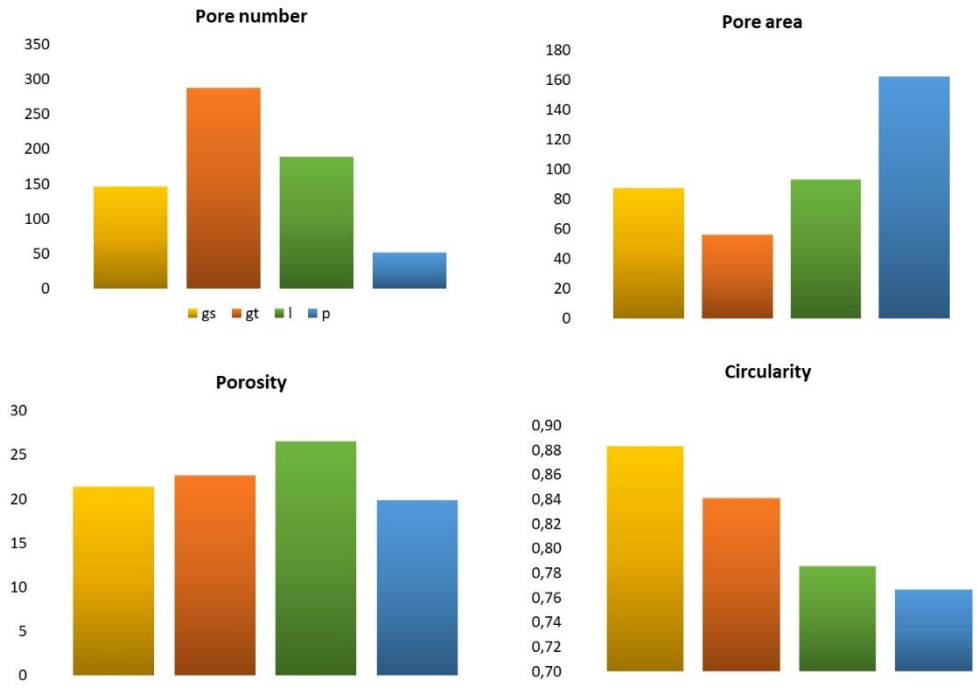

Figure 3.6. Histograms of pore number, pore area, porosity, and circularity. gs= galleried stereom at suture; gt= galleried stereom at tubercle; l=labyrinthic stereom; p=perforate stereom.

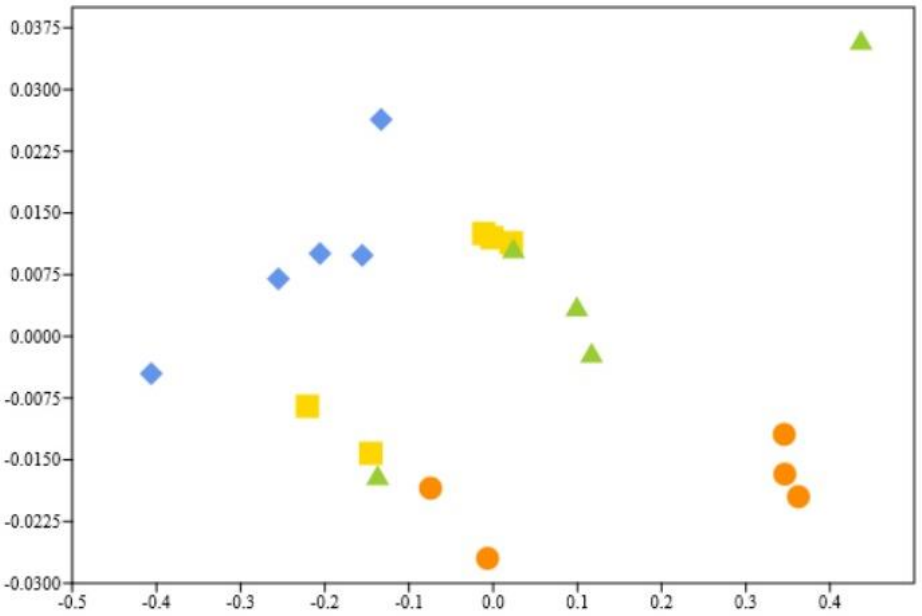

Figure 3.7. Non-metric multidimensional scaling (nMDS) ordination based on Euclidean similarity index considering the skeleton analysis data.

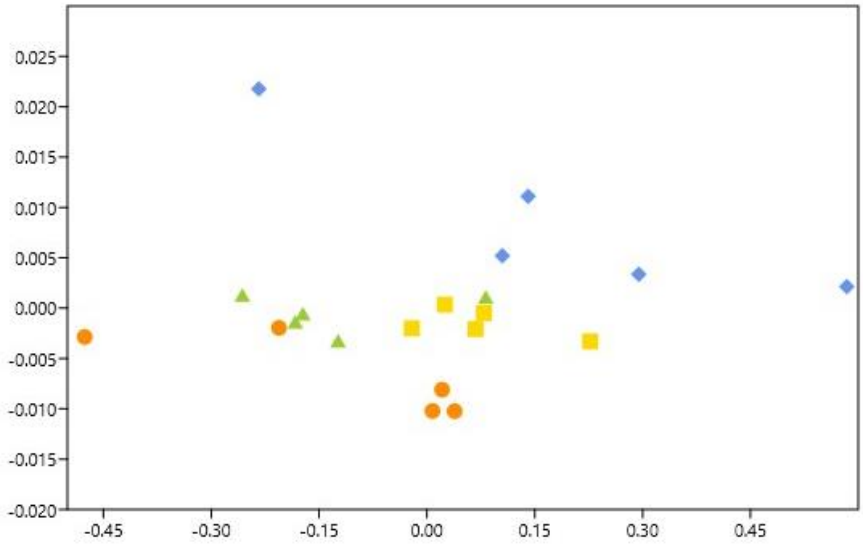

Figure 3.8. Non-metric multidimensional scaling (nMDS) ordination based on Euclidean similarity index considering the pore analysis data.

Table 3.1. Summary of the trabecular analysis and Kruskal-Wallis test results.

Suture galleried	**N**	**Tubercle galleried**	**N**	**Labyrinthic**	**N**	**Perforate**	N	Kruskal-Wallis tests			
								H (chi^2)	Hc	p	n
265.20 ± 30.3	-	542.00 ±134.00	-	367.60 ±68.94	-	122.00 ±39.3	-	16.58	16.58	<0.001	6484
5433.20 ±942.1	-	7735.20 ±1895.9	-	7007.80 ±1855,9	-	4045.00 ±962.9	-	10.93	10.94	0.001	121106
399.40 ±48.0	-	841.40±207.2	-	563.40 ±104.56	-	179.20 ± 57.09	-	16.58	16.58	<0.001	9917
14.89 ±1.0	1997	10.57 ±1.7	4207	12.71 ±1.4	2817	23.94 ±5.70	896	16.07	16.07	<0.001	9917
14.30 ±6.47	1997	10.08 ±1.6	4207	12.16 ±1.4	2817	22.46 ±5.2	896	16.07	16.07	<0.001	9917
5.88 ±0,51	1997	3.75 ±0.6	4207	4.70 ±0.9	2817	11.51 ±3.48	896	16.01	16.01	<0.001	9917
1.03 ±0.0	1997	1.04 ±0.0	4207	1.04 ±0.0	2817	1.05 ±0.0	896	12.41	12.46	0.002	9917
19 ±1.9	-	15 ±2.9	-	18.29 ±5.0	-	39.52 ±13.8	-	12.39	12.39	<0.001	9917

Table 3.2. Summary of the orientation analysis results

	Suture galleried	Tubercle galleried	Labyrinthic	Perforate
-90	0.055±0.0	0.068±0.0	0.057±0.0	0.046±0.0
-80	0.048±0.0	0.083±0.0	0.055±0.0	0.047±0.0
-70	0.052±0.0	0.051±0.0	0.053±0.0	0.051±0.0
-60	0.051±0.0	0.046±0.0	0.051±0.0	0.055±0.0
-50	0.051±0.0	0.046±0.0	0.052±0.0	0.059±0.0
-40	0.049±0.0	0.046±0.0	0.055±0.0	0.062±0.0
-30	0.046±0.0	0.050±0.0	0.061±0.0	0.060±0.0
-20	0.052±0.0	0.056±0.0	0.054±0.0	0.062±0.0
-10	0.073±0.0	0.082±0.0	0.059±0.0	0.070±0.0
10	0.121±0.0	0.084±0.0	0.081±0.0	0.093±0.0
20	0.050±0.0	0.070±0.0	0.054±0.0	0.061±0.0
30	0.049±0.0	0.054±0.0	0.057±0.0	0.055±0.0
40	0.052±0.0	0.069±0.0	0.057±0.0	0.054±0.0
50	0.054±0.0	0.039±0.0	0.050±0.0	0.053±0.0
60	0.053±0.0	0.044±0.0	0.051±0.0	0.049±0.0
70	0.050±0.0	0.034±0.0	0.053±0.0	0.045±0.0
80	0.052±0.0	0.043±0.0	0.054±0.0	0.044±0.0
90	0.041±0.0	0.035±0.0	0.046±0.0	0.034±0.0
Direction (°)	0.262±3.5	-82.000±6.5	-36.664±49.0	-8.040±30.5
Dispersion (°)	4.744±2.0	14.010±6.0	20.612±16.0	24.528±13.2
Amount	0.186±0.0	0.010±0.1	0.432±0.4	0.606±0.3
Goodness	0.650±0.2	0.220±0.2	0.226±0.2	0.584±0.2

Table 3.3. Summary of the pore analysis and Kruskal-Wallis test results.

Suture galleried	**N**	**Tubercle galleried**	**N**	**Labyrinthic**	**N**	**Perforate**	N	Kruskal-Wallis tests			
								H (chi^2)	Hc	p	N
153.60±16.7	768	274.6 ±36.2	1373	182.60 ±36.7	913	59.60 ±17.4	298	16,38	16.38	<0.001	3352
92.07 ±9.9	768	62.77 ±16.1	1373	95.31 ±14.4	913	221.78 ±95.7	298	15.27	15.27	0.001	3352
34.27 ±2.4	768	29.07 ±4.5	1373	36.81 ±4.1	913	57.46 ±15.6	298	13.78	13.79	0.003	3352
0.88 ±0.0	768	0.8 3±0.0	1373	0.82 ±0.0	913	0.77 ±0.0	298	11.02	11.19	0.011	3352
14066.39 ± 1331.4	768	16891.41 ±3146.4	1373	17006.15±1821.8	913	12607.33± 4239.6	298	6.95	6.95	0.07	3352
34.27±2.4	768	25.52±4.7	1373	25.69±2.7	913	19.05±6.4	298	6.95	6.95	0.07	3352

Table 3.4. Correlation matrix of the Pearson's r statistics reporting the correlation coefficients (highlighted in bold) and the p-value of the correlations

	Nodes	**Segments**	**Points**	**Curved length**	**Chord length**	**Radius**	**Tortuosity**	**Thickness**
Nodes		3.0208E-31	1.416E-07	2.5262E-06	1.6302E-06	2.9108E-05	0.52267	0.00024907
Segments	**0.99975**		1.9755E-07	3.1818E-06	2.0643E-06	3.5669E-05	0.5246	0.00031878
Points	**0.89068**	**0.88635**		3.87E-05	3.224E-05	0.0003719	0.42794	0.00044625
Curved length	**-0.84659**	**-0.84232**	**-0.7868**		2.7173E-31	2.8778E-12	0.1244	1.1475E-09
Chord length	**-0.85436**	**-0.85022**	**-0.79151**	**0.99976**		3.3898E-12	0.142	1.4403E-09
Radius	**-0.7941**	**-0.78892**	**-0.71722**	**0.96812**	**0.96753**		0.24315	2.1182E-13
Tortuosity	**-0-15188**	**-0.15119**	**-0.18776**	**0.35514**	**0.34036**	**0.27358**		0.24962
Thickness	**-0.73125**	**-0.72271**	**-0.71056**	**0.9372**	**0.93555**	**0.97622**	**0.27**	

Table 3.5. Summary of the Two-sample Wilcoxon Mann-Whitney test results between the galleried stereom at suture and the galleried located at the tubercle.

Two-sample Wilcoxon Mann-Whitney tests	Nodes	Points	Segments	Curved length	Chord length	Radius	Tortuosity	Thickness	Pore number	Pore Area	Perimeter	Circularity	Total area	Porosity
z	-2.51	-1.26	-2.51	-2.51	-2.51	-2.51	-2.42	-2.09	-2.51	-2.29	-1.67	-2.13	-1.67	-1.67
p	0.012	0.208	0.012	0.012	0.012	0.012	0.016	0.036	0.012	0.021	0.094	0.035	0.094	0.095

3.2.2 Structural analysis

Figures 3.9 and 3.10 report the results of finite element analyses conducted on each stereom. The components of computed homogenised stiffness tensors are reported in Table 3.6. These values clearly show that all stereoms are anisotropic except the labyrinthic, which can be considered isotropic. To better represent the anisotropic nature of stereoms, the components of $\mathbf{C_r}$ are plotted in polar coordinates as a function of θ. These plots are reported in Figure 3.9, where the dashed line represents the direction of higher stiffness. To be noted that in this figure only the component C_{r22} is not diagrammed since $C_{r22}(\theta) = C_{r11}(\theta - \pi/2)$.

The components of the stiffness tensor along the direction of higher stiffness are reported in Table 3.7. These values show that the anisotropy of the perforate and both galleried stereoms is more pronounced with respect to labyrinthic stereom. Anisotropy is related to higher values of the ratio C_{r11}/C_{r22}. As shown by the low values of $C_{r13} = C_{r31}$ and $C_{r23} = C_{r32}$, all stereoms, exhibit poor coupling between shear and longitudinal behaviours when solicited in reference of higher stiffness. Hence, all stereoms can be considered, with a good approximation, as orthotropic materials. Notably, however, the tubercle galleried stereom exhibits higher coupling between shear and the direction of lower longitudinal stiffness (higher value of the stiffness tensor component $C_{r23} = C_{r32}$).

The contour plot of figure 3.10 shows how the microstructure geometry influences the stress distribution within each stereom. As expected, higher stress values tend to concentrate between pores. The flow of stresses is clearly visible in the regions where the alignment of pores allows a continuous transmission of internal forces, forming stress concentration bands. Longitudinal and transversal bands are clearly visible in all stereoms, while diagonal bands are evident especially in the labyrinthic stereom. Noticeably, the very regular geometry of the suture galleried stereoms tailors a direct transmission of stresses along all directions. The transversal misalignment of pores in the tubercle galleried stereom, instead, inhibit the formation of stress bands in this direction

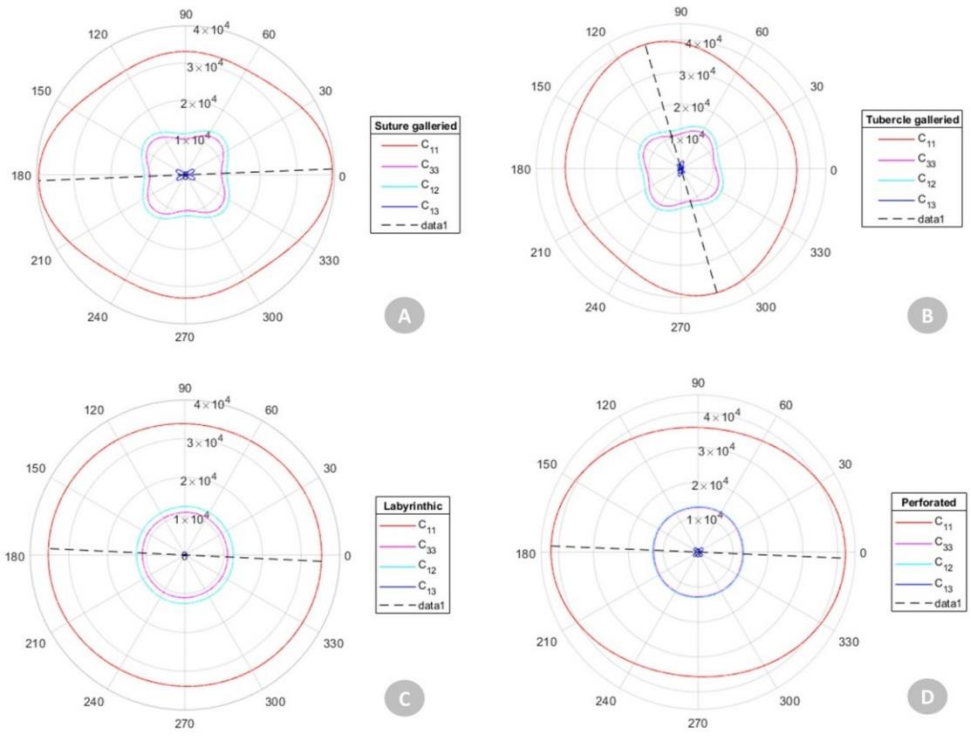

Figure 3.9. ELAST Polar plot of stiffness tensor components as a function of the rotation angle θ. Dashed line represents the direction θ_max of higher stiffness. A) Suture galleried, B) Tubercle Galleried, C) Labyrinthic, D) Perforate

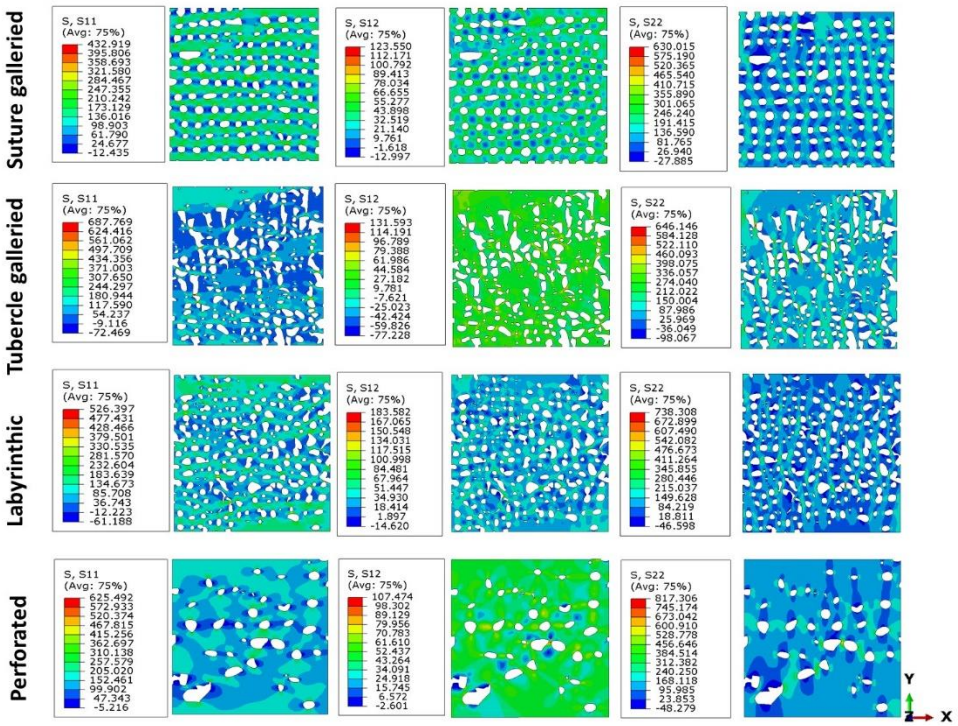

Figure 3.10. Contour plots of stress values computed via finite element analyses for the different stereom types. Left column: stereoms subjected to uniform strain in the horizontal direction; central column: stereoms subjected to uniform shear strain; right column: stereoms subjected to uniform strain in the vertical direction; S11 = normal stress along the horizontal direction; S12 = shear stress; S22 = normal stress along the vertical direction

Table 3.6. ELAST Stiffness tensor components in MPa of a homogeneous linearly elastic material mechanically equivalent to stereom.

Stiffness tensor component	**Suture galleried**	**Tubercle galleried**	**Labyrinthic**	**Perforate**
C_{11}	39411	35961	35294	42167
C_{22}	33089	39014	33877	35664
C_{33}	9607	10814	11003	12763

$C_{12} = C_{21}$	11024	12305	12499	13004
$C_{13} = C_{31}$	368	-111	-36	-151
$C_{23} = C_{32}$	-22	-1858	-165	-268

Table 3.7. ELAST CR Stiffness tensor components in MPa of a homogeneous linearly elastic material mechanically equivalent to stereoms, oriented according to the direction of higher stiffness, which is identified by the angle $\boldsymbol{\theta_{max}}$.

Stiffness tensor component	**Suture galleried**	**Tubercle galleried**	**Labyrinthic**	**Perforate**
θ_{max}	2.286°	-73.872°	-2.664°	-2.376°
C_{r11}	39440	40112	35297	42180
C_{r22}	33083	35428	33849	35629
C_{r33}	9595	10532	11015	12774
$C_{r12} = C_{r21}$	11012	12023	12511	13015
$C_{r13} = C_{r31}$	0	-1	0	0
$C_{r23} = C_{r32}$	93	-851	-134	148

3.3 Discussion

The results achieved in the present study described the microstructural variation in the *Paracentrotus lividus* interambulacral plates. According to the descriptions provided by Smith (1980), different structural bands are recognizable within each plate corresponding to a clear sequence of a distinct structural pattern (Fig. 3.11). Nonetheless, the results quantitatively highlighted important differences among the different types of stereom, providing novel insights on their geometrical configuration and mechanical behaviour.

Imperforate stereom

The imperforate stereom (Fig. 3.11$_{i}$) is a solid calcite layer present at the mamelon zone, which is exposed to the maximum high frictional and compressive stresses of the spine action.

Sutural galleried stereom

This galleried stereom (Fig. 3.11$_{gs}$) characterizes the suture area and ends with knob-like protrusions, allowing interlocking between complementary plates (Fig. 3.12A-B). In living organisms, this galleried stereom offers an attachment site for short sutural collagen fibres connecting adjacent plates (see Mancosu and Nebelsick, 2020), as well as, representing a directional load transfer in the trabecular system, disseminating applied stress directionally onto the adjacent ones, decreasing the chance of a structural local failure (Silva and Gibson, 1997). FE-Analysis reported a prevalent direction of higher stiffness at 2.286°. The low value of the ratio between C_{11} and C_{22} confirms the anisotropic behaviour and specialization to withstand stresses along the horizontal direction.

Tubercle galleried stereom

This galleried stereom (Fig. 3.11$_{gt}$) constitutes the tubercle boss and is characterised by aligned trabeculae, which are recently discovered to be arranged as a Voronoi construction with a prevalence of

hexagonal polygons, and a regularly organized seed distribution (Perricone et al., 2022). However, this stereom is different from the one located at the suture for number of nodes, segments, curved length, chord length, radius, thickness, number of pores and pore area as reported by Two-sample Wilcoxon Mann-Whitney test results. Interestingly, the tests also reported that pore perimeter was not significant. This paradox could be explained by considering the pores of the suture and tubercle galleried stereoms as isoperimetric, i.e., figures with same perimeters but different areas. The thickness distribution is vastly different between the two galleried stereoms as highlighted by the thickness map (Fig. 3.13). Indeed, the tubercle stereom shows a higher number of short and thin trabeculae, with smaller but more numerous pores as well as different concentric banding representing the stereom growth zones (Fig. 3.12). The tubercle galleried stereom displays an inclined main orientation at -82° with a moderate dispersion due to significative amounts of differently oriented trabeculae, particularly at ~0° (Wainwright et al., 1976, Vogel, 2013; Currey, 1999; Grun and Nebelsick, 2018; Nichols and Currey, 1968; Oaki and Imai, 2006; Müter et al., 2015). In living organisms, this stereom offers an attachment site for the catch apparatus fibres connecting the spine to the tubercle (Takahashi K. 1967; Hidaka and Takahashi, 1983; De Castillo et al., 1995). Similarly to the suture galleried stereom, this trabecular system can disseminate directionally applied stress; however, the growth bandings could presumably influence the mechanical response of the tubercle as shown in the spines (Grossmann and Nebelsick, 2013; Nickel et al. 2018; Presser et al. 2009; 2011); hence, further investigations are necessary. FE-Analysis reported the direction of higher stiffness at -73.872°. Similarly to the suture galleried stereom, the low value of the C_{11}- C_{22} ratio confirms an anisotropic behaviour and specialization to withstand inclined directional stresses.

Labyrinthic stereom

The labyrinthic stereom (Fig. 3.11$_l$) consists of a uniformly short and thick system of trabeculae with pores comparable to the suture galleried, but smaller, more numerous and less regular. FE-Analysis reported the direction of higher stiffness at -2.664°. However, the high value of the C_{11}- C_{22} ratio leads to a mechanical behaviour that is

approximately isotropic and a lower specialization to preferably work in one direction.

Perforate stereom

This stereom (Fig. 3.11$_p$) is a remarkably high-density layer and its trabecular system is thicker compared to the other analysed stereom types. Compared to the other analysed stereom types, pores are less numerous and regular in shape, but larger. FE-Analysis reported the direction of higher stiffness at -2.376°. This stereom is characterized by higher value of the C_{11}- C_{22} ratio that determines a low anisotropic behaviour and lower specialization of this stereom to primarily work in one direction. However, in figure 3.9 a slight preferential horizontal direction of the higher stiffness is visible.

Stereom comparison

The statistical analysis carried out for the comparison of the different stereom types revealed that all the investigated stereoms are significantly different (Fig. 3.13). Interestingly, the tubercle galleried is diametrically opposite to the perforate stereom in terms of skeletal geometric organization (Fig. 3.11). Indeed, the tubercle galleried is characterised by more trabeculae (segments and points) and connection points (nodes), which are shorter, less thick and tortuous, whereas the perforate stereom has less trabeculae and connection points that are however longer, thicker and more tortuous (Fig. 3.11).

The pore analysis revealed that although the microstructure architectures are significantly different, the porosity is homogeneous. Hence, lightness is ensured even in perforate stereom, which is characterized by large pores. As shown by the comparison of different stereom data, the porosity distribution and trabecular orientation are determining factors for the different isotropic and anisotropic mechanical behaviours. The possible architectural modulations in relation to specific mechanical needs have been hypothesized and described in several studies regarding echinoid plates and other skeletal elements (Raup, 1966; Nissen, 1969; Jensen, 1972; Regis, 1977; Smith, 1980; Telford, 1985 Muter et al, 2015; Grun and

Nebelsick, 2018; Grun et al., 2018). Accordingly, the structural pattern could be correlated to the specified mechanical needs of the skeletal areas. In the area subjected to high compressive stress, as in the mamelon zone, the skeletal material increases in density specializing in an imperforate stereom, whereas it specializes in the anisotropic galleried stereom within the margins following the directional stresses originating from sutural collagen fibres connecting adjacent plates. Another anisotropic galleried stereom is present at the tubercle boss that accommodates the stresses produced from the movable spines (Ji et al., 2022). The plate centre could be subjected to multiple directional tensions that are confronted by a uniformly long and thick non-oriented trabeculae of the isotropic labyrinthic stereom. Finally, a perforate stereom is employed in the basal area, indicating that this area is subjected to high tensional states (presumably generated from spine actions). This specialization is confirmed by the results of the structural analysis, which highlighted the highly anisotropic behaviour of both galleried stereoms. The perforate stereom exhibited a lower anisotropic response while the labyrinthic can be considered isotropic with acceptable approximation. From the comparison between the magnitudes of maximum longitudinal stiffnesses C_{r11}, it is clear that the labyrinthic stereom is visibly less stiff than the others. This is due to the presumably lower values of stress to which the central portion of the plate is subjected. This observation is confirmed by the presence of a very coarse and open structure close to the boss centre. On the other hand, the stiffer stereom resulted to be the perforate one, which, being positioned in the lower portion of the plate, is probably subjected to tensile stresses when a compressive force is applied to the mamelon zone. Noticeably, all stereoms have similar values of the minimum longitudinal stiffness C_{r22}. However, it is necessary to point out that these values of stiffness have been computed on 2D models of the stereoms, assuming an arbitrary thickness in the transversal direction. Future analyses on 3D models are needed to confirm described trends.

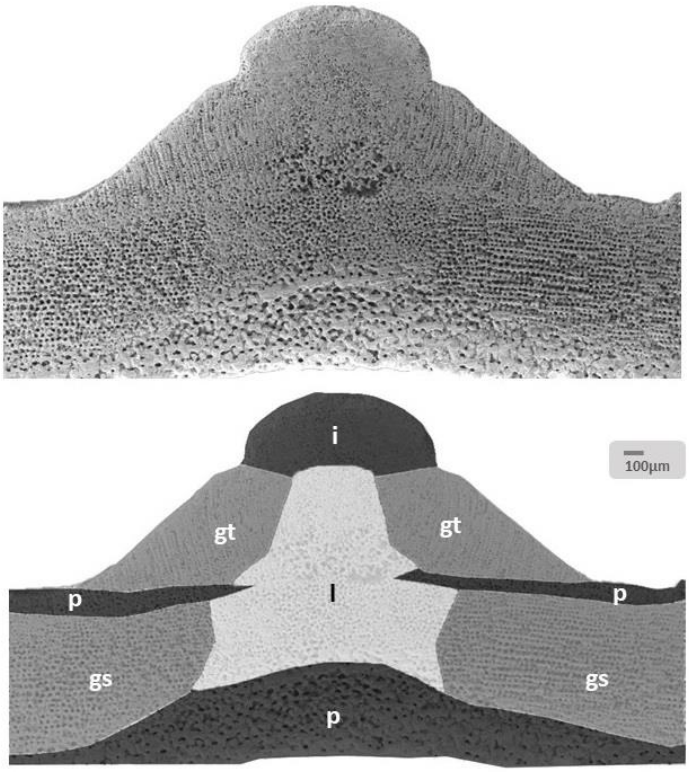

Figure 3.11. *SEM micrographs showing microstructure and stereom variability of the interambulacral plates*. Longitudinal vertical section of the plate showing a high diversity of the stereom microarchitecture according to zones and related specific mechanical needs. Details of stereom types detected: (i) imperforate stereom; (l) labyrinthic stereom; (gt) tubercle galleried stereom; (gs) suture galleried stereom; (p) perforate stereom. Bar = 100 µm.

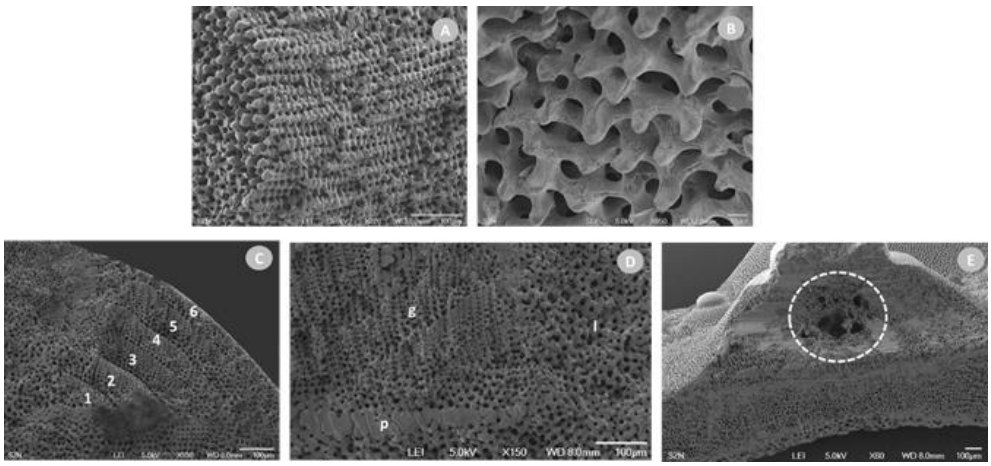

Figure 3.12. SEM micrographs showing stereom variability. A) galleried stereom at suture. B) finger-joint details. Tubercle structure with C) Growth concentric lines and D) details showing stereom types detected: (l) labyrinthic stereom; (g) galleried stereom; (p) perforate stereom. E) Boss internal area characterized by a large open labyrinthic microstructure. Bar = 100 µm

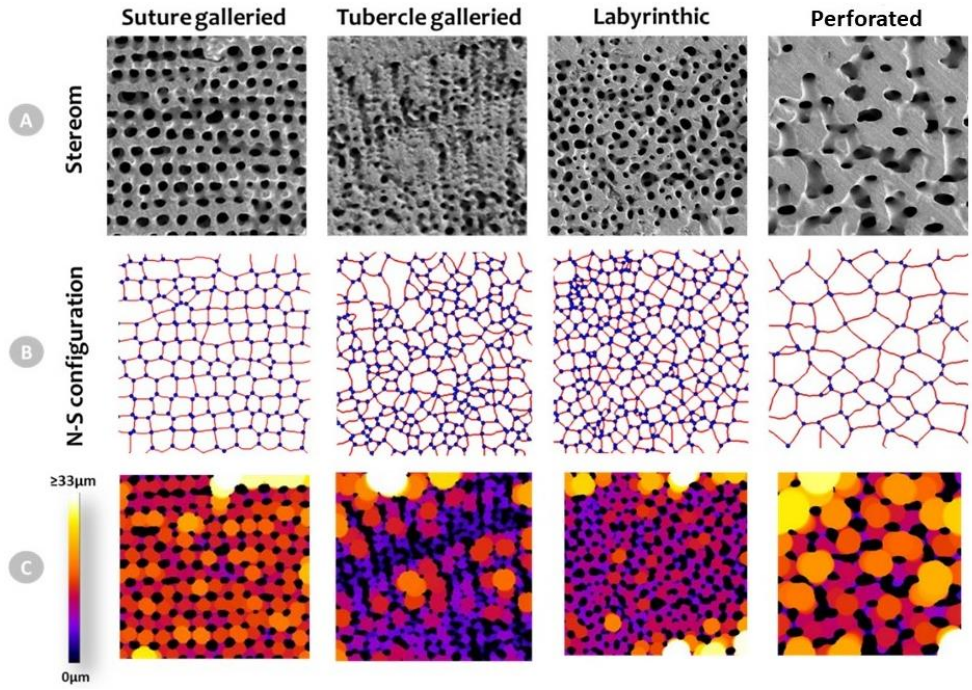

Figure 3.13. Skeleton analyses. A) Investigated stereom types: suture galleried, tubercle galleried, labyrinthic and perforate. B) Node-segment configuration system. C) Thickness map (from 0 to >33 µm)

3.4 Conclusion

In this study, the species-specific structural pattern in the interambulacral plates of the regular echinoid *Paracentrotus lividus* was analysed and described leading to additional understanding of the structural organization and mechanical function of the stereom. In particular:

- The *Paracentrotus lividus* plate shows different structural bands corresponding to a clear sequence of a distinct structural pattern.
- These bands consist of imperforate, galleried, labyrinthic and perforate stereoms.
- The imperforate stereom is a solid calcite layer, characterising the mamelon zone exposed to maximum mechanical stresses produced by the spine action.
- The galleried stereom is present in the tubercle and suture area; however, the tubercle galleried is differentiated from the one at suture in terms of geometry (i.e., number of trabeculae, junctions, trabecular length, radius, thickness, orientation and porosity) and mechanical behaviour.
- The labyrinthic stereom characterises the central part of the plate and consists of a uniformly short and thick system of non-oriented trabeculae with an anisotropic behaviour characterized by a lower stiffness.
- The perforate stereom is a high-density layer characterising the basal plate zone, which is extremely differentiated from all other stereom types and exhibits the stiffer mechanical response.

The combination of SEM micrograph image analysis with FEM provided consistent results and demonstrated the informative value of a 2D study, which are encouraging and provide a starting point for future research. Several aspects of the echinoid microstructural mechanics can be further investigated extending observations to the 3D dimension. Using X-ray microtomography, these studies can include a comprehensive 3D examination of different stereom types and their mechanical behaviour, as well as, the morphological and mechanical analysis of the entire 3D skeletal plate considering the structural differentiation, which are now objects of study by the authors. Due to their unique functional strategies, the echinoid

structure on par of vertebrate bones can provide ideal biomimetic concepts for the development and optimization of manmade lightweight and resistant foam structures and materials.

Note

This chapter has been published as: Perricone, V., Cesarano, P., Mancosu, A., Asnicar, D., Bravi, S., & Marmo, F. (2023). Echinoid skeleton: an insight on the species-specific pattern of the *Paracentrotus lividus* plate and its microstructural variability. *Journal of the Royal Society Interface, 20(199), 20220673*.

Chapter 4

The 3D analysis of the echinoid microarchitecture

In this Chapter, a comprehensive three-dimensional (3D) analysis of the microarchitectural variability within *Paracentrotus lividus* interambulacral plate is provided. Accordingly, different stereom types were selected and analyzed including galleried stereoms at tubercle and suture, labyrinthic stereom at the plate center and the perforate stereom at the basal zone (A. B. Smith, 1980) (Fig.4.1). A combination of micro-CT analysis and finite element analyses (FEA) were used to examine the mechanical behaviour of these lightweight and tough microarchitectures.

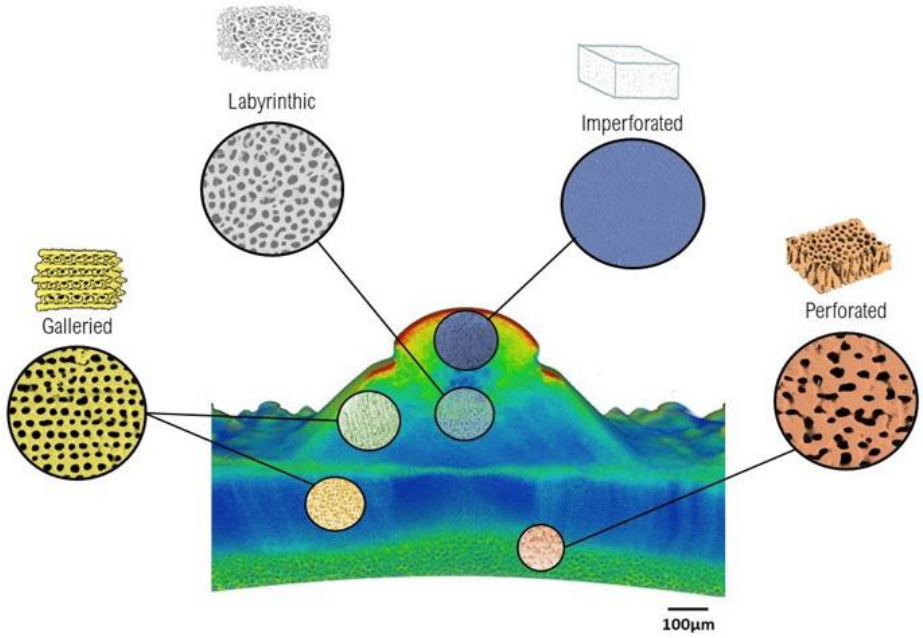

Figure 4.1. Longitudinal section of the micro-CT scan showing stereom variability and highlighting the galleried stereom located at the tubercle boss and suture area, labyrinthic stereom located at the plate center and perforated stereom at the basal zone.

4.1 Materials and methods

Specimens of *Paracentrotus lividus* were collected by scuba divers of the Stazione Zoologica Anton Dohrn in the marine protected area of Porto Cesareo, Italy (40° 16.761′ N, 17° 51.292′ E; February 2023). Animal sampling was performed according to the authorization of Marina Mercantile (DPR 1639/68, 09/19/1980, confirmed by D. Lgs. 9/01/2012 n.4) and in full compliance with the European Union guidelines (directive 2010/63 and following D.Lgs. 4/03/2014 n.26). Test samples were completely digested via treatment in 1 N NaOH (for one week) which completely removed the organic components and provided clean disassembled plates. The samples were then washed three times in deionized water to remove any loose organic debris as well as residual NaOH, and subsequently air-dried, and successively analyzed using X-ray microtomography

4.1.1 X-Ray Microtomography

Intact plates (~ 0.5cm2) from the treated echinoid tests were selected for micro-CT scans at the National Institute of Geophysics and Volcanology (INGV). Scans were carried out using a micro-CT system (Zeiss Xradia 410 Versa) equipped with a microfocus X-ray source with energies ranging from 40 to 150kV, allowing the sample to be scanned with a wide density range. The detectors were mounted on microscope objectives with magnifications ranging from 0.4× to 20×, yielding fields of view of ~ 55mm and~ 1mm respectively. The resulting spatial resolution of these micro-CT images range from ~ 55µm to 0.9µm.

4.1.2 Data processing

Micro-CT data were rendered using ImageJ and Seg3D software. Four subvolumes were oriented, extracted and processed for six different plate regions corresponding to six different stereom types, namely: Stereom 1, corresponding to galleried stereom located at tubercle boss; Stereom 2, galleried stereom at suture area closer to the tubercle; Stereom 3, galleried stereom at suture area closer to the

plate's edges; Stereom 4, labyrinthic stereom located at plate center; Stereom 5 extracted from the plate center, herein rediscovered as an angled galleried stereom; Stereom 6 perforated stereom at the basal zone (Fig. 4.2A). The imperforate stereom present at the mamelon zone has not been considered in this microstructural analysis, due to its highly density layout and the lack of a well-defined trabecular system. The 3D data were analyzed using open-source Python libraries (i.e., SimpleITK, scikit-image, scipy, skan, openCV, numpy, and pandas). Sub-volumes of interest (cubes of 100×100 pixels, corresponding to cubes of 1.485 × 1.485 um) were extracted from the plate scan. Median and Gaussian blur denoising filters were applied to the sub-volumes enhancing the contrast between material (stereom) and the surrounding non-material matrix. Sub-volumes were binarized using interactive thresholding.

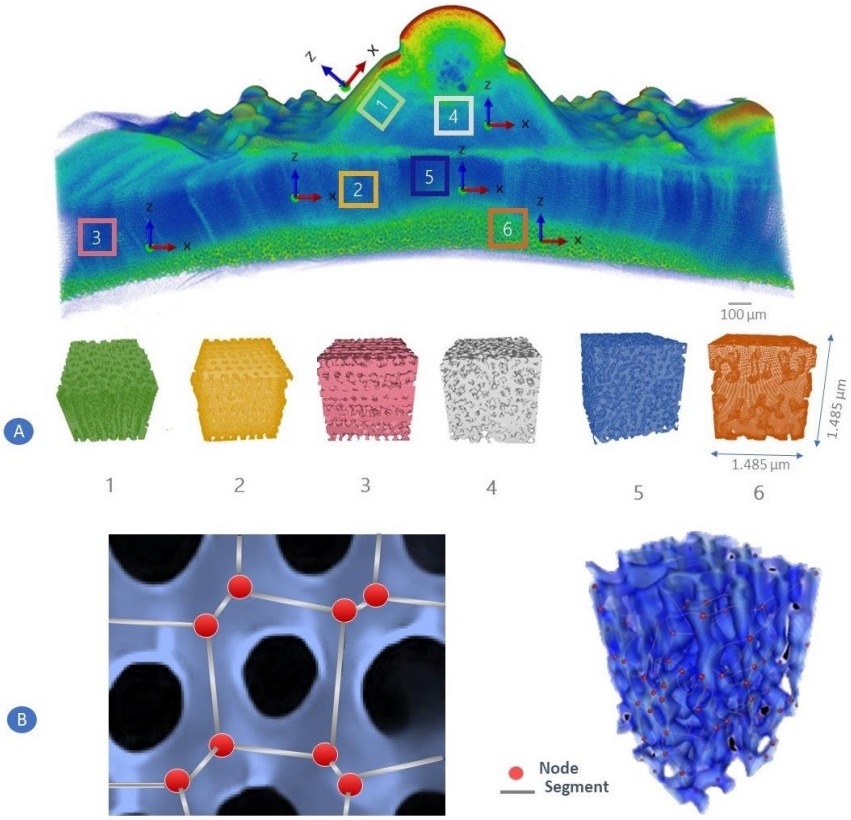

Figure 4.2. (A) Stereom sub-volume selection and x-y-z orientation. (B) Skeletonization process, showing the translation of the microstructure into nodes and segments.

4.1.3 Segment-Node configuration and trabecular analysis

The binarized 3D sub-volume was skeletonized using an implementation of Lee et al. (1994) from the scikit-image library. The skeletonization function transforms the trabecular system into a segment-node configuration: segments are lines equidistant to the boundaries of each trabecula describing their shapes, and nodes are the junctions or intersection points of these segments describing their connectivity. Node-segment configurations of the different microstructures were analyzed to obtain key information regarding the trabecular system (Tab 4.1).

Table 4.1. Trabecular descriptors.

Nodes (N)	Number of connective points and related Euclidean coordinates (x, y, z)
Segments (S)	Number of trabeculae and related Euclidean coordinates of their constitutive points (x, y, z)
Connectivity (C)	Number of trabeculae connected to each node
Chord length (L_c)	Length of the straight line between two nodes
Curved length (L_t)	Length of the approximated curved course of a segment
Tortuosity (τ)	Ratio between curved length and chord length $\tau = L_t/L_c$
Local thickness (T)	Mean value of the minimum distance between the segment point and nearest pore calculated for each point describing a segment
Porosity (P)	Percentage of pore volume in the skeletal sub-volume compared to the entire sub-volume investigated

4.1.4 Finite Element Analysis

The elastic properties of stereoms are influenced by the presence of voids and solid material, along with an even finer ultrastructural inhomogeneities due to compositional and crystallographic variability of the Mg-Calicite. Nonetheless, to understand the response of each architectural type to external forces and deformations, each stereom can be analyzed by computing the averaged elastic properties considering the calcitic material as homogeneous and thus evaluating only the effect of the intricate details of the trabecular system. To this end, a linear elastic finite element analysis (FEA) was here conducted to evaluate the mechanical response of a set of representative volume elements (RVE) derived from the four selected sub-volume of each stereom type. The homogenized stiffness tensor components for each model were computed by averaging the stress-strain relationship within each corresponding RVE.

The geometry of the RVEs were obtained as isosurfaces from the binarized 3D sub-volumes extracted with Seg3D and then processed via SIMULIA Abaqus 2023 software. These isosurfaces were meshed using tetrahedral/hexahedral finite elements. The material properties of these models were assumed to be linearly elastic, with an elastic modulus of $E = 73500\ MPa$ and a Poisson ratio $v = 0.4$, corresponding to solid organic calcite (T. Chen, 2011).

Once the finite element model of RVEs was set, six analyses were performed by applying a uniform distribution of a single strain component $\epsilon_i = 0.00211$, $i = 1,2,...,6$, while keeping the other strain components equal to zero. This analysis used the Voigt notation, in which $\epsilon_1 = \varepsilon_x$, $\epsilon_2 = \varepsilon_y$, and $\epsilon_3 = \varepsilon_z$ represent linear strains, while $_4 = \gamma_{yz}$, $\epsilon_5 = \gamma_{zx}$, and $\epsilon_6 = \gamma_{xy}$, and $\epsilon_6 = \gamma_{xy}$ indicate shear strains. Figure 4.3 illustrates the loading and boundary conditions applied for each case. In each analysis, one of the loading cases was applied to the structure, and the average stress and strain were computed.

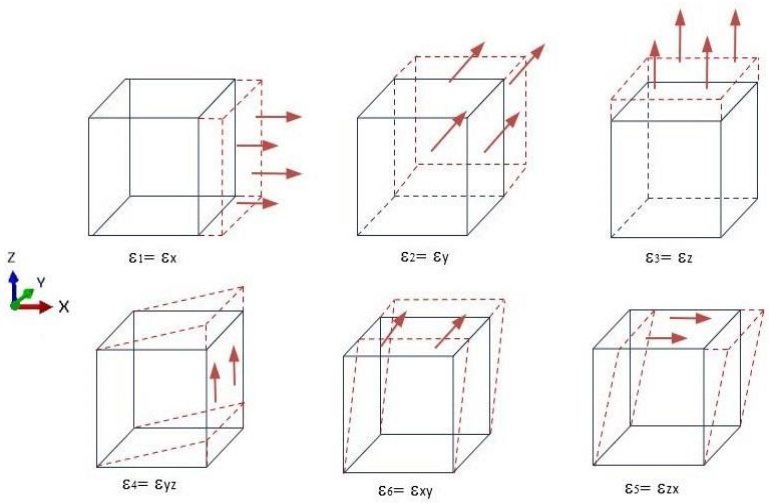

Figure 4.3. Boundary conditions for tensile and shear loading in FEM.

The results of the generic i-th analysis were used to compute the components of the homogenized stiffness tensor associated with the corresponding stereo as:

$$C_{ij} = \frac{\bar{\sigma}_j}{\varepsilon_i} \tag{4.1}$$

Where $\bar{\sigma}_j$ being the average value of the stress component σj computed on the entire volume *V* of the stereom RVE:

$$\bar{\sigma}_j = \frac{\int_V \sigma_j \, dV}{\int_V dV} \tag{4.2}$$

The resulting homogenized stiffness tensors were expected to exhibit anisotropic components. It is possible to identify the directions of higher and lower longitudinal stiffness, represented by the directions $\mathbf{n}_1$ and $\mathbf{n}_3$ along which C_{11} is maximized or minimized, respectively. Once the unit vectors $\mathbf{n}_1$ and $\mathbf{n}_3$ were determined, the third axis of the principal references for the homogenized material was defined as $\mathbf{n}_2 = \mathbf{n}_3 \times \mathbf{n}_1$, which is orthogonal to both these directions. It is important to note that C_{22} and C_{33} are maximized or minimized along directions that are orthogonal to the directions were C_{11} is maximized or minimized. Therefore, there is no practical need to maximize/minimize

these components. To determine the maximum and minimum values of C_{11}, a set of three orthogonal unit vectors was generated, spanning the range of polar and azimuthal angles with intervals of 1 degree. The components of **C** are then computed in the rotated reference frame defined by these unit vectors as basis. To this end, the stiffness tensor C is expressed in the rotated reference using the rotation formula $\mathbf{C' = MCM^T}$, where (A. F. Bower, 2009):

$$M = \begin{bmatrix} i_x^2 & j_x^2 & k_x^2 & 2j_xk_x & 2i_xk_x & 2i_xj_x \\ i_y^2 & j_y^2 & k_y^2 & 2j_yk_y & 2i_yk_y & 2i_yj_y \\ i_z^2 & j_z^2 & k_z^2 & 2j_zk_z & 2i_zk_z & 2i_zj_z \\ i_yi_z & j_yj_z & k_yk_z & j_yk_z + k_yj_z & i_yk_z + k_yi_z & i_yj_z + j_yi_z \\ i_xi_z & j_xj_z & k_xk_z & j_xk_z + k_xj_z & i_xk_z + k_xi_z & i_xj_z + j_xi_z \\ i_xi_y & j_xj_y & k_xk_y & j_xk_y + k_xj_y & i_xk_y + k_xi_y & i_xj_y + j_xi_y \end{bmatrix} \quad (4.3)$$

Where $\mathbf{i} = (i_x, i_y, i_z), \mathbf{j} = (j_x, j_y, j_z), \mathbf{k} = (k_x, k_y, k_z)$ are the unit vectors representing the ortho-normal base of the new reference. Accordingly, $\mathbf{n}_1$ and $\mathbf{n}_3$ are set equal to the unit vectors i that produce, respectively, the minimum and maximum values o C'_{11}.

Successively, the components of **C** in the principal material reference frame, denoted by C_{ij}^p, were then calculated using the rotation formula with $\mathbf{i} = \mathbf{n}_1$, $\mathbf{j} = \mathbf{n}_2$, and $\mathbf{k} = \mathbf{n}_3$. To obtain representative values for the directions of the principal material reference and the principal stiffness tensor components, their average values were computed for each stereom type to account for intratypological material inhomogeneity.

The ratios between the significant principal components of **C** were used to quantify the degree of anisotropy in each stereom. In particular, if the ratios between the averaged stress tensor components $(\text{i.e. } \bar{C}_{ij}^p/\bar{C}_{kl}^p)$ deviate significantly from unity, it indicates that the structure exhibits a high degree of anisotropy and thus directional specialization:

Table 4.2. Nomenclature used for FEM results.

E, ν	Young modulus and Poisson ratio of the basic organic calcitic material
ϵ, ε_i	Strain tensors and relevant components in Voigh notation
$\mathbf{T}, \sigma_i$	Stress tensors and relevant components in Voigh notation
$\mathbf{C}, C_{ji}$	Matrix representation and relevant components associated to the stiffness tensor, expressed in Voight notation $(\sigma_j = C_{ji}\varepsilon_i)$
C^p, C^p_{ji}	Matrix representation and relevant components associated to the stiffness tensor in the principal reference, expressed in Voight notation.
$\mathbf{n}_i$	Base unit vector of the Stiffness principal reference. $\mathbf{n}_1$: direction of maximum longitudinal stiffness, $\mathbf{n}_3$: direction of minimum longitudinal stiffness, $\mathbf{n}_2 = \mathbf{n}_3 \times \mathbf{n}_1$: direction of intermediate longitudinal stiffness.
$\overline{\square}$	Average value of the quantity □ computed for all RVEs of a specific stereom type

To further highlight the elastic behavior of the analysed stereoms, a 3D representation of the relationship between each elastic tensor component and the orientation of the reference frame was generated. From the shape of these 3D directional representations, it is possible to visualize the material's anisotropic behavior (S. G. Lechnickij, 1981) (P. Vannucci, 2018). In particular, the 3D representation of longitudinal stiffness components in an isotropic material appears s a spherical surface, while an elongated surface indicates a higher level of elastic anisotropy.

4.2 Results

4.2.1 Trabecular analysis

The results of the segment-node configuration and trabecular analysis are summarized in Figure 4.4, comparing the different stereom types. All the stereoms show specific length of trabeculae and related thickness with a little tortuosity and similar values of connectivity of about 3. Among them, a clear divergence can be detected in stereom 6, characterized by less number of nodes and segments and larger (longer and thicker) trabeculae with respect to the other stereom types. The porosity is lower in the stereom 1 and 6, while it is higher for steremos 2 - 5, corresponding to the central part of the plate.

Table 4.3. Summary of the trabecular analysis results.

	stereom 1	stereom 2	stereom 3
N	4198.5 ± 423.70	2575.50 ± 173.29	2724.5 ± 72.40
S	5740.75 ± 586.63	3614.00 ± 256.27	4119.25 ± 110.37
C	3.24 ± 0.14	3.12 ± 0.03	3.15 ± 0.03
L_c (μm)	9.60 ± 0.50	10.38 ± 0.20	6.60 ± 0.08
L_t (μm)	7.88 ± 0.31	9.08 ± 0.16	5.73 ± 0.07
τ	1.17 ± 0.02	1.12 ± 0.00	1.12 ± 0.00
T (μm)	2.83 ± 0.02	4.27 ± 0.13	2.66 ± 0.25
P (%)	42.43 ± 2.53	53.38 ± 1.49	57.58 ± 0.89
	stereom 4	stereom 5	stereom 6
N	4641.00 ± 1145.60	5018.50 ± 335.12	975.00 ± 164.54
S	6859.50 ± 1687.69	7753.00 ± 3206.26	1374.50 ± 238.25
C	3.27 ± 0.14	3.44 ± 0.31	3.44 ± 0.00
L_c (μm)	5.34 ± 0.57	7.95 ± 0.60	14.78 ± 0.95
L_t (μm)	4.66 ± 0.47	6.98 ± 0.46	12.70 ± 0.72
τ	1.12 ± 0.00	1.12 ± 0.01	1.14 ± 0.01
T (μm)	2.23 ± 0.25	3.23 ± 0.11	6.50 ± 0.53
P (%)	56.55 ± 2.42	55.40 ± 3.92	41.15 ± 5.00

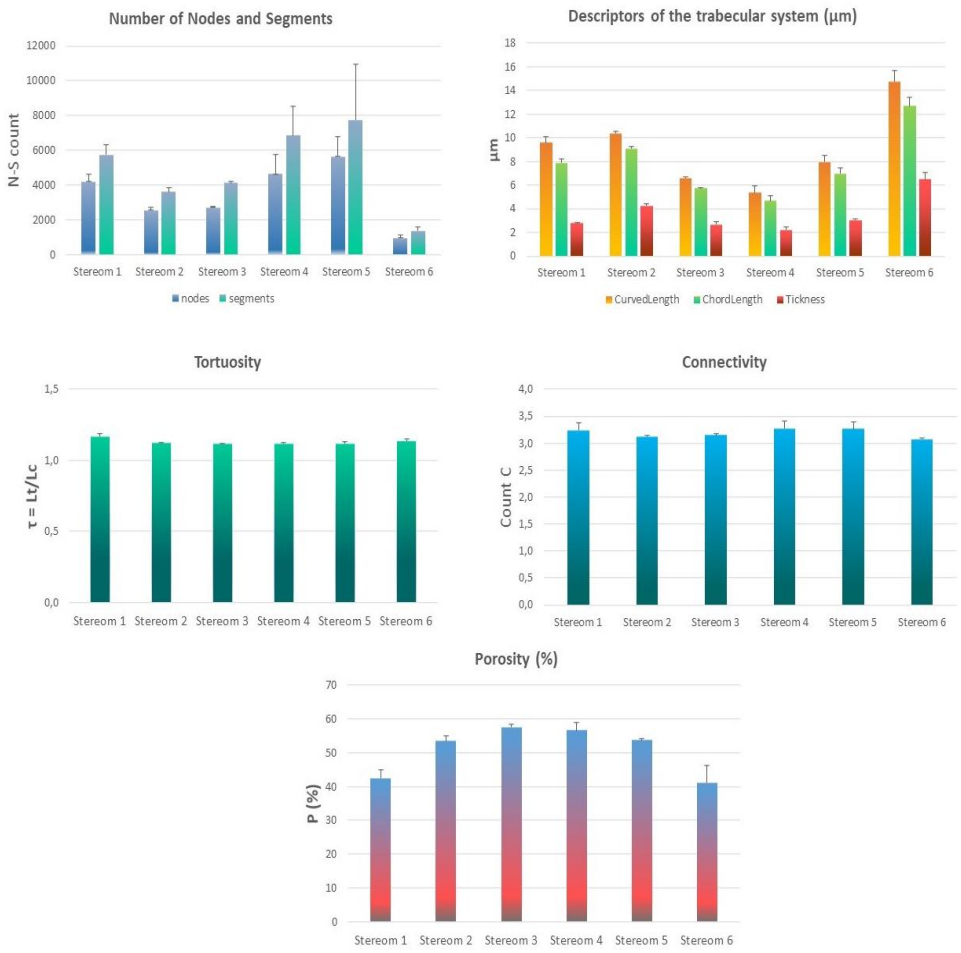

Figure 4.4. Trabecular analysis. Histograms of node–segment configuration, descriptors of the trabecular system, tortuosity, connectivity and porosity comparing the investigated stereom types.

4.2.2 Finite Element Analysis

The stiffness tensor components, expressed in the principal material reference, indicate that all stereoms exhibit an orthotropic elastic behaviour. In fact, both normal-shear and shear-shear coupling values are approximately null (below 0.5% of $\bar{C}_{11}^{p}$) for all stereom types (for more information, see the supplementary material).

The average values of the principal longitudinal stiffness components, as shown in Figure 4.5, demonstrate a clear trend in which stereom 1 and 6 have higher values of longitudinal stiffness compared to the other stereom types.

Stereoms with significantly different principal longitudinal moduli can transfer and redirect stresses along the direction of maximum longitudinal stiffness, while reducing the transmission of stresses in the direction of minimum longitudinal stiffness. As reported by the FEA results, the principal longitudinal stiffness components vary significantly within each stereom type. Specifically, in stereom type 1, the maximum longitudinal stiffness $\bar{C}_{11}^{p}$ is much greater than $\bar{C}_{22}^{p}$ and $\bar{C}_{33}^{p}$, indicating that this stereoms is strongly specialized in the $\mathbf{n}_1$ direction while having relatively lower longitudinal stiffness in the $\mathbf{n}_2 - \mathbf{n}_3$ plane.

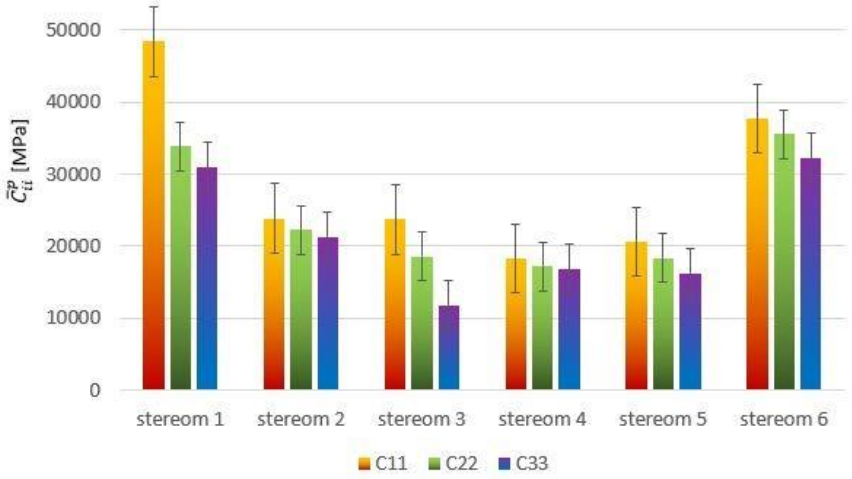

Figure 4.5. Finite Element Analysis. Averaged values of principal longitudinal stiffness components $\bar{\boldsymbol{C}}_{\boldsymbol{11}}^{\boldsymbol{p}}$, $\bar{\boldsymbol{C}}_{\boldsymbol{22}}^{\boldsymbol{p}}$ and $\bar{\boldsymbol{C}}_{\boldsymbol{33}}^{\boldsymbol{p}}$ (in MPa) for each stereom type.

Conversely, the principal longitudinal stiffness values for all other stereom types are almost evenly distributed, indicated a less directional specialization.

Stereom stiffness specialization can also been evaluated by the ratios $\bar{C}_{11}^{p}/\bar{C}_{33}^{p}$. Stereoms with higher values of longitudinal stiffness

show a greater ratio and it can vary significantly across the different stereom type. For example, this ratio can be as high as 2.02 in the stereom 3, indicating a strong anisotropic nature, or as low as 1.09 in stereom 4, which is approximately isotropic.

The streomic stiffness specialization is further highlighted by the shape of the 3D surfaces in Figure 4.6, in which elongated shapes indicate a longitudinal specialization while spherical ones revealed an isotropic nature. The elongated shape of the 3D surfaces in stereom 1 and 6 confirms their high specialization towards the axis of maximum longitudinal stiffness. In contrast, stereom 4, which is almost isotropic, features a nearly spherical surface. The red, green, and blue axes in Figure 6 indicate the orientation of the principal reference frame for each stereom type related with the x − y − z reference of RVEs (for more details, refer to Figure 4.2).

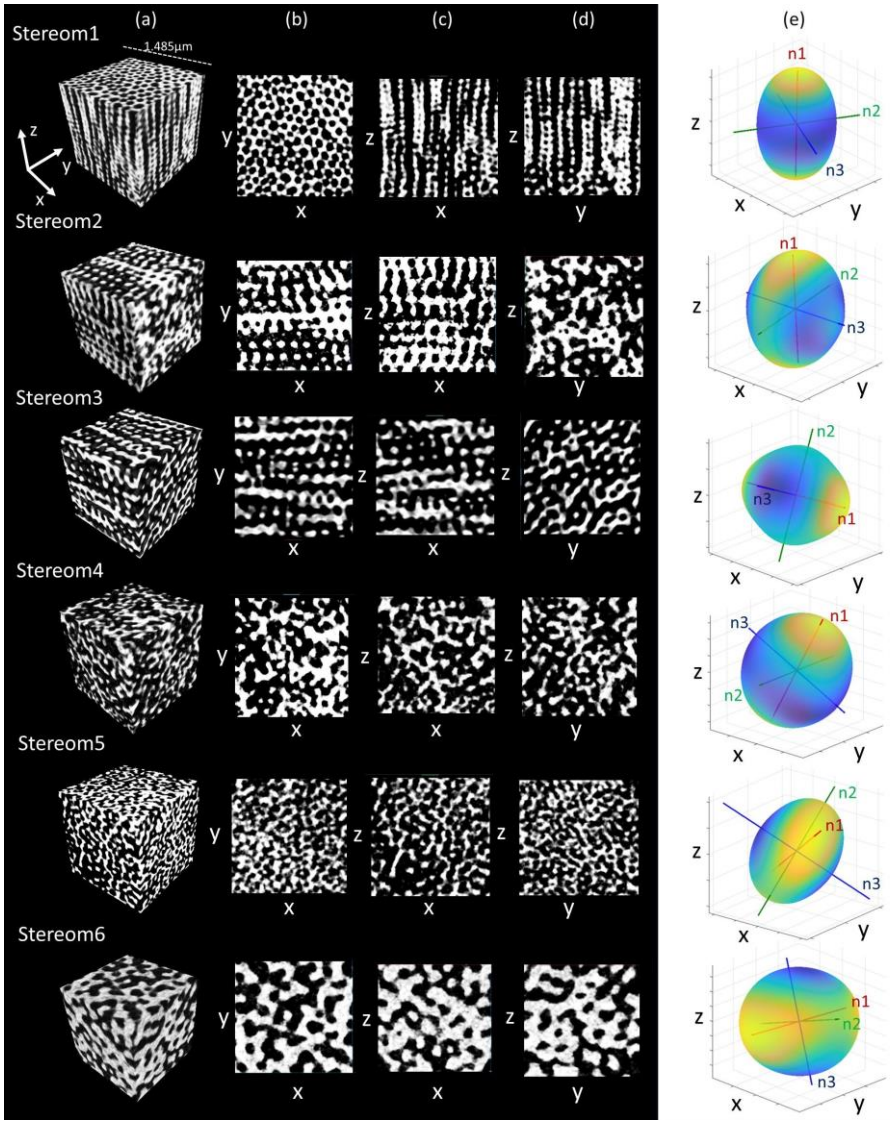

Figure 4.6. Micro-CT scans of the analyzed stereom types (RVE1) showing (a) isometric, (b) coronal, (c) sagittal and (d) transversal views. (e) 3D directional representation of longitudinal stiffness tensor components.

Table 4.4. Average value of the stiffness tensor principal components $\bar{C}_{ij}^{p}$ for each stereom type.

	stereom 1	stereom 2	stereom 3	stereom 4	stereom 5	stereom 6
$\bar{C}_{11}^{p}$ (MPa)	48447	23822	23679	18235	21263	37693
$\bar{C}_{22}^{p}$ (MPa)	33873	22270	18553	17117	19096	35569
$\bar{C}_{33}^{p}$ (MPa)	30934	21245	11712	16764	16532	32297
$\bar{C}_{12}^{p}$ (MPa)	17398	8299	6570	6407	7238	15597
$\bar{C}_{13}^{p}$ (MPa)	16137	7534	4783	6293	6418	14881
$\bar{C}_{23}^{p}$ (MPa)	14091	7003	5346	6098	6106	14064
$\bar{C}_{14}^{p}$ (MPa)	19	2	20	1	2	-4
$\bar{C}_{15}^{p}$ (MPa)	5	0	14	3	8	6
$\bar{C}_{16}^{p}$ (MPa)	58	5	-63	6	-70	-29
$\bar{C}_{24}^{p}$ (MPa)	-21	-100	34	-14	70	-90
$\bar{C}_{25}^{p}$ (MPa)	-6	9	17	-17	28	37
$\bar{C}_{26}^{p}$ (MPa)	6	6	9	0	-2	3
$\bar{C}_{34}^{p}$ (MPa)	-36	-17	6	-16	58	-47
$\bar{C}_{35}^{p}$ (MPa)	0	27	9	-14	24	32
$\bar{C}_{36}^{p}$ (MPa)	111	78	-59	-34	34	-111
$\bar{C}_{44}^{p}$ (MPa)	10632	6794	5716	5645	6414	10446
$\bar{C}_{55}^{p}$ (MPa)	9746	6050	4044	5484	5874	10235
$\bar{C}_{66}^{p}$ (MPa)	8890	5555	4743	5334	5586	9752
$\bar{C}_{45}^{p}$ (MPa)	70	-9	-49	-2	-13	-47
$\bar{C}_{46}^{p}$ (MPa)	1	-6	49	-16	20	7
$\bar{C}_{56}^{p}$ (MPa)	-33	-18	-19	-1	38	-20

Table 4.5. Ratio $\bar{C}_{ij}^{p}/\bar{C}_{pq}^{p}$ between theaverage of the stiffness tensor principal components for stereom all analyzed stereom type.

	stereom 1	stereom 2	stereom 3	stereom 4	stereom 5	stereom 6
$\bar{C}_{11}^{p}/\bar{C}_{22}^{p}$	1.43	1.07	1.28	1.07	1.11	1.06
$\bar{C}_{11}^{p}/\bar{C}_{33}^{p}$	1.57	1.12	2.02	1.09	1.29	1.17
$\bar{C}_{22}^{p}/\bar{C}_{33}^{p}$	1.10	1.05	1.58	1.02	1.16	1.10
$\bar{C}_{12}^{p}/\bar{C}_{13}^{p}$	1.08	1.10	1.37	1.02	1.13	1.05
$\bar{C}_{12}^{p}/\bar{C}_{23}^{p}$	1.23	1.18	1.23	1.05	1.19	1.11
$\bar{C}_{13}^{p}/\bar{C}_{23}^{p}$	1.15	1.08	0.89	1.03	1.05	1.06
$\bar{C}_{44}^{p}/\bar{C}_{55}^{p}$	1.09	1.12	1.41	1.03	1.09	1.02
$\bar{C}_{44}^{p}/\bar{C}_{66}^{p}$	1.20	1.22	1.20	1.06	1.15	1.07
$\bar{C}_{55}^{p}/\bar{C}_{66}^{p}$	1.10	1.09	0.85	1.03	1.05	1.05

4.3 Discussion

In this study, the microstructural variation and regional mechanics of the inter-ambulacral plates of *Paracentrotus lividus* were determined in a 3D coordinate system, leading to new and interesting insights. In 1980, Smith first classified the different structural bands within *Paracentrotus lividus* plates as follow (Fig.4.7(A)): a galleried stereom located at tubercle boss and sutures (1,2,3), a labyrinthic stereom at the center of the tubercle and of the plate (4), and a perforated stereom at the basal zone (6) (A. B. Smith, 1980). In a previous work, Perricone et al. (2023) analyzed the same species-specific structural pattern in a 2D system leading to an additional understanding of the structural organization and mechanical function of the stereom.

In the present study X-ray microtomography was used to retrieve the 3D geometric features of a series of representative volumes of the stereom extracted from different regions of the inter-ambulacral plates of *Paracentrotus lividus*. These scans were analyzed to obtain geometric and elastic information regarding the trabecular system that characterizes each analysed stereom type. Each stereo showed unique topological features and variable porosity between (41.155.0%) (stereom 6) and (56.552.4%) (stereom 4), similar to the values detected in the periodic stereom at the tubercle of the sea urchin Phyllacanthus imperialis (53.2%) (H. Ji et. Al, 2022) and radaiting layer (383.8%) and the medulla of Heterocentrotus mamillatus (614.8%) (V. Presser et al., 2010). In particular, FEA confirmed and highlighted important differences among the different stereom types with respect to their trabecular configuration and elastic behavior and allowed as to formulate a new plate model (Fig. 4.7(B)) that slightly differentiates from the one described by A. B. Smith (1980).

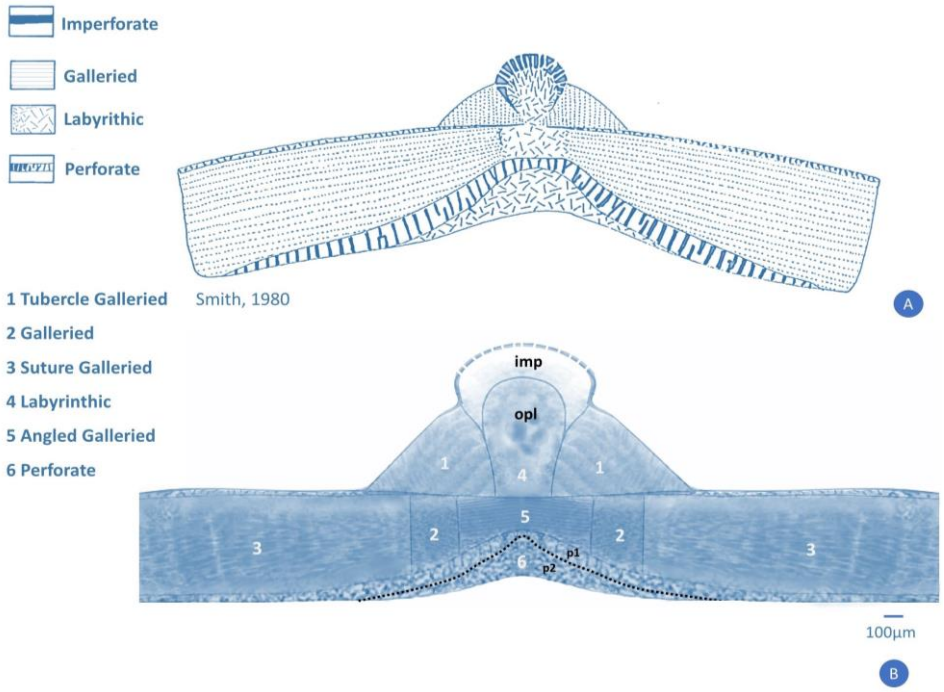

Figure 4.7. Stereom organization and comparison with previous literature (A.B. Smith, 1980). Species-specific pattern of *P. Lividus* in A) Smith's model and B) reformulated model. The main stereom types analyzed are reported, emphasizing the main differences, including the differentiation between the galleried stereoms 2 and 3, and the identification of the stereom 5 as an angled galleried stereom, previously reported as labyrinthic stereom. imp=imperforate; opl=open labyrinthic stereom.

4.3.1 Stereom 1: the galleried stereom located at the tubercle boss

Stereom 1 corresponds to the galleried stereom located at the tubercle boss and it is characterized by numerous trabeculae aligned with the direction orthogonal to the tubercle lateral surface. The stereom consists of numerous parallel pores visible in the zx and zy planes (Figure 4.6(a)), which have been previously described to be arranged as a Voronoi construction with a prevalence of hexagonal polygons, and a regularly organized seed distribution (V. Perricone et al., 2022). Moreover, as previously reported in the 2D analysis (V. Perricone et al., 2023), the 3D geometrical analysis also confirms that this galleried stereom differs from those located at the suture in terms of number of nodes, segments, curved length, chord length, thickness

and porosity. The high values of the ratios C_{11}^p/C_{22}^p and C_{11}^p/C_{33}^p characterizes all RVEs and highlight the anisotropic behavior and the directional stiffness specialization of stereom 1. This is confirmed by the elongated shape of the 3D surfaces representing the directional variation of the longitudinal stiffness components (Fig. 4.6(e)). The Poisson and shear effects are less significant compared to those in the longitudinal direction. The direction of maximum longitudinal stiffness ($\mathbf{n}_1$) is aligned with the normal to the lateral surface of the tubercle, while the two directions of lower longitudinal stiffness ($\mathbf{n}_2$ and $\mathbf{n}_3$) lay on the plane tangential to this surface (Fig. 4.8).

Such high uni-directional specialization in stereom 1, which can effectively withstand longitudinal stresses, presents clear insights into the function of the tubercle stereom in living organisms. Indeed, this ordered stereom offers an attachment site for the catch apparatus fibers connecting the spine to the tubercle, which is therefore subjected to intense directional and impact stresses (K. TAKAHASHI, 1967), (M. Hidaka et al., 1983), (J. De Castillo et al., 1995), (H. Ji et al., 2022). Recently, H. Ji et al. (2022) reported how the periodic stereom structures at the tubercle of the sea urchin *Phyllacanthus imperialism* provide an excellent fracture resistance and energy dissipation capacity with relatively high porosity (50.6%). Another characteristic of stereom 1, which is not fully investigated and requires additional analysis, is related to its growth banding that could presumably influence the mechanical response of the tubercle as has already been assessed in the spines (J. N. Grossman et al., 2013), (K. Nickel et al., 2018), (V. Presser et al., 2009).

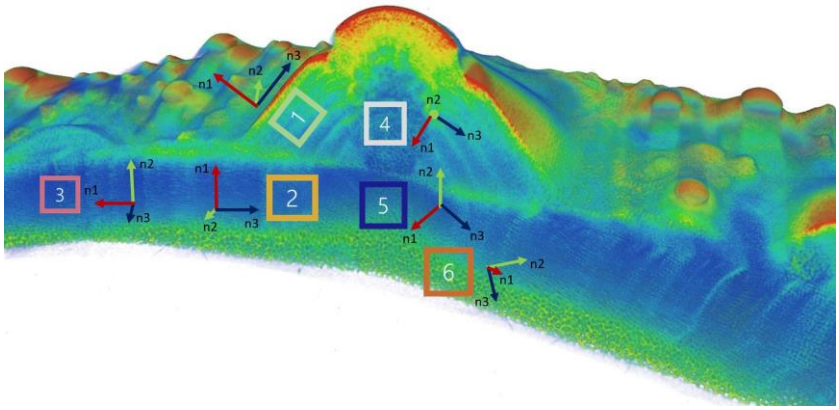

Figure 4.8. Principal stiffness direction of analyzed stereom types; $\mathbf{n}_1$: direction of maximum longitudinal stiffness, $\mathbf{n}_3$: direction of minimum longitudinal stiffness, $\mathbf{n}_2 = \mathbf{n}_3 \times \mathbf{n}_1$: direction of intermediate longitudinal stiffness.

Table 4.6. Stiffness tensor principal components C_{ij}^{p} for stereom type 1.

	stereom 1			
	RVE 1	RVE 2	RVE 3	RVE 4
C_{11}^{p} (MPa)	48149	46212	46762	52663
C_{22}^{p} (MPa)	32237	32570	31685	39002
C_{33}^{p} (MPa)	31183	29113	29684	33758
C_{12}^{p} (MPa)	16748	16402	16246	20198
C_{13}^{p} (MPa)	16332	14847	15491	17879
C_{23}^{p} (MPa)	13863	13153	13359	15987
C_{14}^{p} (MPa)	36	-14	19	34
C_{15}^{p} (MPa)	32	-4	-15	7
C_{16}^{p} (MPa)	-58	114	78	96
C_{24}^{p} (MPa)	-39	154	-68	-131
C_{25}^{p} (MPa)	27	-20	-16	-15
C_{26}^{p} (MPa)	-7	-7	8	28
C_{34}^{p} (MPa)	-31	74	-40	-146
C_{35}^{p} (MPa)	79	133	-56	-154
C_{36}^{p} (MPa)	-305	214	390	144
C_{44}^{p} (MPa)	10214	10386	10007	11920
C_{55}^{p} (MPa)	9909	9188	9601	10286
C_{66}^{p} (MPa)	8769	8457	8547	9788
C_{45}^{p} (MPa)	19	86	98	77
C_{46}^{p} (MPa)	15	5	-25	9
C_{56}^{p} (MPa)	-10	40	-27	-135

Table 4.7. Values of the ratio C_{ij}^{p}/C_{pq}^{p} between the stiffness tensor principal components for stereom type 1.

	stereom 1			
	RVE 1	RVE 2	RVE 3	RVE 4
C_{11}^{p}/C_{22}^{p}	1.49	1.42	1.48	1.35
C_{11}^{p}/C_{33}^{p}	1.55	1.59	1.58	1.56
C_{22}^{p}/C_{33}^{p}	1.03	1.12	1.07	1.16
C_{12}^{p}/C_{13}^{p}	1.03	1.10	1.05	1.13
C_{12}^{p}/C_{23}^{p}	1.21	1.25	1.22	1.26
C_{13}^{p}/C_{23}^{p}	1.18	1.13	1.16	1.12
C_{44}^{p}/C_{55}^{p}	1.03	1.13	1.05	1.16
C_{44}^{p}/C_{66}^{p}	1.16	1.23	1.18	1.22
C_{55}^{p}/C_{66}^{p}	1.13	1.09	1.12	1.05

Table 4.8. Principal stiffness direction of stereom type 1. $\mathbf{n}_1$: direction of max-imum longitudinal stiffness, n3: direction of minimum longitudinal stiffness, $\mathbf{n}_2 = \mathbf{n}_3 \times \mathbf{n}_1$: direction of intermediate longitudinal stiffness.

	stereom 1			
	RVE 1	RVE 2	RVE 3	RVE 4
n_{1x}	0.0161	-0.0119	-0.0138	0.0006
n_{1y}	0.0068	-0.0328	-0.0107	-0.0349
n_{1z}	0.9998	0.9994	0.9998	0.9994
n_{2x}	0.4225	0.4846	0.3255	0.2419
n_{2y}	0.9063	0.8741	0.9454	0.9697
n_{2z}	-0.0130	0.0345	0.0146	0.0337
n_{3x}	0.9062	0.8747	0.9455	0.9703
n_{3y}	-0.4227	-0.4847	-0.3256	-0.2418
n_{3z}	-0.0117	-0.0055	0.0095	-0.0090

4.3.2 Stereom 2 and 3: the non-uniform galleried stereom located at the suture region

The microstructure identified by Smith (1980) as galleried stereom located at the suture region exhibits a gradual variation of geometry. In our study, we selected two representative stereom types extracted from this apparently uniform microstructure, namely stereom 2 and 3. They are respectively extracted near the tubercle and closer to the plate sutures and consist of pores that are parallelly organized in the *yx* and *zx* planes (Fig. 4.4). A visual analysis of stereoms 2 shows the similarity with stereom 3 since both stereom types are characterized

by galleries parallel to the *x* axis. However, differently from stereom 3, stereom 2 presents some elongated elements parallel to *y* and *z*, see, e.g. Figure 4.6 (a and b).

While they may show a similar number of trabeculae and connections (see node-segment configuration in Fig. 4.4), the trabecular length and porosity are quite different in these stereoms. Furthermore, FEA results indicate that these stereoms exhibit very different elastic behaviour, despite the visual similarity.

In particular, the ratios C_{11}^p/C_{22}^p and C_{11}^p/C_{33}^p, which have average values 1.28 and 2.02 in stereom 3, are significantly higher than the corresponding ratios in stereom 2, with average 1.07 and 1.12, see, e.g. the supplementary material. While stereom 2 is almost isotropic, it exibits a maximum longitudinal stiffness in the direction orthogonal to plate mid-surface (*z*), which is interestingly orthogonal to the direction of galleries (*x*) and aligned with the elongated elements visible in Figure 4.6 (a and b). The values of the principal longitudinal stiffness of all RVEs of stereom 3, instead, indicate two stiffer directions ($\mathbf{n}_1$ and $\mathbf{n}_2$), the first parallel to the longitudinal direction of the plate (*x*) and the second orthogonal to the plate mid-surface (*y*). The compliant direction ($\mathbf{n}_3$) is directed along the plate transversal direction (*z*).

The differences between stereom types 2 and 3 show that galleried stereom is characterized by an increased stiffness specialization while moving from the plate center toward its edges. This may be associated with the necessity to directionally distribute the stress from the spine actions into the suture. Actually, the coronal, sagittal and transversal sections of the entire plate shown in Figure 4.9 (A-C) display the varying orientation of the galleried stereom departing from the plate center towards the plate edges. Studies in the literature reported that the trabeculae with a periodic arrangement are able to disseminate applied stresses directionally onto the adjacent ones, decreasing the chance of a localized structural failure (V. Perricone et al., 2022), (M. J. Silva et al., 1997). This suggests a significant adaptive purpose and is especially beneficial at the edges. Consider also that this stereom functions as an attachment site for short sutural collagen fibers connecting adjacent plates (A. Mancosu et al., 2020).

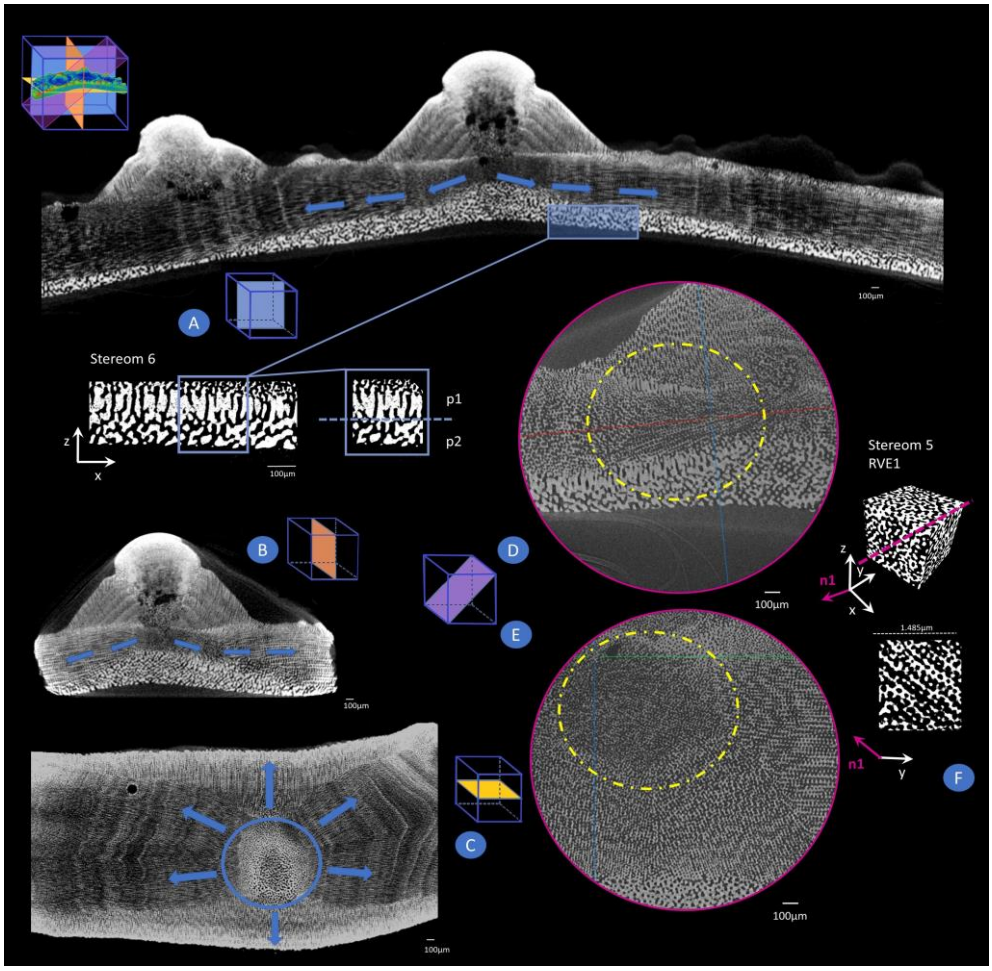

Figure 4.9. Micro-CT scan of *P.Lividus* plate from the following plane prospectives: A) coronal plane, including a detail of perforated stereom 6 (p1 and p2), B) transversal plane and C) sagittal plane, showing the galleries departing from the center of the primary tubercle with growth bandings (blu arrows). D) and E) angled plane respective of the coronal and sagittal plane respectively revealing the galleried of the stereom 5. F) Representative RVE1 of the stereom 5 with a layer cut at 63° showing the angled galleries.

Table 4.9. Stiffness tensor principal components C_{ij}^{p} for stereom type 2

	stereom 2			
	RVE 1	RVE 2	RVE 3	RVE 4
C_{11}^{p} (MPa)	23846	21617	25032	24792
C_{22}^{p} (MPa)	21925	20820	23983	22350
C_{33}^{p} (MPa)	20689	19171	22954	22165
C_{12}^{p} (MPa)	8349	6835	9218	8793
C_{13}^{p} (MPa)	7149	7283	7943	7761
C_{23}^{p} (MPa)	6742	6312	7756	7203
C_{14}^{p} (MPa)	-1	-4	11	3
C_{15}^{p} (MPa)	2	5	-5	-1
C_{16}^{p} (MPa)	7	2	-13	26
C_{24}^{p} (MPa)	-55	-536	140	51
C_{25}^{p} (MPa)	6	39	15	-24
C_{26}^{p} (MPa)	-18	27	35	-20
C_{34}^{p} (MPa)	-44	-22	16	-17
C_{35}^{p} (MPa)	-56	-18	6	177
C_{36}^{p} (MPa)	229	-72	7	150
C_{44}^{p} (MPa)	6955	5621	7432	7170
C_{55}^{p} (MPa)	5743	6083	6229	6145
C_{66}^{p} (MPa)	5399	5102	6026	5694
C_{45}^{p} (MPa)	0	-35	-4	4
C_{46}^{p} (MPa)	-27	16	-8	-6
C_{56}^{p} (MPa)	-50	-6	17	-31

Table 4.10. Values of the ratio C_{ij}^{p}/C_{pq}^{p} between the stiffness tensor principal components for stereom type 2.

	stereom 2			
	RVE 1	RVE 2	RVE 3	RVE 4
C_{11}^{p}/C_{22}^{p}	1.09	1.04	1.04	1.11
C_{11}^{p}/C_{33}^{p}	1.15	1.13	1.09	1.12
C_{22}^{p}/C_{33}^{p}	1.06	1.09	1.04	1.01
C_{12}^{p}/C_{13}^{p}	1.17	0.94	1.16	1.13
C_{12}^{p}/C_{23}^{p}	1.24	1.08	1.19	1.22
C_{13}^{p}/C_{23}^{p}	1.06	1.15	1.02	1.08
C_{44}^{p}/C_{55}^{p}	1.21	0.92	1.19	1.17
C_{44}^{p}/C_{66}^{p}	1.29	1.10	1.23	1.26
C_{55}^{p}/C_{66}^{p}	1.06	1.19	1.03	1.08

Table 4.11. Principal stiffness direction of stereom type 2. $\mathbf{n}_1$: direction of max-imum longitudinal stiffness, n3: direction of minimum longitudinal stiffness, $\mathbf{n}_2 = \mathbf{n}_3 \times \mathbf{n}_1$: direction of intermediate longitudinal stiffness.

	stereom 2			
	RVE 1	RVE 2	RVE 3	RVE 4
n_{1x}	0.0181	0.1039	-0.0063	0.0429
n_{1y}	-0.0853	-0.1600	-0.0163	-0.0550
n_{1z}	0.9962	0.9816	0.9998	0.9976
n_{2x}	-0.0690	0.9915	-0.0349	-0.0685
n_{2y}	0.9939	0.0944	0.9993	0.9960
n_{2z}	0.0863	-0.0896	0.0161	0.0578
n_{3x}	-0.9975	-0.0783	-0.9994	-0.9967
n_{3y}	-0.0703	0.9826	-0.0348	-0.0708
n_{3z}	0.0121	0.1685	-0.0068	0.0390

Table 4.12. Stiffness tensor principal components C_{ij}^{p} for stereom type 3.

	stereom 3			
	RVE 1	RVE 2	RVE 3	RVE 4
C_{11}^{p} (MPa)	21824	23600	25144	24147
C_{22}^{p} (MPa)	17814	18642	19128	18629
C_{33}^{p} (MPa)	13398	11546	10275	11631
C_{12}^{p} (MPa)	6290	6576	6790	6625
C_{13}^{p} (MPa)	5197	4692	4460	4785
C_{23}^{p} (MPa)	5916	5267	4859	5343
C_{14}^{p} (MPa)	44	11	23	4
C_{15}^{p} (MPa)	36	3	12	5
C_{16}^{p} (MPa)	-73	-54	6	-132
C_{25}^{p} (MPa)	92	11	4	-39
C_{26}^{p} (MPa)	24	-30	41	0
C_{34}^{p} (MPa)	29	15	11	-33
C_{35}^{p} (MPa)	98	39	-41	-59
C_{36}^{p} (MPa)	66	-66	93	-330
C_{44}^{p} (MPa)	5391	5699	6029	5744
C_{55}^{p} (MPa)	4407	3872	3914	3983
C_{66}^{p} (MPa)	5067	4648	4484	4774
C_{45}^{p} (MPa)	-31	-75	17	-106
C_{46}^{p} (MPa)	225	-4	-24	0
C_{56}^{p} (MPa)	-54	3	0	-25

Table 4.13. Values of the ratio C_{ij}^{p}/C_{pq}^{p} between the stiffness tensor principal components for stereom type 3.

	stereom 3			
	RVE 1	RVE 2	RVE 3	RVE 4
C_{11}^{p}/C_{22}^{p}	1.23	1.27	1.31	1.30
C_{11}^{p}/C_{33}^{p}	1.63	2.04	2.45	2.08
C_{22}^{p}/C_{33}^{p}	1.33	1.61	1.86	1.60
C_{12}^{p}/C_{13}^{p}	1.21	1.40	1.52	1.39
C_{12}^{p}/C_{23}^{p}	1.06	1.25	1.40	1.24
C_{13}^{p}/C_{23}^{p}	0.88	0.89	0.92	0.90
C_{44}^{p}/C_{55}^{p}	1.22	1.47	1.54	1.44
C_{44}^{p}/C_{66}^{p}	1.06	1.23	1.34	1.20
C_{55}^{p}/C_{66}^{p}	0.87	0.83	0.87	0.83

Table 4.14. Principal stiffness direction of stereom type 3. $\mathbf{n}_1$: direction of max-imum longitudinal stiffness, n3: direction of minimum longitudinal stiffness, $\mathbf{n}_2 = \mathbf{n}_3 \times \mathbf{n}_1$: direction of intermediate longitudinal stiffness.

	stereom 3			
	RVE 1	RVE 2	RVE 3	RVE 4
n_{1x}	-0.9939	-0.9951	-0.9938	-0.9998
n_{1y}	-0.1045	-0.0696	-0.0695	-0.0175
n_{1z}	-0.0349	-0.0698	-0.0872	0.0000
n_{2x}	-0.0770	-0.0964	-0.1115	-0.0112
n_{2y}	0.4327	0.5392	0.6231	0.6427
n_{2z}	0.8982	0.8366	0.7742	0.7660
n_{3x}	-0.0787	-0.0206	0.0005	-0.0134
n_{3y}	0.8955	0.8393	0.7791	0.7659
n_{3z}	-0.4381	-0.5433	-0.6269	-0.6428

4.3.3 Stereom 4 and 5: the labyrithic stereom located at the tubercle center and the transition zone towards an inclined galleried microstructure

In its plate model (A. B. Smith, 1980), Smith reported a labirinthic stereom at the center of the tubercle and at the plate center which seem to be classified as a unique microstructure, as in fact seems apparently deducible from a 2D perspective (V. Perricone et al., 2023). We extracted four RVEs for both these locations, namely stereom 4, at the center of the tubercle, and stereom 5, located at the center of the plate, just underneat the tubercle. Both stereoms present a

geometry which is apparently not ordered if observed on the principal anatomical planes of the inter-ambulacral plate, see, e.g., Figure 4.6 (a-d). However, the different material scale visible in such views produces the geometric differences in the microstructure in terms of porosity, length, and thickness of the trabecular system (Figure 4.4).

FEM analyses highlighted the different elastic behaviour of these microstructures. In particular, the ratios C_{11}^p/C_{22}^p and C_{11}^p/C_{33}^p assume values close to unity for all RVEs of stereom 4, showing its almost isotropic behaviour. The slight spherical shape of the 3D directional representation of the longitudinal stiffness of stereom 4 indicated the lack of any definite stiffness specialization of such microstructure.

Conversely, the ratios C_{11}^p/C_{22}^p and C_{11}^p/C_{33}^p reached the values 1.45 and 1.28 for RVE 1 of stereom 5, demonstrating its anisotropic nature. The elongated 3D surface representing the directional dependence of its longitudinal stiffness confirmed the clear specialization of stereom 5. Additionally, stereom 5 revealed a non-homogeneous microstructure since RVE 2 resulted almost isotropic, while RVEs 3 and 4 are clearly anisotropic, with lower stiffness specialization with respect to RVE 1. A further 3D inspection has revealed the presence of distinct galleries departing from the center of the plate toward the suture edges, with an angled orientation, as clearly shown in Figure 4.9 (D) and (E). A cross section of RVE 1 of stereom 5 with the plane defined by *y* and $\mathbf{n}_1$, that is the axis of the maximum longitudinal stiffness, exposed the galleried microstructure parallel to $\mathbf{n}_1$, see, i.e., Figure 4.9 (F).

Consequently, the stereom 5 could be classified as an inclined galleried stereom and, eventually, the plate center could be considered a region of transition between a labirinthic, non-ordered, isotropic microstructure, such as RVE 2 of stereom 5, that gradually specializes to an inclined galleried microstructure, such as RVE 1 of stereom 5.

Table 4.15. Stiffness tensor principal components C_{ij}^{p} for stereom type 4.

	stereom 4			
	RVE 1	RVE 2	RVE 3	RVE 4
C_{11}^{p} (MPa)	17319	18222	16300	21097
C_{22}^{p} (MPa)	15753	17472	15572	19671
C_{33}^{p} (MPa)	15594	17044	15274	19144
C_{12}^{p} (MPa)	5883	6527	5741	7479
C_{13}^{p} (MPa)	5824	6369	5695	7283
C_{23}^{p} (MPa)	5513	6291	5584	7002
C_{14}^{p} (MPa)	-1	0	0	5
C_{15}^{p} (MPa)	7	-1	6	0
C_{16}^{p} (MPa)	19	-6	-16	28
C_{24}^{p} (MPa)	18	-56	55	-75
C_{25}^{p} (MPa)	-59	33	16	-56
C_{26}^{p} (MPa)	2	0	-1	-1
C_{34}^{p} (MPa)	126	-74	-12	-105
C_{35}^{p} (MPa)	-179	217	148	-243
C_{36}^{p} (MPa)	-62	109	-106	-77
C_{44}^{p} (MPa)	5302	5746	5032	6502
C_{55}^{p} (MPa)	5173	5543	4966	6253
C_{66}^{p} (MPa)	4966	5469	4838	6062
C_{45}^{p} (MPa)	23	-3	-41	15
C_{46}^{p} (MPa)	-59	29	7	-43
C_{56}^{p} (MPa)	114	-44	-13	-61

Table 4.16. Values of the ratio C_{ij}^{p}/C_{pq}^{p} between the stiffness tensor principal components for stereom type 4.

	stereom 4			
	RVE 1	RVE 2	RVE 3	RVE 4
C_{11}^{p}/C_{22}^{p}	1.10	1.04	1.05	1.07
C_{11}^{p}/C_{33}^{p}	1.11	1.07	1.07	1.10
C_{22}^{p}/C_{33}^{p}	1.01	1.03	1.02	1.03
C_{12}^{p}/C_{13}^{p}	1.01	1.02	1.01	1.03
C_{12}^{p}/C_{23}^{p}	1.07	1.04	1.03	1.07
C_{13}^{p}/C_{23}^{p}	1.06	1.01	1.02	1.04
C_{44}^{p}/C_{55}^{p}	1.03	1.04	1.01	1.04
C_{44}^{p}/C_{66}^{p}	1.07	1.05	1.04	1.07
C_{55}^{p}/C_{66}^{p}	1.04	1.01	1.03	1.03

Table 4.17. Principal stiffness direction of stereom type 4. $\mathbf{n}_1$: direction of max-imum longitudinal stiffness, n3: direction of minimum longitudinal stiffness, $\mathbf{n}_2 = \mathbf{n}_3 \times \mathbf{n}_1$: direction of intermediate longitudinal stiffness.

	stereom 4			
	RVE 1	RVE 2	RVE 3	RVE 4
n_{1x}	-0.4496	-0.1528	-0.1923	-0.0806
n_{1y}	-0.0632	0.4439	0.1732	0.5087
n_{1z}	-0.8910	-0.8829	-0.9659	-0.8572
n_{2x}	-0.0617	0.4346	0.7938	0.3289
n_{2y}	0.9973	0.8326	0.6062	0.8254
n_{2z}	-0.0396	0.3433	-0.0494	0.4589
n_{3x}	0.8911	0.8876	0.5770	0.9409
n_{3y}	0.0372	-0.3313	-0.7763	-0.2450
n_{3z}	-0.4523	-0.3202	-0.2541	-0.2338

Table 4.18. Stiffness tensor principal components $\boldsymbol{C_{ij}^p}$ for stereom type 5.

	stereom 5			
	RVE 1	RVE 2	RVE 3	RVE 4
C_{11}^p (MPa)	22335	19977	22771	19970
C_{22}^p (MPa)	19706	18135	20835	17709
C_{33}^p (MPa)	15351	18128	17057	15594
C_{12}^p (MPa)	7500	6881	7850	6722
C_{13}^p (MPa)	6171	6841	6868	5793
C_{23}^p (MPa)	5786	6330	6561	5748
C_{14}^p (MPa)	14	-3	-8	4
C_{15}^p (MPa)	20	-3	19	-2
C_{16}^p (MPa)	-172	-158	115	-66
C_{24}^p (MPa)	-173	-81	282	252
C_{25}^p (MPa)	-11	28	16	80
C_{26}^p (MPa)	9	0	-7	-9
C_{34}^p (MPa)	-8	123	75	43
C_{35}^p (MPa)	17	-110	106	85
C_{36}^p (MPa)	-35	12	-38	196
C_{44}^p (MPa)	6695	5917	6840	6204
C_{55}^p (MPa)	5648	6286	6020	5542
C_{66}^p (MPa)	5344	5824	5720	5456
C_{45}^p (MPa)	-118	-71	91	45
C_{46}^p (MPa)	93	-90	106	-27
C_{56}^p (MPa)	-77	186	47	-4

Table 4.19. Values of the ratio C_{ij}^{p}/C_{pq}^{p} between the stiffness tensor principal components for stereom type 5.

	stereom 5			
	RVE 1	RVE 2	RVE 3	RVE 4
C_{11}^{p}/C_{22}^{p}	1.13	1.10	1.09	1.13
C_{11}^{p}/C_{33}^{p}	1.45	1.10	1.33	1.28
C_{22}^{p}/C_{33}^{p}	1.28	1.00	1.22	1.14
C_{12}^{p}/C_{13}^{p}	1.22	1.01	1.14	1.16
C_{12}^{p}/C_{23}^{p}	1.30	1.09	1.20	1.17
C_{13}^{p}/C_{23}^{p}	1.07	1.08	1.05	1.01
C_{44}^{p}/C_{55}^{p}	1.19	0.94	1.14	1.12
C_{44}^{p}/C_{66}^{p}	1.25	1.02	1.20	1.14
C_{55}^{p}/C_{66}^{p}	1.06	1.08	1.05	1.02

Table 4.20. Principal stiffness direction of stereom type 5. $\mathbf{n}_1$: direction of max-imum longitudinal stiffness, n3: direction of minimum longitudinal stiffness, $\mathbf{n}_2 = \mathbf{n}_3 \times \mathbf{n}_1$: direction of intermediate longitudinal stiffness.

	stereom 5			
	RVE 1	RVE 2	RVE 3	RVE 4
n_{1x}	-0.7112	0.0677	0.7112	0.3732
n_{1y}	0.4444	-0.9679	-0.4619	-0.9237
n_{1z}	-0.5446	-0.2419	0.5299	-0.0872
n_{2x}	-0.0009	-0.7300	0.0586	-0.8409
n_{2y}	0.7742	-0.2133	0.7902	-0.2971
n_{2z}	0.6330	0.6493	0.6100	-0.4523
n_{3x}	0.7030	0.6800	0.7005	-0.3918
n_{3y}	0.4507	-0.1327	0.4028	-0.2421
n_{3z}	-0.5502	0.7211	-0.5891	0.8876

4.3.4 Stereom 6: the perforate high-density stereom at the plate basal zone

Stereom 6 corresponds to the high-density microstructure characterizing the basal plate zone, consisting of a trabecular system with a low number of elements per unit volume and long and thick trabeculae (Fig. 4.4). As shown in figure 4.9A, stereom 6 has a distinctive dense structure that appears to be divided into two different geometric layers: a palisade-like layer at the top (p1) and a tortuous layer at the bottom (p2). Smith (1980) classified these layers as a perforated over a labyrinthic microstructure. Nonetheless, this

labyrinth is noticeably different from the one located at the tubercle center (stereom 4).

The FEA results showed that this stereom is characterized by a relatively high stiffness and the ratios C_{11}^{p}/C_{22}^{p} and C_{11}^{p}/C_{33}^{p} showed the slight stiffness specialization of this microstructure. This is confirmed by the slightly elongated surface representing the directional dependence of longitudinal stiffness, see, e.g., Figure 4.6(e). It's worth noting that RVE 4 exhibited a higher stiffness specialization compared to the other RVEs. In this instance, the ratios C_{11}^{p}/C_{22}^{p} and C_{11}^{p}/C_{33}^{p} reached 1.30 and 1.41, respectively, which are significantly higher than the corresponding ratios computed for the other microstructures, averaging at 1.06 and 1.12. Such difference in stiffness specialization does not correspond to a significant variation in the orientation of the axes of maximum and minimum longitudinal stiffness. Actually, the direction of maximum longitudinal stiffness, namely $\mathbf{n}_1$, is parallel to y for all RVEs, while the minimum longitudinal stiffness $\mathbf{n}_3$ typically aligns with the *z*−*x* plane, albeit with slight variations in orientation among the four RVEs. The distinct orientation of $\mathbf{n}_3$ is likely associated with the location of each specific RVE within the plate. RVE 1 and 4, extracted near the plate center, exhibit n3 almost parallel to the z-axis, whereas RVE 2 and 3 have $\mathbf{n}_3$ inclined within the *z* − *x* plane.

Interestingly, the orientation of the axes of maximum longitudinal stiffness, always parallel to y, appears to contrast with the orientation of the palisade-like structures mentioned earlier, which align along the *z*-axis

Table 4.21. Stiffness tensor principal components C_{ij}^{p} for stereom type 6.

	stereom 6			
	RVE 1	RVE 2	RVE 3	RVE 4
C_{11}^{p} (MPa)	38369	40392	42495	29515
C_{22}^{p} (MPa)	36836	38181	40052	27207
C_{33}^{p} (MPa)	34274	35904	38089	20919
C_{12}^{p} (MPa)	16243	17010	17823	11310
C_{13}^{p} (MPa)	15372	16682	17792	9677
C_{23}^{p} (MPa)	14839	15241	16467	9708
C_{14}^{p} (MPa)	-6	-3	-6	-1
C_{15}^{p} (MPa)	3	-1	-8	29
C_{16}^{p} (MPa)	237	-132	-68	-153
C_{24}^{p} (MPa)	-55	-145	-144	-17
C_{25}^{p} (MPa)	185	15	-38	-15
C_{26}^{p} (MPa)	-5	21	-1	-4
C_{34}^{p} (MPa)	-159	19	-89	40
C_{35}^{p} (MPa)	405	-203	60	-132
C_{36}^{p} (MPa)	380	-40	-357	-428
C_{44}^{p} (MPa)	10710	11220	11447	8408
C_{55}^{p} (MPa)	10482	11216	11576	7664
C_{66}^{p} (MPa)	10152	10244	10789	7822
C_{45}^{p} (MPa)	-12	60	-202	-35
C_{46}^{p} (MPa)	22	24	-45	27
C_{56}^{p} (MPa)	-66	31	-75	32

Table 4.22. Values of the ratio C_{ij}^{p}/C_{pq}^{p} between the stiffness tensor principal components for stereom type 6.

	stereom 6			
	RVE 1	RVE 2	RVE 3	RVE 4
C_{11}^{p}/C_{22}^{p}	1.04	1.06	1.06	1.08
C_{11}^{p}/C_{33}^{p}	1.12	1.13	1.12	1.41
C_{22}^{p}/C_{33}^{p}	1.07	1.06	1.05	1.30
C_{12}^{p}/C_{13}^{p}	1.06	1.02	1.00	1.17
C_{12}^{p}/C_{23}^{p}	1.09	1.12	1.08	1.16
C_{13}^{p}/C_{23}^{p}	1.04	1.09	1.08	1.00
C_{44}^{p}/C_{55}^{p}	1.02	1.00	0.99	1.10
C_{44}^{p}/C_{66}^{p}	1.06	1.10	1.06	1.08
C_{55}^{p}/C_{66}^{p}	1.03	1.09	1.07	0.98

Table 4.23. Principal stiffness direction of stereom type 6. $\mathbf{n}_1$: direction of max-imum longitudinal stiffness, n3: direction of minimum longitudinal stiffness, $\mathbf{n}_2 = \mathbf{n}_3 \times \mathbf{n}_1$: direction of intermediate longitudinal stiffness.

	stereom 6			
	RVE 1	RVE 2	RVE 3	RVE 4
n_{1x}	0.0871	-0.0349	-0.0698	-0.0520
n_{1y}	0.9956	0.9994	0.9976	0.9932
n_{1z}	-0.0349	0.0000	0.0000	0.1045
n_{2x}	0.9372	0.7981	0.6803	0.9944
n_{2y}	-0.0700	0.0279	0.0476	0.0612
n_{2z}	0.3418	0.6018	0.7314	-0.0867
n_{3x}	-0.3379	-0.6014	-0.7296	0.0925
n_{3y}	0.0625	-0.0210	-0.0510	-0.0994
n_{3z}	0.9391	0.7986	0.6820	0.9907

4.4 A reformulated skeletal model for the *Paracentrotus Lividus* interambulacral plates

The overall results obtained in this study enabled the identification and characterization of the unique 3D variability of the echinoid stereom in terms of trabecular configuration and averaged elastic properties. By comparing these results with the outcomes of the 2D investigations (A. B. Smith, 1980), (V. Perricone et al.,2023), additional key structural details can be identified and included in a reformulated skeletal model of the *Paracentrotus lividus* inter-ambulacral plates as shown in Figure 4.7 (B). Proposed model includes the distinction between the galleried stereom 2 and 3, resulting in a non-uniform galleried stereom present at the plate suture region, and the recognition of the stereom 5 as an inclined galleried microstructure pertaining to a region of transition between the labirinthic and the galleried microstructures present at the plate center, beneath the tubercle.

Key differences with respect to the previous literature can be identified in the values of the stiffness between the 2D and 3D analyses (V. Perricone et al.,2023), e.g., the galleried stereom in the 2D model is more rigid than the 3D cubes. Hence, even if the 2D analysis can provide some structural aspects, a 3D investigation is necessary to understand the effective elastic behavior of these micro-

architectures. As in the 2D description (V. Perricone et al.,2023), the specific modulations of the material properties and 3D architecture can be associated to specific mechanical needs, which have been hypothesized and described in several studies regarding echinoid plates and other skeletal elements (V. Perricone et al.,2023), (H.-U. Nissen, 1969), (M. Telford, 1985), (A. B. Smith, 1980), (M. Jensen, 1972), (T. B. Grun, 2018). Regarding the elastic constants, the achieved results not only provide a useful insight about the anisotropic or isotropic mechanical behavior of the stereoms, but also offer important information concerning the nature and direction of the forces operating on them and the entire plate. Specifically, the segmentation of the entire plate into distinct orientation of the axes of maximum and minimum longitudinal stereomic stiffness, which are shown in Figure 4.8, is likely related to the principal stress directions within the plates from the spines, along with the direction of the collagen fibers and their stereomic insertion. According to the proposed skeletal model for the *Paracentrotus Lividus* inter-ambulacral plates, shown Figure 4.7 (B), the stereom is characterized by high density imperforated microstructure present at the tubercle top, which is likely subjected to stress concentrations induced by the spine action. At the tubercle boss, the stereom is specialized in a high anisotropic galleried configuration, which is able to transfer directional stresses of the catch apparatus fibres inserted along the galleries connecting the spine with the tubercle. The center of the tubercle presents a less stiff, isotropic labyrinthic stereom with non-oriented trabeculae. Its presence is presumably due to lower stress values having principal directions without any specific orientation. This conjecture is supported by the presence of a very coarse and open structure at the boss centre. Below the tubercle, a transition region connects the labirithic microstructure with anisotropic galleried stereoms that, with varying orientation, depart from the centre and directionally distribute the applied stresses towards the suture areas, where the stresses become parallel to the plate mid-plane. The peculiar mechanical behaviour of sutures (F. Marmo et al., 2022) influences the stress distribution far from the plate center, confirming the alignment between the principal stress directions and the microstructure orientation near the plate edges. Finally, a highly thick and stiff perforate stereom is present in the basal region, indicating that here the plate is subjected to stress concentrations.

4.5 Conclusion

In conclusion, this study has provided a comprehensive exploration of the microstructural variations and mechanical behaviors of the inter-ambulacral plates in *Paracentrotus Lividus* using advanced 3D imaging and finite element analysis (FEA). Building upon earlier 2D investigations, the research elucidated distinct stereom types within the plates, each exhibiting unique trabecular configurations and elastic properties. The findings underscore significant differences in mechanical behavior among stereom types, particularly highlighting the directional specialization and anisotropic nature of the galleried stereom at the tubercle boss. This specialized structure, crucial for attachment sites of spine-related fibers, demonstrates robustness against directional stresses, enhancing fracture resistance and energy dissipation capabilities.

Moreover, the study identified nuanced structural adaptations across different regions of the plate, such as the labyrinthic stereom at the tubercle center and the perforated stereom at the basal zone, each tailored to specific mechanical demands. These insights not only contribute to our understanding of *Paracentrotus Lividus* skeletal architecture but also offer potential inspirations for biomimetic applications in material science. By mimicking the natural strategies of echinoids in creating graded porous structures, future developments could lead to innovative designs of adaptive, lightweight, and resilient materials capable of withstanding diverse internal and external forces across various technological domains.

Overall, this investigation underscores the importance of 3D analyses in capturing the true complexity and mechanical functionality of biological structures, surpassing the limitations of traditional 2D approaches. It lays the groundwork for further studies aimed at unravelling the dynamic interplay between structure and function in echinoderm skeletal systems, with potential implications for advancing bioinspired materials and engineering solutions

Note

This chapter has submitted as: Perricone, V., Cesarano, P., Deb, M., Lublin, D., Mutalipassi, M., Pappalardo, L., ... & Marmo, F. Microarchitectural Design Variation of the Echinoid Skeleton: A 3D Structural and Mechanical Study of *Paracentrotud Lividus*. *Available at SSRN 4846809.*

Chapter 5

The echinoid plate: microstructural variation in relation to the main sustained mechanical stresses

In this Chapter, investigation the mechanical behaviour of the overall plate of *Paracentrotus Lividus* is reported to understand if the stereom variability responds to species-specific strategies to increase both lightness and resistance. For this purpose, a digital model of the echinoid plate was generated and analyzed using a Finite Element Analysis.

5.1 Mechanical interpretation hypothesis

The echinoid skeletal pattern within the plate resembles the trabecular architecture of vertebrate bones, which has been reconstructed and analysed by numerous biomechanical studies (e.g., Buckwalter and Cooper, 1987; Weiner and Wagner, 1998; Muller, 2009; Ruffoni and Van Lenthe, 2017). In these multiple analyses, bone has been identified as optimally structured apropos its load-bearing function, as well as, specifically guided and maintained during its development and formation by mechanical forces (Wolff's Law). Interestingly, historical studies assessed that the trabecular architecture of the proximal femur perfectly matches principal stress trajectory patterns, calculated using the 'Graphical Statics' theory (Von Meyer, 1867) (Fig.5.1). This configuration corresponds to a mechanically optimized structure ensuring maximal strength and minimal weight.

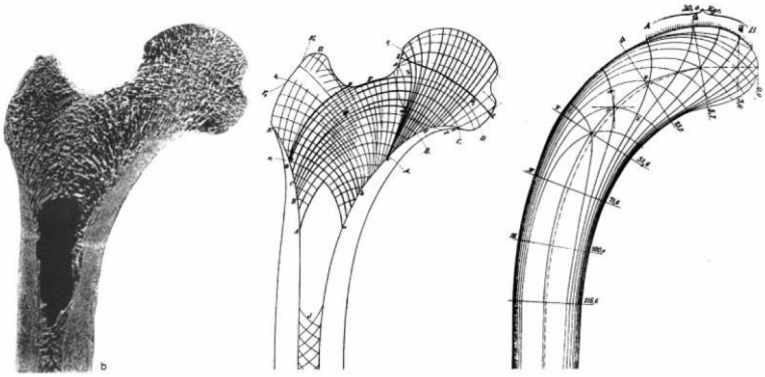

Figure 5.1. Illustration of the Wolff's trajectorial theory. On the left, a mid-frontal section of the proximal femur can be seen displaying a trabecular architecture; the middle illustration shows Von Meyer's schematic drawing (1967); stress trajectories in a model analysed by Culmann (1864;1875) using graphical statics can be viewed on the right. (Adapted from Wolff, 1986).

Based on this detailed knowledge regarding bone trabecular architecture and its mechanical meaning, a hypothesis was formulated stating that the plate stereom structure could be described through the relationship between form and function, produced and maintained by mechanical forces acting on the plate. In this perspective, the echinoid plate structure would similarly correspond to the diagram of the main stress trajectory as seen in vertebrate bones. In this respect, the skeletal plates are mainly influenced by the attached spines that determine a series of tensile and compression stresses. Spines perform different functions, such as locomotion, burrowing, protection (from physical trauma and predators), and stress impact reducer in the prevention of structural test damage; thus, its microstructure pattern could be the resulting optimized architecture. Moreover, different isotropic and anisotropic stereom types could influence stress directions and until today no studies have explored this possible effect.

To assess this hypothesis, a 3D reconstruction of the *Paracentrotus Lividus* plate and its material variability were carried out to analyses the actions of the main mechanical stresses by using Finite Element Analysis (FEA). In this manner, the microstructural variation of the plate was described and compared with the main stress trajectories generated by the stress of spine action through the application of a normal load on the tubercle

5.2 Materials and methods

5.2.1 Photogrammetry

To obtain the overall geometry of a real plate and reconstruct a geometric 3D model to be analyzed by the Finite Element Method, an intact interambulacral plate from a *P.Lividus* test was photographed using a Panasonic Lumix FZ1000 digital camera from a lateral, top and bottom perspective while rotating the sample on a support plane (Fig. 5.2A). To perform this, the camera was mounted on a tripod, with the optical axis orthogonal to the support plane of the plate, at a fixed distance of approximately 100 mm from the sample. The digital photographs, 403 in total, included a 1 mm scale for calibration. They were subsequently uploaded to a personal computer and measured using ImageJ®. Lastly, the photographs were used to reconstruct a three-dimensional (3D) geometric model of the plate using a photogrammetric reconstruction using Agisoft PhotoScan® software (Fig. 5.2B).

In order to calibrate the 3D model, the *P.lividus* plate was manually measured with a calibre obtaining length, width and thickness. The plate thickness was estimated to be about 1mm.

5.2.2 Finite Element Analysis

The plate geometry obtained from the photogrammetric acquisition was regularized by employing a parametrized description of the plate. The regularized 3D plate model was incorporated in the center of a consecutively reconstructed multiplate model replicating part of the echinoid test. This configuration allowed efficient analysis of the centre positioned plate using FEM, while constraining the entire model to the surrounding external plates. In this way, the displacement constraints (necessary to anchor the model ensuring its equilibrium and preventing movement while loaded) do not affect the plate analysis avoiding concentrated reactions at supports that could influence stress directions. Kinematic coupling constraints were applied to model the plate suture and prevent sliding at the interfaces between adjacent plate surfaces. Specifically, for each interface, these constraints eliminated the degrees of freedom in the radial and circumferential

directions using a user-defined cylindrical coordinate system at the coupling nodes. In contrast, the orthogonal direction was governed by a Coulomb-type contact with a friction coefficient of 2.

To investigate the effect of the microstructure variability, two different cases were analyzed:

1) Model n.1. homogeneous isotropic material distribution with Young's modulus of 73.5 GPa (Figure 5.2D, model 1)

2) Model n.2. anisotropic materials distributed according to the microstructure variability described in chapters 2 and 3. In particular, oriented suture galleried and tubercle galleried structures were considered anisotropic, whereas non-oriented labyrinthic and perforated structures were considered isotropic (Figure 5.2D, model 2 and Figure 5.3)

The 3D model surfaces were meshed by employing tetrahedral linear finite elements. For model 2, parabolic tetrahedral elements were also used to further highlight the effect of the material difference on the maximum and minimum main stress directions within the plate. The material properties of the plate of model n.2 were assigned based on results obtained from FE Analysis described in Chapter 4.

The models were subjected to compression stresses of spine action computed for a resultant force of 2N at the principal tubercle apex. Based on the negative echinoid coelomic pressure of –8 Pa reported by Ellers and Telford (1992), a uniformly distributed pressure of 8e-06 MPa was applied to the different model surfaces

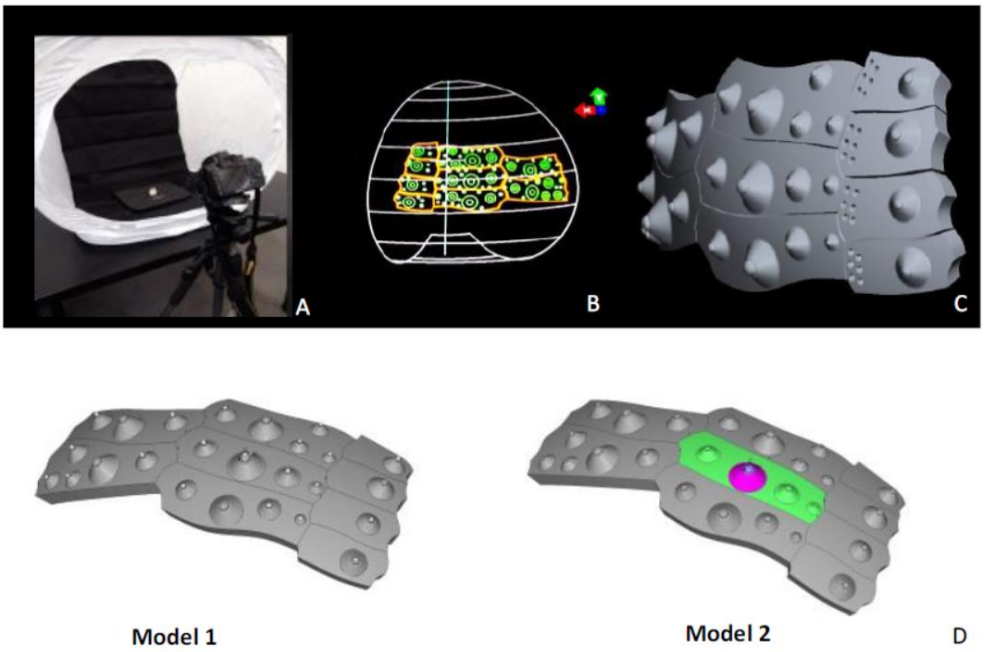

Figure 5.2. *Geometry acquisition and 3D plate model reconstruction*. A) Photogrammetry; B) and C) Plate model reconstruction, D) Model 1 and Model 2 differentiation based on microstructure variability

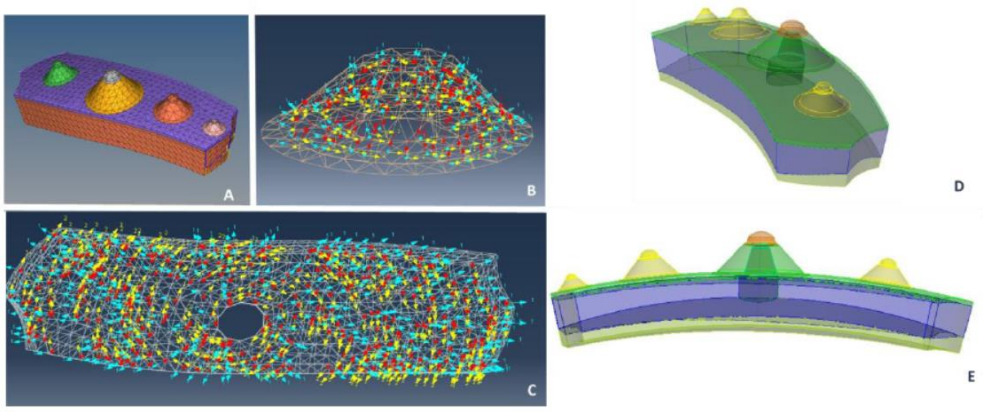

Figure 5.3. *Model 2 and material differentiation*. A) Mesh; B) and C) material orientation, D) and E) material differentiation

5.3 Results

The minimum principal stress (as compressive stress direction) and maximal principal stress (as tensile stress direction) results were reported in Figures 5.4 and 5.5 for both the transversal and longitudinal sections using a chromatic scale.

Figure 5.4 shows how the minimum principal stress departing from the tubercle was radially distributed and extended to the lateral regions with directions parallel to the surface. In model 2, these vectors were deviated with respect to model 1, indicating a material differentiation influence. In particular, the stress assumed directions parallel to the surface and formed an evident arc in the basal zone, which redistributed stress directly into the suture. The use of parabolic elements further highlighted this deviation, both in the transversal and longitudinal sections.

Figure 5.5 demonstrates that the maximum principal stress in model 1 possesses circular directions, which in model 2 deviated towards a closer parallel alignment. Between these two models, there is also a significant difference in stress values. Moreover, both models present a high tensional state in the basal zone. Similarly, to the previous case, the use of parabolic elements further highlighted this deviation.

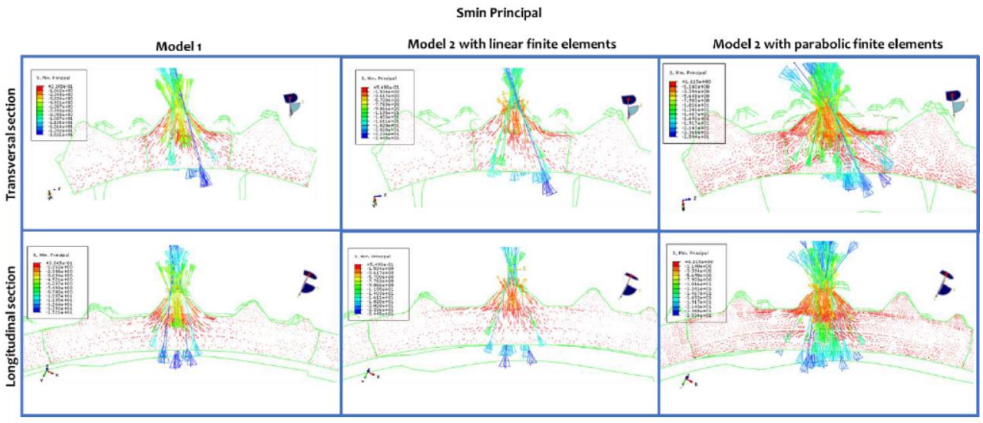

Figure 5.4. *Minimal principal stress of P.Lividus* interambulacral plate. Results of FEA simulating a distributed normal load on the mamelon displayed in an ascending order using a chromatic scale from blue to red.

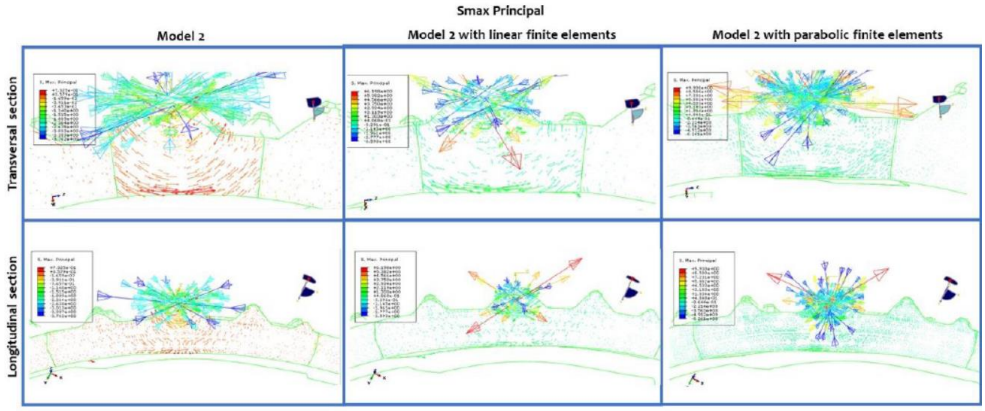

Figure 5.5. *Maximum principal stress in the P. Lividus* interambulacral plate. FEA simulating a distributed normal load on the mamelon. Results are displayed in an ascending value using a chromatic scale from blue to red.

5.4 Discussion

In nature, forms and structures generally adapt to a minimum use of energy and material for their construction and maintenance, as well as, to ensure sufficient resistance to withstand mechanical forces. Accordingly, D'Arcy Thompson (1917) described how organismal forms can be considered as a diagram of forces. The study carried out in this paper confirms that the echinoid skeletal architecture can be described as a diagram of multiple force actions. The echinoid skeletal material is highly variable in density and microarchitecture because of the remarkable plasticity of the skeletal tissue. The possible architectural modulations in relation to specific mechanical needs have been hypothesized and described in several studies regarding echinoid plates and other skeletal elements (Raup, 1966; Nissen, 1969; Jensen, 1972; Regis, 1977; Smith, 1980; Telford, 1985a, b); however, presently, no study has neither explored nor demonstrated in detail its correlation with principal stresses and stress deviation related to material differentiation. FEA results showed that the microstructure variability within the plate could be explained by a similar Wolff's trajectorial hypothesis for vertebrate bones and that material differentiation itself influences the stress direction. In fact, the orientations of the trabecular architecture correspond with those of the

principal stresses and consequently with the main stress trajectories. Accordingly, the structural pattern showed a specific correlation to the mechanical needs of the skeletal areas. In the area subjected to high compressive stress, as in the mamelon zone, the skeletal material increases in density specializing in an imperforated stereom, whereas it specializes in the galleried stereom within the margins following the main stress trajectories. The plate's centre seems to be subjected to multiple directional stress that are confronted by uniformly long and thick non- oriented trabeculae of the labyrinthic stereom. Contrarily, a perforated stereom was employed in the basal area, which for the first time was demonstrated to be subjected to high traction states; in this case a functional increase in density was needed to reinforce the structure.

The difference between the two FEM models indicated a direct influence of the material differentiation on stress redistribution within the plate. The stresses were distributed paralleled to the surface flowing to the lateral areas and directly into the sutures that were characterized by soft collagenous ligaments and could presumably act as stress dissipators.

This study demonstrated that the echinoid microstructural variability represents a functional mechanical adaptation of the skeleton. The use of stereom types, differentiated based on predicted stress trajectories, represents a structural optimization for the increase of skeletal resistance and lightness. In this regard, the strategic density variation and directional response were necessary to increase structural strength and material saving.

5.5 Conclusion

This study confirms that the echinoid skeletal architecture can be effectively described as a diagram of multiple force actions, reinforcing D'Arcy Thompson's (1917) perspective on organismal forms as diagrams of forces. The echinoid skeletal material exhibits remarkable plasticity, resulting in high variability in density and microarchitecture tailored to specific mechanical needs. Our findings support the

hypothesis that material differentiation within the skeletal structure correlates with principal stresses and stress deviation.

Finite Element Analysis (FEA) results revealed that the microstructural variability within the echinoid plate aligns with Wolff's trajectorial hypothesis for vertebrate bones, indicating that material differentiation influences the stress direction. Specifically, the orientations of the trabecular architecture correspond with principal stress trajectories. High compressive stress areas, such as the mamelon zone, exhibit increased material density, forming an imperforated stereom. In contrast, galleried stereom is present in the margins following main stress trajectories, and uniformly long and thick non-oriented trabeculae of the labyrinthic stereom counteract multiple directional stress in the plate's center. Additionally, the basal area, subjected to high traction states, employs perforated stereom, reinforcing the structure through a functional increase in density.

The difference between the two FEM models highlighted the direct influence of material differentiation on stress redistribution within the plate. Stresses were distributed parallel to the surface, flowing into the lateral areas and sutures, which are characterized by soft collagenous ligaments acting as stress dissipators.

Overall, this study demonstrates that the echinoid microstructural variability represents a functional mechanical adaptation of the skeleton. The strategic use of differentiated stereom types based on predicted stress trajectories optimizes structural strength and lightness, achieving a balance between skeletal resistance and material efficiency.

Chapter 6

Conclusions and future perspectives

The aim of this thesis was to investigate the mechanical design of echinoids with the intention to acquire new biological insights and to identify strategies that can be abstracted and applied to the design of new bioinspired structures in building construction and materials.

In the field of building construction, lightweight and resistant shell structures can be designed by efficiently integrating and optimizing form, structure, and function to achieve the capability to bear a variety of loading conditions. The observation of the echinoid test and the direct analysis of its mechanical behaviour can lead to the abstraction of different functional principles that can be appliable to the designing of new shell structures able to efficiently withstand a large variety of loading conditions, as confirmed by previous studies (e.g., Marmo et al., 2022). The studies carried out in this thesis show that further interesting strategies can be identified by analysing the microscale architecture.

In nature, forms and structures generally adapt to a minimum use of energy and material for their construction and maintenance, as well as to ensure sufficient resistance to withstand mechanical forces. the different studies confirm this adaptation in the echinoid skeleton by revealing the unique specialization of its microarchitecture. The possible stereomic architectural modulations in relation to specific mechanical needs have been hypothesized and described in several studies regarding echinoid plates and other skeletal elements (D. Raup, 1966), (M. Jensen, 1972), (H.-U. Nissen, 1969), (A. B. Smith, 1980), (M. Telford, 1985), (D. A. van Egmond et al., 2021) such as at starfish (T. Yang et al., 2022). Contemporary research into stereom architectures continues to reveal new 3D geometrical and

compositional insights leading to superior mechanical performance, especially damage tolerance (T. Yang et al., 2022).

The achieved results regarding the material distribution, topology, geometry, and mechanical behavior variability are interesting, revisiting the available literature dating back over 44 years and providing key starting points for future biomechanics and biomimetic research.

In the literature, numerous examples demonstrate how the morphology of biomaterials can inspire innovative designs that align with the construction principles of natural organisms, while also incorporating structural optimization. One such example is the use of spinodal architected materials with tunable anisotropy in structural optimization. This approach mimics various microstructural characteristics observed in nature, directly targeting stiffness and lightweight design. Additionally, it indirectly enhances other mechanical and biological functions, which are supported by the spinodal porosity and randomness at the microscale (V. Fernando et al., 2022).

Several aspects of the echinoid stereom can be further investigated including the analysis fracture behaviour be as well as, the material properties, compositional and crystallographic characterizations of the different stereo types and their influence on the mechanical response. All these aspects are objects of current study by our team to better understand the meaning of this unique assemblage of ordered and disordered trabecular typologies. Ji et al. (2022) have reported the high fracture resistance and energy dissipation effects of the echinoid-ordered stereom structures. Conversely, a recent work revealed that a certain degree of disorder observed in numerous natural cellular materials can also lead to improved damage tolerance with respect to fully ordered ones (D. A. van Egmond, 2021). Echinoids seem to effectively combine both, presumably enabling a dynamic adaptation over space and time of skeletal trabecular templates and their material property distribution to the expected applied forces. Understanding this type of strategy can provide interesting suggestions for the development of graded porous ceramics with superior mechanical performances. Porous structures are of high interest in several fields, such as electronics, biology, chemistry, and energy; however, their application is often limited by

their mechanics which generally exhibit low damage tolerance and structural resistance. Hence, echinoids can represent a valid source of inspiration for the creation of adaptive, lightweight, and resistant structures to withstand internal and external forces.

As a future vision and innovation, lessons derived from the echinoid can be abstracted and translated into newly inspired designs that are increasingly like the construction law of these organisms. The morphogenetic logic of the echinoid skeleton can be translated into a computational flow design in which the choice between order or disorder architecture, as well as its composition, depends on the specific constraint of the materials, structure, shape, and applied loads. This vision can be thoroughly applied thanks to the digital revolution that now enables new design spaces and fabrication with a free formal expression. Digital modelling, analysis, and fabrication are now dissolving the dichotomy between form and matter allowing the development and controlled deposition of complex material with continuous hierarchical shapes and multiscale structures. This empower a new vision in which the “learning from nature” approach combined with nature-based materials and a coherent use of computational design and fabrication can be configured as a future line of human design able to imitate and integrate nature through multiple dimensions

Bibliography

Abou Chakra M, Stone JR. (2011), Holotestoid: a computational model for testing hypotheses about echinoid skeleton form and growth. J. Theor. Biol. 285, 113–125. (doi:10.1016/j.jtbi.2011.06.019)

Addadi L., S. Weiner, (1992), Control and design principles in biological mineralization, Angewandte Chemie International Edition in English 31 (2) 153–169.

Addadi L., S. Weiner, (2014), Biomineralization: mineral formation by organisms, Physica Scripta 89 (9) 098003.

Adriaenssens S, Block P, Veenendaal D, Williams C. (2014), Shell structures for architecture: form finding and optimization. Routledge.

Albéric M, Caspi EN, Bennet M, Ajili W, Nassif N, Azaïs T, ... Politi Y. (2018), Interplay between calcite, amorphous calcium carbonate, and intracrystalline organics in sea urchin skeletal elements. Cryst. Growth Des. 18, 2189-2201.

Albéric M, Stifler CA, Zou Z, Sun CY, Killian CE, Valencia S, ... Politi Y. (2019), Growth and regrowth of adult sea urchin spines involve hydrated and anhydrous amorphous calcium carbonate precursors. J. Struct. Biol.: X. 1,100004.

Allasinaz A. (1995), Paleontologia generale e sistematica degli invertebrati. Genova, Italy: ECIG.

Allwood J. M., J. M. Cullen, M. A. Carruth, D. R. Cooper, M. McBrien, R. L. Milford, M. C. Moynihan, A. C. Patel, Allwood Sustainable materials: with both eyes open, Vol. 2012, UIT Cambridge Limited Cambridge, UK.

Ameye L, Hermann R, Killian C, Wilt F, Dubois P. (1999), Ultrastructural localization of proteins involved in sea urchin biomineralization. J. Histochem. Cytochem. 47,1189-1200.

Barthelat F., (2007), Biomimetics for next generation materials, Philosophical Transactions of the Royal Society A: Mathematical, Physical and Engineering Sciences 365 (1861),2907–2919.

Barthelat F., (2015), Architectured materials in engineering and biology: fabrication, structure, mechanics and performance, International Materials Reviews 60 (8), 413–430.

Benyus J. M., et al., (1997), Biomimicry: Innovation inspired by nature.

Bower A. F., (2009), Applied mechanics of solids, CRC press.

Brusca RC, Brusca GJ. 2002), Invertebrates. Basingstoke,UK: Sinauer Associate Incorporated.

Carnevali M. D. C., F. Bonasoro, G. Melone, (1991), Microstructure and mechanical design in the lantern ossicles of the regular sea-urchin Paracentrotus Lividus a scanning electron microscope study, Italian Journal of Zoology 58 (1) 1–42.

Cavey MJ, Märkel K. (1994), Echinodermata. In Microscopic Anatomy of Invertebrates (ed FW Harrison), pp. 345-400. New York: Wiley.

Chen TT. (2011), Microstructure and micromechanics of the sea urchin Colobocentrotus atratus, Thesis, Massachusetts Institute of Technology, MA.

Currey JD. (1999), The design of mineralized hard tissues for their mechanical function. J. Exp. Biol. 202, 3285-3294

Dafni J. (1986), A biomechanical model for the morphogenesis of regular echinoid tests. Paleobiology, 12, 143-160.

De Castillo J, Smith DS, Vidal AM, Sierra C. (1995), Catch in the primary spines of the sea urchin Eucidaris tribuloides: a brief review and a new interpretation. Biol. Bull. 188, 120–127.

Ellers O, Johnson AS, Moberg PE. (1998), Structural strengthening of urchin skeletons by collagenous sutural ligaments. Biol. Bull. 195, 136-144. (doi:10.2307/1542821).

Ellers O, Telford M. (1992), Causes and consequences of fluctuating coelomic pressure in sea urchins. Biol. Bull. 182, 424–434. (doi:10.2307/1542262)

Fayemi PE, Wanieck K, Zollfrank C, Maranzana N, Aoussat A. (2017), Biomimetics: process, tools and practice. Bioinspir. Biomim. 12(1), 011002.

Fazekas, A., Dendievel, R., Salvo, L., & Bréchet, Y. (2002), Effect of microstructural topology upon the stiffness and strength of 2D cellular structures. International Journal of Mechanical Sciences, 44(10), 2047-2066.

Fernandez C, Boudouresque CF. (1997), Phenotypic plasticity of Paracentrotus lividus (Echinodermata: Echinoidea) in a lagoonal environment. Marine Ecology Progress Series, 152, 145-154.

Fernandez C, Caltagirone A. (1994), Growth rate of adult sea urchins, Paracentrotus lividus in a lagoon environment: The effect of different diet types. In: David B, Guille A, Fe´ral JP, Roux M (eds) Echinoderms through time. AA Balkema Press, Rotterdam, pp 655–660

Fernandez, C., (1996), Croissance et nutrition de Paracentrotus lividus dans le cadre d'un projet aquacole avec alimentation artificielle. These de doctorat, Universite de Corse, 278 pp.

Fernando V. Senhora, Emily D. Sanders, and Glaucio H. Paulino, (2022), Optimally-Tailored Spinodal Architected Materials for Multiscale Design and Manufacturing. Advanced Materials.

Fratzl P., (2007), Biomimetic materials research: what can we really learn from nature's structural materials?, Journal of the Royal Society Interface 4 (15) 637–642.

Fratzl P., R. Weinkamer, (2007), Nature's hierarchical materials, Progress in materials Science 52 (8) 1263–1334.

Fratzl P, Kolednik O, Fischer FD, Dean MN. (2016). The mechanics of tessellations–bioinspired strategies for fracture resistance. Chem. Soc. Rev. 45, 252–267. (doi:10.1039/c5cs00598a).

Gamble JC. (1965), Some observations on the behaviour of two regular echinoids. In Symposium Underwater Association. Underwater Ass., Malta (pp. 47-50).

Gorzelak P. (2021), Functional Micromorphology of the Echinoderm Skeleton. Cambridge University Press.

Grossmann JN, Nebelsick JH. (2013), Stereom differentiation in spines of Plococidaris verticillata, Heterocentrotus mammillatus and other regular sea urchins. In Echinoderms in a changing world (ed C. Johnson), pp 97–104. London,UK: Taylor & Francis

Grossmann J. N., J. H. Nebelsick, (2013), Comparative morphological and structural analysis of selected cidaroid and camarodont sea urchin spines, Zoomorphology 132 301–315.

Grun T. B., Von Scheven M, Bischoff M, Nebelsick JH., (2018), Structural stress response of segmented natural shells: a numerical case study on the clypeasteroid echinoid Echinocyamus pusillus. J. R. Soc. Interface 15, 20180164.

Grun T. B., Nebelsick JH., (2018), Structural design of the minute clypeasteroid echinoid Echinocyamus pusillus. R. Soc. Open Sci. 5, 171323.

Grun T. B., Nebelsick JH., (2018), Structural design of the echinoid's trabecular system. PLoS One 13 (9), e0204432.

Grun TB, Nebelsick JH. (2018) Technical biology of the clypeasteroid echinoid Echinocyamus pusillus: a review. C. T. Geo. 7, 247–254. (doi:10.2478/ctg-2018-0017)

Hammer Ø, Harper DA, Ryan PD. (2001), PAST: Paleontological statistics software package for education and data analysis. Palaeontol. Electron. 4, 9.

Hidaka M., Takahashi K. (1983), Fine structure and mechanical properties of the catch apparatus of the sea-urchin spine, a collagenous connective tissue with muscle-like holding capacity. J. Exp. Biol. 103, 1-14.

Huang W., D. Restrepo, J.-Y. Jung, F. Y. Su, Z. Liu, R. O. Ritchie, J. McKittrick, P. Zavattieri, D. Kisailus, (2019), Multiscale toughening mecha-nisms in biological materials and bioinspired designs, Advanced Materials 31 (43), 1901561.

Ibidapo-Obe O, Royles R, Sofoluwe AB. (1981), Echinodome: some approaches to the analysis of the drop-shaped tank. Mech. Res. Commun. 8, 47-54.

Jensen M., (1972), The ultrastructure of the echinoid skeleton. Sarsia 48, 39-48

Ji HM, Qi QJ, Liang SM, Yu H, Li XW. (2022), Ordered stereom structure in sea urchin tubercles: High capability for energy dissipation. Acta Biomaterialia. 150, 310-323.

Kawaguti S., Y. Kamishima, (1965), Electron microscopy on the spine muscle of the echinoid, Biol. J. Okayama Univ. 11 31–40.

Killian CE et al. (2009), Mechanism of calcite co-orientation in the sea urchin tooth. J. Am. Chem. Soc. 131, 18404-18409.

Killian CE et al. (2011), Self-Sharpening Mechanism of the Sea Urchin Tooth. Adv. Funct. Mater. 21, 682-690.

Killian CE, Wilt FH. (2008), Molecular aspects of Biomineralization of the echinoderm endoskeleton. Chem Rev 108:4463-4474.

Lechnickij S. G., (1981) Theory of elasticity of an anisotropic body, Mir Publ.

Knippers J, Menges A, Gabler M, La Magna R, Waimer F, Reichert S, Schwinn T. (2013), From nature to fabrication: biomimetic design principles for the production of complex spatial structures. In Advances

in architectural geometry (eds. L Hesselgren, S. Sharma, J Wallner, N Baldassini, P Bompas, J Raynaud), pp 107–122. Wien: Springer.

Knippers J, Nickel KG, Speck T. (2016), Biomimetic Research for Architecture and Building Construction. Switzerland: Springer International Publishing.

Knippers J, Schmid U,Speck T. (2019), Biomimetics for architecture: learning from nature. Birkhäuser.

Knippers J, Speck T. (2012), Design and construction principles in nature and architecture Bioinspir. Biomim. 7015002.

Krauss S, Monsonego-Ornan E, Zelser E, Fratzl P, Shahar R. (2009), Mechanical function of a complex three-dimensional suture joining thebony elements in the shell of the redearedslider turtle. Adv. Mater. 21, 407–412. (doi:10.1002/adma.200801256)

Kroh A, Mooi R. World Echinoidea Database. Paracentrotus lividus (Lamarck, 1816). (2020), Accessed through: World Register of Marine Species at: http://www.marinespecies.org/aphia. php?p=taxdetails&id=124316 on 23 September 2020.

Lee T.-C. Lee, R. L. Kashyap, C.-N. Chu, (1994), Building skeleton models via 3-d medial surface axis thinning algorithms, CVGIP: Graphical Models and Image Processing 56 (6) 462–478.

Mancosu A, Nebelsick, JH. (2020), Tracking biases in the regular echinoid fossil record: the case of Paracentrotus lividus in recent and fossil shallow-water, high-energy environments. Palaeontol. Electron. 23, 1-35.

Marmo F, Perricone V, Cutolo A, Candia Carnevali, Langella C, Rosati L. (2022), Flexible sutures reduce bending moments in shells: from the echinoid test to tessellated shell structures. R. Soc. Open Sci. 9, 211972.

Marmo F, Perricone V, Langella C, Pontillo G, Rosati L. (2019), Bioinspired design of shell structures: a lesson from echinoids. In Proceedings of IASS Annual Symposia. International Association for Shell and Spatial Structures (IASS). pp. 1-7

Marmo F, Rosati L. (2017), Reformulation and extension of the thrust network analysis. Computers & Structures, 182:104-118.

Meyers M. A., P.-Y. Chen, A. Y.-M. Lin, Y. Seki, (2008), Biological materials: Structure and mechanical properties, Progress in materials science 53 (1) 1–206.

Michiels T, Adriaenssens S, Dejong MM. (2019). Form finding of corrugated shell structures for seismic design and validation using non-linear pushover analysis. Engin. Struct. 181, 362–373. (doi:10.1016/j.engstruct.2018.12.043).

Mongiardino Koch N, Coppard SE, Lessios HA, Briggs DE, Mooi R, Rouse GW. (2018), A phylogenomic resolution of the sea urchin tree of life. BMC Evol. Biol. 18, 1-18.

Moss ML, Meehan MM. (1967), Sutural connective tissues in the test of an echinoid Arbacia punctulata. Acta Anat. 66, 279–304.

Moureaux C., A. Perez-Huerta, P. Comp`ere, W. Zhu, T. Leloup, M. Cusack, P. Dubois, (2010), Structure, composition and mechanical relations to function in sea urchin spine, Journal of structural biology 170 (1) 41–49.

Müter D, Sørensen HO, Oddershede J, Dalby KN, Stipp SLS. (2015), Microstructure and micromechanics of the heart urchin test from X-ray tomography. Acta Biomater. 23, 21-26.

Nebelsick JH, Dynowski JF, Grossmann JN, Tötzke C. (2015), Echinoderms: hierarchically organized light weight skeletons. In Evolution of lightweight structures, pp. 141-155. Dordrecht, Netherlands: Springer.

Nichols D, Currey JD. (1968), The secretion, structure, and strength of echinoderm calcite. In Cell Structures and its Interpretation, pp 251-261. London, UK: Edward Arnold.

Nickel KG, Klang K, Lauer C, Buck G. (2018), Sea urchin spines as role models for biologic design and integrative structures. In Highlights of applied mineralogy, pp. 1-14. Berlin,Germany: Walter de Gruyter GmbH & Co KG.

Nissen HU. (1969), Crystal orientation and plate structure in echinoid skeletal units. Science 166, 1150-1152

Oaki Y, Imai H. (2006), Nanoengineering in echinoderms: the emergence of morphology from nanobricks. Small 2, 66-70

Pearse JS, Pearse VB. (1975), Growth zones in the echinoid skeleton. Am Zool. 15, 731-751.

Perricone V, Grun T, Marmo F, Langella C, Candia Carnevali MD. (2020), Constructional design of echinoid endoskeleton: main structural components and their potential for biomimetic applications. Bioinspiration & Biomimetics. 16, 011001.

Perricone V, Grun TB, Rendina F, Marmo F, Candia Carnevali MD, Kowalewski M, ... Micheletti A. (2022), Hexagonal Voronoi pattern detected in the microstructural design of the echinoid skeleton. J. R. Soc. Interface 19, 20220226.

Perricone V., C. Langella, C. Santulli, (2022), Sustainable biomimetics: A discussion on differences in scale, complexity, and organization between the natural and artificial world, in: Bionics and Sustainable Design, Springer, pp. 171–193.

Perricone V., P. Cesarano, A. Mancosu, D. Asnicar, S. Bravi, F. Marmo, (2023), Echinoid skeleton: an insight on the species-specific pattern of the Paracentrotus Lividus plate and its microstructural variability, Journal of the Royal Society Interface 20 (199) 20220673.

Philippi U, Nachtigall W. (1996), Functional morphology of regular echinoid tests (Echinodermata, Echinoida): a finite element study. Zoomorphology 116, 35–50. (doi:10. 1007/BF02526927).

Presser V, Schultheiß S, Berthold C, Nickel KG. (2009) Sea urchin spines as a model-system for permeable, light-weight ceramics with graceful failure behaviour. Part I. Mechanical behaviour of sea urchin spines under compression. J. Bionic. Eng. 6, 203–213.

Presser V, Schultheiß S, Kohler C, Berthold C, Nickel KG, Vohrer A, Stegmaier T. (2011), Lessons from nature for the construction of ceramic cellular materials for superior energy absorption. Adv. Eng. Mater. 13, 1042-1049

Raup DM. (1966). The endoskeleton. In Physiology of Echinodermata, pp. 379-395. New York,USA: John Wiley & Sons.

Regis MB. (1977), Organisation microstructurale du stereome de l'Echinoide Paracentrotus lividus (Lamarck) et ses eventuelles incidences physiologiques. C. R. Acad. Sei. Paris 285,189-192.

Sarikaya M., (1999), Biomimetics: materials fabrication through biology, Proceedings of the National Academy of Sciences 96 (25) 14183–14185.

Seilacher A, Gishlick AD. (2014), Morphodynamics. Boca Raton, FL: CRC Press.

Seilacher A. (1979), Constructional morphology of sand dollars. Paleobiology 5, 191–221. (doi:10. 1017/S0094837300006527)

Seto J., Y. Ma, S. A. Davis, F. Meldrum, A. Gourrier, Y.-Y. Kim, U. Schilde, M. Sztucki, M. Burghammer, S. Maltsev, et al., (2012), Structure-

property relationships of a biological mesocrystal in the adult sea urchin spine, Proceedings of the National Academy of Sciences 109 (10) 3699–3704.

Silva M. J., Gibson L. J., (1997), The effect of non-periodic microstructure and defects on the yield strength of two-dimensional cellular solids. Int. J. Mech. Sci. 39, 549–63.

Smith A. B. (1980), The structure and arrangement of echinoid tubercles, Philosophical Transactions of the Royal Society of London. B. Biological Sciences 289 (1033).1-54

Smith A. B. (1980), Stereom microstructure of the echinoid test. Pap. Palaeontology. 25,1-81

Smith A. B. (1984), Echinoid Palaeobiology. Special Topics in Palaeontology. London, UK: Allen & Unwin.

Smith A., N. Hollingworth, (1990), Tooth structure and phylogeny of the Upper Permian echinoid Miocidaris keyserlingi, Proceedings of the Yorkshire Ge-ological Society 48 (1) 47–60.

Stock S. R., (2014), Sea urchins have teeth? a review of their microstructure, biomineralization, development and mechanical properties, Connective tissue research 55 (1) 41–51.

Su X, Kamat S, Heuer AH. (2000), The structure of sea urchin spines, large biogenic single crystals of calcite. J Mater Sci 35, 5545–555.

Takahashi K. (1967), The catch apparatus of the sea-urchin spine: I gross histology, J. Fac. Sci. Univ. Tokyo (IV) 11, 109–120.

Takahashi K. (1967), The ball and socket joint of the sea urchin spine: geometry and its functional implications. J Fac Sci Tokyo Univ. 11, 131–135.

Telford M., (1985), Domes, arches and urchins: the skeletal architecture of echinoids (Echinodermata). Zoomorphology 105, 114-124.

Telford M., B. Keegan, B. O'Conner, (1985), Structural analysis of the test of Echinocyamus pusillus (OF M¨uller), AA Balkema Rotterdam.

Thompson JR, Cotton LJ, Candela Y, Kutscher M, Reich M, Bottjer DJ. (2022), The Ordovician diversification of sea urchins: systematics of the Bothriocidaroida (Echinodermata: Echinoidea). J. Syst. Palaeontol. 19, 1395-1448.

Toader N., W. Sobek, K. G. Nickel, (2017), Energy absorption in functionally graded concrete bioinspired by sea urchin spines, Journal of Bionic Engineering 14 (2) 369–378.

Vanucci P. (2018), Anisotropic Elasticity. Singapore: Springer.

Van Egmond D. A., B. Yu, S. Choukir, S. Fu, C. V. Singh, G. Hibbard, B. D. Hatton, et al., (2021), The benefits of structural disorder in natural cellular solids, arXiv preprint arXiv:2110.04607.

Vincent JF, Bogatyreva OA, Bogatyrev NR, Bowyer A, Pahl AK. (2006), Biomimetics: its practice and theory. J.R. Soc. Interface, 3, 471-482.

Vincent JF, Bogatyreva OA, Bogatyrev NR, Bowyer A, Pahl AK. (2006), Biomimetics: its practice and theory. J. R. Soc. Interface, 3(9), 471-482.

Vincent JF. (2016), Biomimetics in architectural design. Intelligent Buildings International 8, 138-149.

Vogel S. (2013), Comparative biomechanics: life's physical world. Princeton, NJ: University Press.

Wang R., L. Addadi, S. Weiner, (1997), Design strategies of sea urchin teeth: structure, composition and micromechanical relations to function, Philosophical Transactions of the Royal Society of London. Series B: Biological Sciences 352 (1352) 469–480.

Wainwright SA, Biggs WD, Currey JD, Gosline JM. (1976), Mechanical design in organism. London, UK: Edward Arnold Publisher.

Weber J. N., (1969), The incorporation of magnesium into the skeletal calcites of echinoderms, American Journal of Science 267 (5) 537–566.

Weber J., R. Greer, B. Voight, E. White, R. Roy, (1969), Unusual strength properties of echinoderm calcite related to structure, Journal of ultrastructure research 26 (5-6) 355–366.

Weiner S. (1985), Organic matrix-like macromolecules associated with the mineral phase of sea urchin skeletal plates and teeth. J. Exp. Zool. 234, 7–15.

Wester T. (1984), Structural order in space: the plate-lattice dualism. Copenaghen, Denmark: Royal Academy of Arts, School of Architecture.

Wester T. (1990), A geodesic dome-type based on pure plate action. Int. J. Space Struct. 5, 155–167. (doi:10.1177/026635119000500302)

Wester T. (2002), Nature teaching structures. Int. J. Space Struct. 17, 135–147.

Wilkie IC, Fassini D, Cullorà E, Barbaglio A, Tricarico S, Sugni M, Carnevali MDC. (2015), Mechanical properties of the compass depressors of the sea-urchin Paracentrotus lividus (Echinodermata, Echinoidea) and the effects of enzymes, neurotransmitters and synthetic tensilin-like protein. PloS one, 10.

Wormser C. (2008), Generalized Voronoi Diagrams and Applications (Doctoral dissertation).

Yang T., Z. Wu, H. Chen, Y. Zhu, L. Li, (2020), Quantitative 3d structural analysis of the cellular microstructure of sea urchin spines (i): Methodology, Acta Biomaterialia 107 204–217.

Yang T., Z. Jia, Z. Wu, H. Chen, Z. Deng, L. Chen, Y. Zhu, L. Li, (2022), High strength and damage-tolerance in echinoderm stereom as a natural bi-continuous ceramic cellular solid, Nature Communications 13 (1) 6083.

Yaraghi N. A., D. Kisailus, (2018), Biomimetic structural materials: inspiration from design and assembly, Annual Review of Physical Chemistry 69, 23–57.

Zhang Q, Yang X, Li P, Huang G, Feng S, Shen C, ... & Lu TJ. (2015), Bioinspired engineering of honeycomb structure–Using nature to inspire human innovation. Progress in Materials Science, 74, 332-400.

Zhang W, Wu C, Zhang C, Chen Z. (2012), Microstructure and mechanical property of turtle shell, Theor. Appl. Mech. Lett. 2 (1) 44–48.

Ziegler A, Stock SR, Menze BH, Smith AB. (2012), Macro-and microstructural diversity of sea urchin teeth revealed by large-scale micro-computed tomography survey. In Developments in X-ray tomography VIII (Vol. 8506, p. 85061G). International Society for Optics and Photonics.

Author’s publications

1. Perricone, V., Cesarano, P., Deb M., Lublin, D., Mutalipassi, M., Pappalardo, L., Marmo F., (2024), F. Microarchitectural Design Variation of the Echinoid Skeleton: A 3D Structural and Mechanical Study of Paracentrotud lividus. Journal of the Royal Society Interface (under revision)
2. Perricone V., Cesarano P., Mancosu A., Asnigar D., Bravi S., Marmo F., (2023), Echinoid Skeleton: an insight on the species-specific pattern of the Paracentrotus lividus plate and its microstructural variability. Journal of the Royal Society Interface, 20: 20220673.
3. Yu T., Marmo F., Cesarano P., Adriaenssens S., (2023), Continuous modeling of creased annuli with tunable bistable and looping behaviors. Proceedings of the National Academy of Sciences (PNAS), 120 (4): e2209048120.
4. Paradiso M., Cesarano P., Vaiana N., Rosati L.., (2022), Closed-form expressions of shear deformability tensors associated with a new beam model. IFAC-PapersOnLine 55.20: 427-432.
5. Pellecchia D., Cesarano P., 149-172 (2022), A Generalized Formulation of Time Integration Methods for Nonlinear Dynamic Analysis of Hysteretic Mechanical Systems. Mathematical Applications in Continuum and Structural Mechanics, 149-172. DOI: 10.1007/978-3-030-42707-8_8